Isoscalar Dipole Excitation in Tin Isotopes

Isoskalare Dipolanregungen in Zinn-Isotopen
Zur Erlangung des Grades eines Doktors der Naturwissenschaften (Dr. rer. nat.)
genehmigte Dissertation von Joachim Mario Tscheuschner aus Darmstadt
Tag der Einreichung: 16.01.2018, Tag der Prüfung: 12.02.2018
Darmstadt — D 17

1. Gutachten: Prof. Dr. Thomas Aumann
2. Gutachten: Prof. Dr. Thorsten Kröll

TECHNISCHE UNIVERSITÄT DARMSTADT

Institut für Kernphysik
Fachbereich Physik

Isoscalar Dipole Excitation in Tin Isotopes
Isoskalare Dipolanregungen in Zinn-Isotopen

Genehmigte Dissertation von Joachim Mario Tscheuschner aus Darmstadt

1. Gutachten: Prof. Dr. Thomas Aumann
2. Gutachten: Prof. Dr. Thorsten Kröll

Tag der Einreichung: 16.01.2018
Tag der Prüfung: 12.02.2018

Darmstadt — D 17

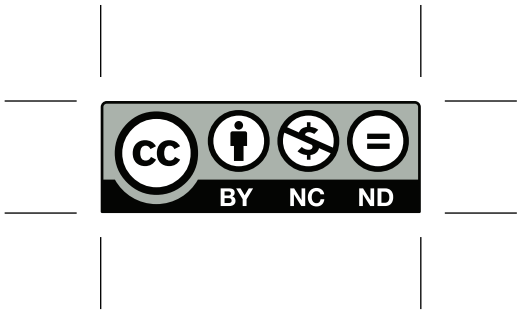

Erklärung zur Dissertation

Hiermit versichere ich, die vorliegende Dissertation ohne Hilfe Dritter nur mit den angegebenen Quellen und Hilfsmitteln angefertigt zu haben. Alle Stellen, die aus Quellen entnommen wurden, sind als solche kenntlich gemacht. Diese Arbeit hat in gleicher oder ähnlicher Form noch keiner Prüfungsbehörde vorgelegen.

Darmstadt, den 15.01.2018

(Joachim Mario Tscheuschner)

Abstract

The investigation of the nuclear structure in stable and unstable nuclei revealed a concentration of dipole strength well below the Giant Dipole Resonance. In the low-lying dipole excitation a separation of the isoscalar and isovector part occurred. One of the questions to answer is the evolution of the excitation mode with increasing neutron-excess. The mode is probed with the tin isotopes Sn-128 and Sn-132 with inelastic isoscalar excitation in inverse kinematics. The experiment was performed at RIKEN RIBF in Japan, Wako. With the aid of the fragment separator BigRIPS and the spectrometer ZeroDegree Spectrometer were the reaction channel Sn(α,α'γ) selected. The target chamber CRYPTA embodied liquid helium as the isoscalar target. It was surrounded by two scintillating crystal arrays. They consists out of NaJ crystals (DALI2) and large volume $LaBr_3$:Ce crystals (HECTOR) placed in forward direction. The detected γ-rays contain the information of the excitation energy.
For both isotopes known transition energies, mainly decays of 2^+ states to the ground state 0^+, were measured and their peak-centroid and cross section determined. The measured transition energies match the literature values. In addition, for both isotopes two new transition energies and their cross section were determined. The transition energies in Sn-128 are 5.45(15) MeV and 6.35(15) MeV with the cross sections 112(29) μb and 79(29) μb, respectively, and in Sn-132 they are 6.25(10) MeV and 7.10(10) MeV with the cross sections 4.03(30) mb and 0.258(16) mb, respectively. The nature of the transitions is not clarified and theoretical calculations are performed. It is remarkable that no transition strength was observed above the neutron separation-threshold.
Under the assumption that the transitions are *E1*-type, the extracted results are compared to theoretical calculations performed for isoscalar low-lying dipole excitation using Quasiparticle Random Phase Approximation. Within the uncertainties they agree with each other. Furthermore, the results are compared to other experiments performed with stable isotopes and isoscalar probes. A clear trend of the excitation energy with the asymmetry $\left(\frac{N-Z}{A}\right)^2$ was not observed. In addition the result for Sn-132 is compared to the isovector mode in the same isotope. The excitation energy is about 9.8(7) MeV. If the low-lying dipole mode was observed in the experiments, then the low-lying dipole modes separates in energy the isoscalar and isovector part.

Zusammanfassung

Die Untersuchung der Kernstruktur hat in stabilen und radioaktiven Kernen niedrig liegende *E1* Übergange offen gelegt. Dabei wurde auch eine Separation der isoskalaren und isovektoriellen Mode entdeckt. Eine der offenen Fragen ist, wie sich diese Mode mit Veränderung des Neutronenüberschusses entwickelt. Zur Untersuchung dieser Mode, wurden die Zinnisotope Sn-128 und Sn-132 durch inelastische isoskalare Anregungen in inverser Kinematik untersucht. Das dazu durchgeführte Experiment fand am RIKEN RIBF in Japan, Wako statt. Unter Verwendung des Fragmentseparators BigRIPS und des Spektroskops ZeroDegree Spectrometer wurden die Reaktionskanäle Sn(α,α'γ) ausgewählt. Als Target wurde CRYPTA mit flüssigem Helium verwendet. Das Target war von zwei szintillierenden Detektorgruppen umschlossen. Diese bestanden aus NaJ Kristallen (DALI2) und großvolumigen $LaBr_3$:Ce Kristallen (HECTOR) in Vorwärtsrichtung. Die nachgewiesenen γ-Quanten geben Aufschluss über die Anregungsenergie der Zustände in den beiden Zinnisotopen.
Für beide Isotope wurden bereits bekannte Übergänge, hauptsächlich 2^+ zum Grundzustand 0^+, gemessen und deren Schwerpunktsenergien und Wirkungsquerschnitte bestimmt, wobei deren Übergangsenergien mit den Literaturwerten übereinstimmen. Des Weiteren wurden für beide Isotope jeweils zwei neue Übergangsenergien und deren Wirkungsquerschnitte bestimmt. Für Sn-128 wurden die Energien zu 5.45(15) und 6.35(15) MeV mit den Wirkungsquerschnitten $112(29)\,\mu$b und $79(29)\,\mu$b ermittelt. Und für Sn-132 zu 6.25(10) MeV und 7.10(15) MeV mit den Wirkungsquerschnitten 4.03(30) mb und 0.258(16) mb bestimmt. Welche Art die neuen Übergänge sind, ist bisher noch nicht geklärt, aber theoretische Untersuchungen dazu sind auf dem Weg. Bemerkenswert ist, dass oberhalb der Neutronenseparationsschwelle keine Übergangsstärke beobachtet wurde.
Unter der Annahme eines *E1*-Übergangs, wurden die Ergebnisse mit theoretischen Berechnungen für isoskalare Dipolanregungen, basierend auf Quasiparticle Random Phase Approximation, verglichen. Innerhalb der Unsicherheiten stimmen die Ergebnisse überein. Außerdem sind die Ergebnisse mit anderen durchgeführten Experimenten mit stabilen Isotopen verglichen worden. In diesen Experimenten wurden auch isoskalare Sonden verwendet. Ein klarer Trend der Anregungsenergie als Funktion der Asymmetrie $\left(\frac{N-Z}{A}\right)^2$ ist nicht zu erkennen. Das Ergebnis für Sn-132 wurde zudem mit einem Experiment verglichen, in dem die isovektorielle Mode angesprochen wird und deren Anregungsenergie bei 9.8(7) MeV liegt. Falls es sich um eine niedrig liegende Dipolanregung handelt ergibt sich auch für das instabile Sn-132 eine Separation zwischen den isoskalaren und isovektoriellen Anregungen in der Anregungsenergie.

Contents

1. Introduction 2

2. Low-Lying Dipole Transition 4
   2.1. Experimental Knowledge . . . 4
   2.2. Theoretical Framework . . . 6
   2.3. Quasiparticle Random Phase Approximation . . . 7

3. Experimental Setup and Simulation 12
   3.1. Isotope In-Flight Separation Technique . . . 12
      3.1.1. Production . . . 13
      3.1.2. Separation and Identification . . . 13
   3.2. Experimental Setup . . . 15
      3.2.1. Production of the Primary Beam . . . 15
      3.2.2. BigRIPS and ZeroDegree Spectrometer . . . 15
      3.2.3. In-Beam Detector . . . 19
   3.3. In-beam γ-spectroscopy . . . 23
   3.4. γ detector . . . 24
      3.4.1. DALI2 . . . 24
      3.4.2. LaBr Detectors . . . 27
   3.5. Target . . . 29
   3.6. Data Acquisition System . . . 31
   3.7. Experimental Runs . . . 31
   3.8. Simulation . . . 33

4. Data Analysis 35
   4.1. BigRIPS and ZeroDegree Spectrometer . . . 35
      4.1.1. Position Measurement . . . 35
      4.1.2. Time-of-Flight . . . 36
      4.1.3. Energy Loss . . . 39
      4.1.4. Total-Kinetic Energy . . . 40
   4.2. Event Selection . . . 40
   4.3. Target Thickness . . . 43
   4.4. γ-Detection . . . 48
      4.4.1. Energy Calibration . . . 48
      4.4.2. Time Calibration . . . 51
      4.4.3. Addback Routine . . . 54

4.4.4. Doppler Correction . . . 56
4.4.5. Efficiency . . . 58
4.5. Simulation . . . 59
4.6. Estimating the Background . . . 60

5. Conclusion 65
5.1. Determination of the Cross Sections . . . 65
5.1.1. Sn-132 . . . 66
5.1.2. Sn-128 . . . 68
5.2. Estimation of the Systematic Error . . . 77
5.3. Comparison to Theory and Experiments . . . 78

6. Summary and Outlook 80

Appendices 83

A. Beam profile 84

B. Fiber detector 89
B.1. Motivation . . . 89
B.2. Design . . . 89
B.3. Construction . . . 92
B.4. Test . . . 93
B.5. Summary and Outlook . . . 97

C. Components of the Fiber Detector 99
C.1. Photodetector . . . 99
C.1.1. Photomultiplier Tube . . . 99
C.1.2. Silicon Photomultiplier . . . 101
C.2. Electronic . . . 101
C.2.1. FEBEX . . . 101
C.2.2. PADI and VFTX . . . 102
C.2.3. PADI and VFTX . . . 102

D. Acronyms 108

E. Acknowledgement 110

1 Introduction

The atomic nucleus is formed by neutrons and protons, while the number of the latter determines the chemical element. As the protons repel each other due to the Coulomb force, one could naively think that elements other than hydrogen should not be formed. The nuclear force counteracts the repulsion. The nuclear force leads to bound systems with increasing binding energy per nucleon up to Nickel (Ni-62). The binding energy can be measured as the mass deficit of the bound system compared to the sum of the masses of all its individual parts. The mass of a nucleus can be described in terms of the liquid-drop-model by the Bethe-Weizsäcker formula [Wei35].
For a more precise description of collective and single particle excitation in nuclei, more advanced models and potentials have been developed. Potentials have been designed from first principles, for example the (pionless) effective field theory [SH00], or phenomenological interactions such as the Gogny-force [BGG91]. For the models the shell model is an example, in which the excitation energies and states are calculated.
Also on the experimental side modes of excitation have been discovered and are studied, *e.g.*, collective modes. One of these is the Giant Dipole Resonance (GDR). This excitation mode splits into an isovector and isoscalar part and is located well above the particle separation energy. These modes can be pictured as a vibration of the protons and neutrons out-of-phase and in-phase, respectively, see for example [AN13, PVKC07a]. On the low-energy tail located between excitation energy of 5 and 11 MeV, another excitation mode was discovered, see for example [SAZ13], the low-energy dipole excitation, also referred to as soft-dipole mode or as pygmy dipole resonance. This mode appears for nuclei with an asymmetric proton-to-neutron ratio and its nature is still under debate. Nevertheless, to understand this mode, its isoscalar and isovector nature is explored. Many efforts are undertaken to investigate this mode with different probes as a function of the asymmetric proton-to-neutron ratio, see chapter 2. As such, the tin isotopes have been selected as they provide 10 stable isotopes and have a closed proton shell[1] ($Z = 50$).
The experiments were or will be performed at different accelerator facilities, for example GSI Helmholtzzentrum für Schwerionenforschung GmbH (Darmstadt, Germany) [GSIc], S-DALINAC [Ric96] at the Institut für Kernphysik of the TU Darmstadt (Darmstadt, Germany), and at the RIKEN Nishina research facility (Wako, Japan) [Kub03].
In this thesis, the isoscalar nature of the low-lying dipole excitation is investigated for the isotopes Sn-128 and Sn-132. Therefore, an experiment using inelastic α-scattering

[1] The closed shell/magic numbers are the same for the proton and neutron shell: 2, 8, 20, 28, 50, 82, and 126. They refer to a sudden change in excitation energy to the first excited state and in the transition probability.

was performed at RIKEN. The experiment was performed in inverse kinematics due to the short lifetime of the isotope of interest, where a beam of the nuclei impinges on a liquid-helium target. The target is surrounded by γ-detectors to provide high geometrical efficiency. In order to select the reaction channels of interest, Sn-128$(\alpha, \alpha'\gamma)$ and Sn-132$(\alpha, \alpha'\gamma)$, the incoming and outgoing particles are identified using BigRIPS and ZeroDegree Spectrometer [KOT+09], respectively.

An overview of the underlying physics is given in chapter 2. In chapter 3 the experimental details are described. The calibration of the detector, event-selection, and simulation are presented in chapter 4. Chapter 5 shows the results, in particular the fit procedure using simulations of the detector response and the results. Finally, chapter 6 discusses the problems and gives and outlook for future experiments.

2 Low-Lying Dipole Transition

Properties of nuclei are described within various theoretical frameworks. They are connected via observables to experimental data. The measurement of the low-lying dipole excitation can provide a cross section and energy distribution to compare to theoretical models. Using different experimental probes, such as electromagnetic and isoscalar hadronic probes, further information on the modus of the excitation, namely isovector and isoscalar can be revealed.
The first part summarizes key experimental knowledge to date. The second section introduces the theoretical nuclear structure model used to predict position and strength of the excitation.

2.1 Experimental Knowledge

The experimental knowledge about the isoscalar mode of the low lying dipole excitation in unstable isotopes is scarce. In order to investigate the isoscalar and isovector modes, it is necessary to probe the isotope of interest with different particles sensitive to either mode. The photon for example couples to the proton and excites the isovector mode, in contrast to the α-particle, the hadronic part, is sensitive mainly to the isoscalar mode. For the stable Sn-124 isotope (α,$\alpha'\gamma$) [ELS+10] and (γ, γ') [VTB+06] experiments have been performed at the AGOR cyclotron at KVI, Groningen and S-DALINAC, Darmstadt. Figure 2.1 shows and compares the results of the two experiments. The upper panel shows the observed transitions with inelastic α-scattering in red, while the lower panel shows the transition observed in the γ-scattering experiment. In the α-scattering less states are excited as the probe dominantly excites isoscalar transitions, while the photon probes both, isoscalar and isovector transitions. Thus, by comparing the two experiments isoscalar and isovector excitations can be separated. Typically the isoscalar part lies lower in energy (for this excitation mode).
The isotope Sn-132 has also been investigated by Coulomb-excitation [KPA+07]. In this experiment, performed in inverse kinematics, a lead target was used. The kinematically complete measurement made it possible to observe the excitation far above separation threshold by reconstructing the invariant mass. The centroid of a low-lying dipole mode and the giant dipole resonance at energies of 9.8(7) MeV and 16.1(7) MeV was determined, respectively. The low-lying dipole mode was shown to exhaust a few percent of the energy-weighted sum rule. A systematic increase of the isovector dipole strength with increasing neutron to proton ratio is observed, see figure 2.2. An experiment with a similar setup to study Sn-128 was performed and is currently being analyzed, [Hor]. With the available data the behavior of the dipole strength and the position of the energy centroid is investigated along one isotopic chain in a systematic

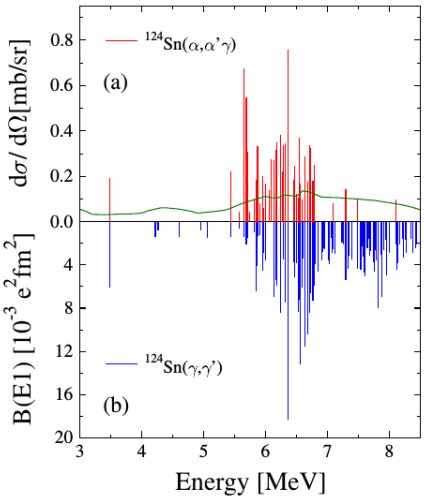

Figure 2.1.: The upper panel shows the differential single cross-section is shown for 1^--states in Sn-124, obtained in Sn-124$(\alpha, \alpha'\gamma)$ scattering. The green solid line marks the experimental sensitivity limit. The lower panel shows the transitions observed in (γ, γ') scattering. In the α-scattering less states are excited as the probe dominantly excites isoscalar transitions, while the γ probes the isovector part. Reprinted figure with permission from [ELS+10]. Copyright (2018) by the American Physical Society.

recording.
The α-probe, used to examine the isoscalar part, mainly excites *E1* transitions, but also *E0* and *E2*. Since the nuclei Sn-128 and Sn-132 have a 0^+ ground state the de-excitation should cascade to the ground-state or to one of the 2^+-states as *E1*-transitions are favored by the electromagnetic decay-mode, see figures 5.2 and 5.7. A review of the experimental concepts and results can be found in [SAZ13] and [AN13].

Energy Weighted Sum Rule

The sum of all excitation probabilities from the ground-state to all possible excited states is given in terms of a sum rule. The electromagnetic response can be characterized using the Energy Weighted Sum Rules (EWSR). Here, the Thomas-Reiche-Kuhn sum rule [Tho25, RT25, Kuh25] is given for *E1* transitions and has the following from

$$\sum E1 = \int_0^\infty \sigma_\gamma(E) dE \approx 60 \frac{NZ}{A} \text{MeV mb}. \tag{2.1}$$

Here, σ_γ is the photon absorption cross-section, N is the neutron number, Z is the proton number, and $A = N + Z$ the mass number [HD81]. Experiments were performed

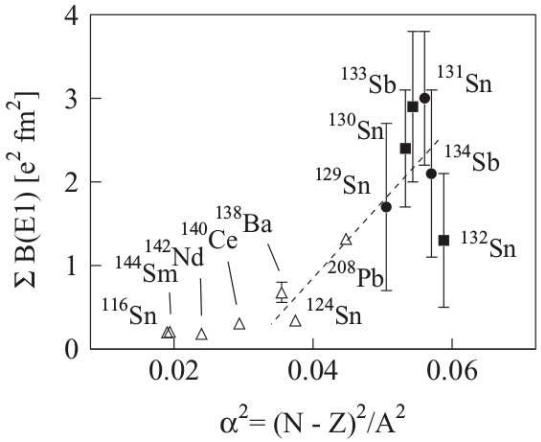

Figure 2.2.: Change of the strength with increasing asymmetry for isovector dipole excitation is shown. The open symbols present stable isotopes, while the solid symbols present unstable isotopes. Reprinted figure with permission from [KPA+07]. Copyright (2018) by the American Physical Society.

to study the GDR and the low-lying dipole excitation. Typically the low-lying dipole excitation exhausts a few percent of the TRK sum-rule, while for example the Giant Dipole Resonance exhausts about 100% [SAZ13].
The IsoScalar-ESWR (IS-ESWR) can be calculated using the variant taken from [HD81]. Here, only the limit for $q \to 0$ is given by

$$\sum_n (E_n - E_0)P = \frac{\hbar^2 A}{32m\pi}\left(11\langle r^4\rangle - \frac{25}{3}\langle r^2\rangle^2\right), \tag{2.2}$$

with $P = \frac{1}{2}\sum_i r_i^3 Y_1^0(r)$ and $Y_1^0(r)$ being the spherical harmonic function. The last term is left out, as it is a small contribution for nuclei with $A \geq 20$.

2.2 Theoretical Framework

The theoretical model applied in this thesis is based on the non-relativistic Quasiparticle Random-Phase Approximation (QRPA) using the Gogny-force (D1S) or Argonne V18. This is also presented in [PHPR14] and references therein. Using two and three nucleon interaction terms. An *ab initio* calculation is at the time not feasible [Rot], due to computational limitations.
In order to describe a nucleus, namely its energy levels, the potential or force between the nucleons is needed for solving the many-body problem. As the potential is not an observable different parametrizations for the potential exist.

Gogny D1S

The Gogny D1S force [BGG91] is developed for the Hatree-Fock-Bogolyubov (HFB) base. It can reproduce the mean-field but also includes pairing of the nucleons. The parametrization of the 2 particle residual part can divided into four parts: The first term corresponds to a finite range potential with the exchange in spin, isospin, and space. The second term depends on the density, the third one is the coupling between spin and orbital momentum. The last term models the Coulomb-force between the protons.

Argonne V18

The Argonne V18 potential uses 18 terms with 40 parameters to model the two nucleon potential, nn, np, and pp [WSS95]. The potential is composed of electromagnetic, one-pion-exchange, and an phenomenological, short- and intermediate-range, interactions. The parameters of the interactions are fitted to nucleon scattering data and the deuteron binding-energy. To improve the potential a phenomenological two-body density dependent term is added. The term models the three-body contact interaction, which is needed to reproduce the ground-state energies and the charge radii in medium to heavy nuclei.
In order to increase the convergence of many-body models the interaction can be diagonalized before by unitary transformation. The Argonne V18 interaction is transformed using Unitary Correlation Operator Method (UCOM) and Similarity Correlation Operator (SRG). By transforming the interaction matrix with a unitary transformation.

2.3 QRPA

The QRPA based on the RPA is a microscopic model using 1-Particle-1-Hole (1p1h), and higher orders, called second RPA or beyond RPA, such as 2p2h, excitations to describe the structure of the ground state and collective excitation. The approximations in the theory is the choice of the space, for example the HFB instead of the full Hilbert space. And the operator is restricted to create particles and holes or in the QRPA quasiparticles. Particle and quasiparticle basis are connected with each other by a linear transformation [RS80].
In the following, the basic concept of the RPA is explained, restricting to 1p1h, for more details refer to [RS80] or [PVKC07b]. Following the second quantization framework, the Schrödinger equation, with the Hamilton operator H, can be written as

$$\langle 0|[a_i^\dagger a_m,[H,Q_\nu^\dagger]]|0\rangle = E_\nu \langle 0|[a_i^\dagger a_m,Q_\nu^\dagger]|0\rangle. \tag{2.3}$$

In the equation $|0\rangle$ is the vacuum state, a_i represents a hole or the annihilation-operator of state i, the $a_m^\dagger$ is the particle state or the creation-operator for state m and E_ν is

the excitation energy of the state. The collective ph-operator $Q^\dagger_\nu$ including the 1p-1h correlations

$$Q^\dagger_\nu = \sum_{m,i} C^\nu_{mi} a^\dagger_m a_i \tag{2.4}$$

is used to create a particular state $|\nu\rangle = Q^\dagger_\nu |\nu\rangle$. This represents the Tamm-Dancoff approximation. Going to RPA the equation is as following

$$Q^\dagger_\nu = \sum_{m,i} X^\nu_{mi} a^\dagger_m a_i - \sum_{m,i} Y^\nu_{mi} a^\dagger_i a_m, \tag{2.5}$$

with the amplitudes X^ν_{mi} and Y^ν_{mi}. They encode in the absolute squares the probability to find the states $a^\dagger_i a_m|0\rangle$ in the (excited) state $|\nu\rangle$. This leads to a set of two equations, as not only ph-pair can be created but also annihilated

$$\begin{aligned} \langle 0|[a^\dagger_i a_m, [H, Q^\dagger_\nu]]|0\rangle &= E_\nu \langle 0|[a^\dagger_i a_m, Q^\dagger_\nu]|0\rangle, \\ \langle 0|[a^\dagger_m a_i, [H, Q^\dagger_\nu]]|0\rangle &= E_\nu \langle 0|[a^\dagger_m a_i, Q^\dagger_\nu]|0\rangle. \end{aligned} \tag{2.6}$$

In the calculations presented here the QRPA is extended to phonons, [PHPR14] and references therein. They include coupling between single and more phonon-states. The ground-state is then the phonon vacuum, while all the excited states are expressed via phonon states. The phonons are built from two quasi-particles in the canonical basis. Using spherical symmetry the phonon-creation operator $O^\dagger_{kJM}$ can be expressed angular-momentum coupled as

$$O^\dagger_{kJM} = \sum_{(\mu m)<(\mu' m')} X^k_{\mu,\mu'} A^\dagger_{\mu\mu' JM} - Y^k_{\mu,\mu'} \tilde{A}_{\mu\mu' JM}, \tag{2.7}$$

with the quantum numbers J and M for the total angular momentum and its projection, respectively. The indices μ summarizes the indices $|nlj\tau\rangle$, which stand for radial, angular momentum, and isospin quantum number. The quasi-particle creation operator $A^\dagger_{\mu\mu' JM}$ is

$$A^\dagger_{\mu\mu' JM} = \frac{1}{\sqrt{1+\delta_{\mu\mu'}}} \sum_{m,m'} \alpha^\dagger_{\mu m} \alpha^\dagger_{\mu' m'}. \tag{2.8}$$

$\alpha^\dagger_{\mu m}$ is the Bogoliubov transformation between the particles and quasiparticle basis. This leads to a different set of equations similar to equation 2.6

$$\begin{aligned} \langle 0|[\tilde{A}_{\mu\mu' JM}, [H, \tilde{A}^\dagger_{\nu\nu' JM}]]|0\rangle &= E_\nu \langle 0|[\tilde{A}_{\mu\mu' JM}, \tilde{A}^\dagger_{\nu\nu' JM}]|0\rangle, \\ \langle 0|[\tilde{A}_{\mu\mu' JM}, [H, \tilde{A}_{\nu\nu' JM}]]|0\rangle &= E_\nu \langle 0|[\tilde{A}_{\mu\mu' JM}, \tilde{A}_{\nu\nu' JM}]|0\rangle, \end{aligned} \tag{2.9}$$

with $\tilde{A}_{\mu\mu' JM}$ being the spherical adjoint of $A^{\dagger}_{\mu\mu' JM}$. For the low-lying dipole transitions the eigenstates of the above equations are used to calculate the reduced transition probability, which is given by

$$B(EJ, J_i \to J_f) = \frac{1}{2J_i+1} |\langle J_f \| Q_J \| J_i \rangle|^2, \tag{2.10}$$

inserting the QRPA phonon states, and the final state being the ground state, leads to the reduced matrix element

$$\begin{aligned} \langle J \| Q_J \| 0 \rangle = \sum_{k \le k'} & \frac{1}{\sqrt{1+\delta_{kk'}}} \\ & (u_k v_{k'} + (-1)^J v_k u_{k'})(X^{kJ*}_{kk'} \langle k \| Q_J \| k' \rangle + (-1)^J Y^{kJ*}_{kk'} \langle k \| Q_J \| k' \rangle^*). \end{aligned} \tag{2.11}$$

The asterisk refers to the complex conjugation. v_k and u_k are not normalized antisymmetrized two-body matrix elements. With the isoscalar *E1* transition-operator

$$Q_{IS} = e \sum_{i=1}^{A} \left(r_i^3 - \frac{5}{3} \langle r^2_{rms} \rangle r_i \right) \sqrt{3} Y_{1M}(r_i) \tag{2.12}$$

which is corrected for spurious center-of-mass effects[1] the strength of the transitions can be evaluated. Y_{1M} any number can be chosen as, here "1" is taken, as the value is independent of the direction.

In the calculations for the tin isotopes, performed by Papakonstantinou et al. [PHPR14], spherical symmetry is assumed and the above mentioned potentials are used. The model is tested by comparing it to experimental results of charge and matter radii in tin isotopes. They both have reasonable results although the Gogny D1S potential agrees slightly better.

Still the strength as a function of the excitation energy is different comparing the two different interactions as shown in figure 2.3. There, the strength is separately shown for the isovector and isoscalar contribution including the Giant Dipole Resonance region. For the isoscalar mode the Gogny interaction indicates a smooth decrease of the excitation energy with increasing neutron number. The Argonne V18 interaction predicts a more structured (fragmented) isoscalar strength. The excitation energy of the first excited isoscalar dipole state has a minimum for Sn-120 and rises again up to Sn-132, but the energy and strength for the isotopes Sn-128 and Sn-132 are similar. The prediction for the isotope Sn-124 can be connected to the experimental values, the isoscalar low-lying dipole excitation energy for the state was found to be at 5.5 and 6.5 MeV, compare to figure 2.1. The calculation predicts the states to be at 8.5 to 9 MeV. This corresponds to a shift of about 3 MeV, which is also true for the GDR in

[1] Spurious states are excitation with low energies. They are artefacts of the model introduced for example by the translation of the center of mass.

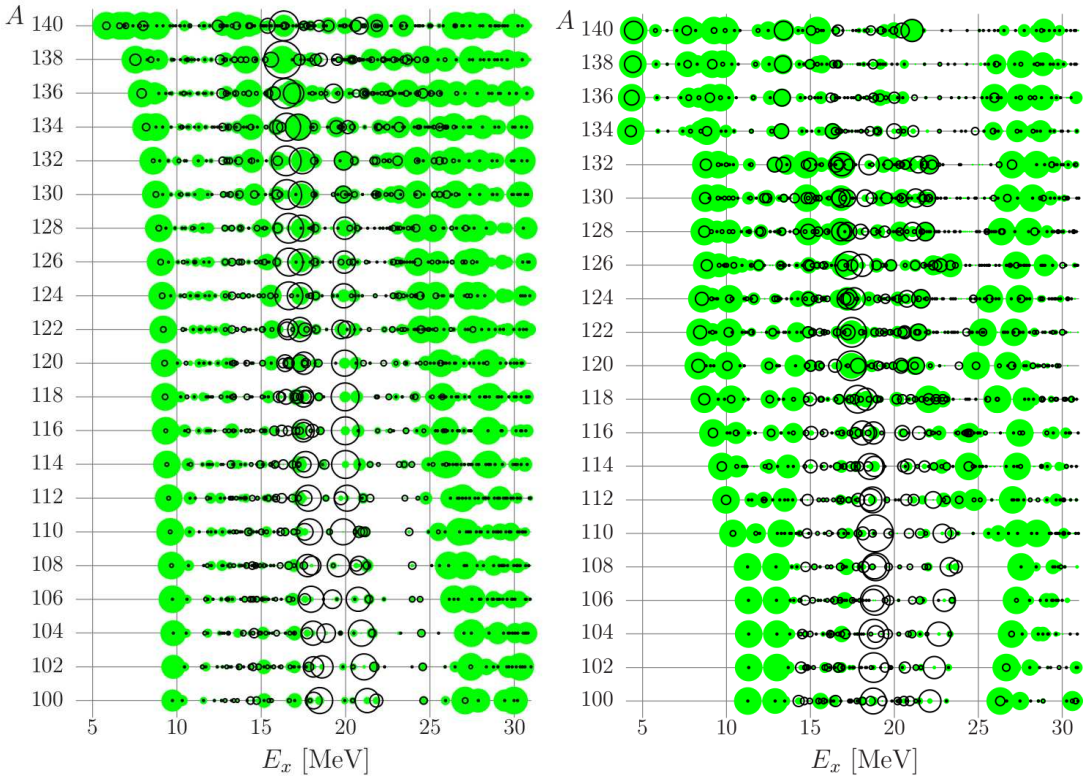

(a) Gogny D1S (b) Argonne V18

Figure 2.3.: The transition strength is shown as function of the excitation energy for different even-even tin isotopes for the two interactions. The strength of isoscalar • and isovector ∘ excitation is proportional to the area of the presenters.The GDR can be identifed in the region between 15 and 20 MeV. Reprinted figure with permission from [PHPR14]. Copyright (2018) by the American Physical Society.

Sn-132. The suggested IS-EWSR strength for all tin isotopes below the the particle threshold should account for 3% to 8%, while above the threshold the strength up to 12 MeV should exceed 5 to 10%.

Figure 2.4 shows the transition densities within the models for the indicated isotope and energy for the isoscalar mode. The main transition strength is located at the surface. The density evolves from Sn-100 to Sn-134 to be more neutron pronounced at the surface. This fact is reassuring as the α-particle interacts with the nucleus at the surface.

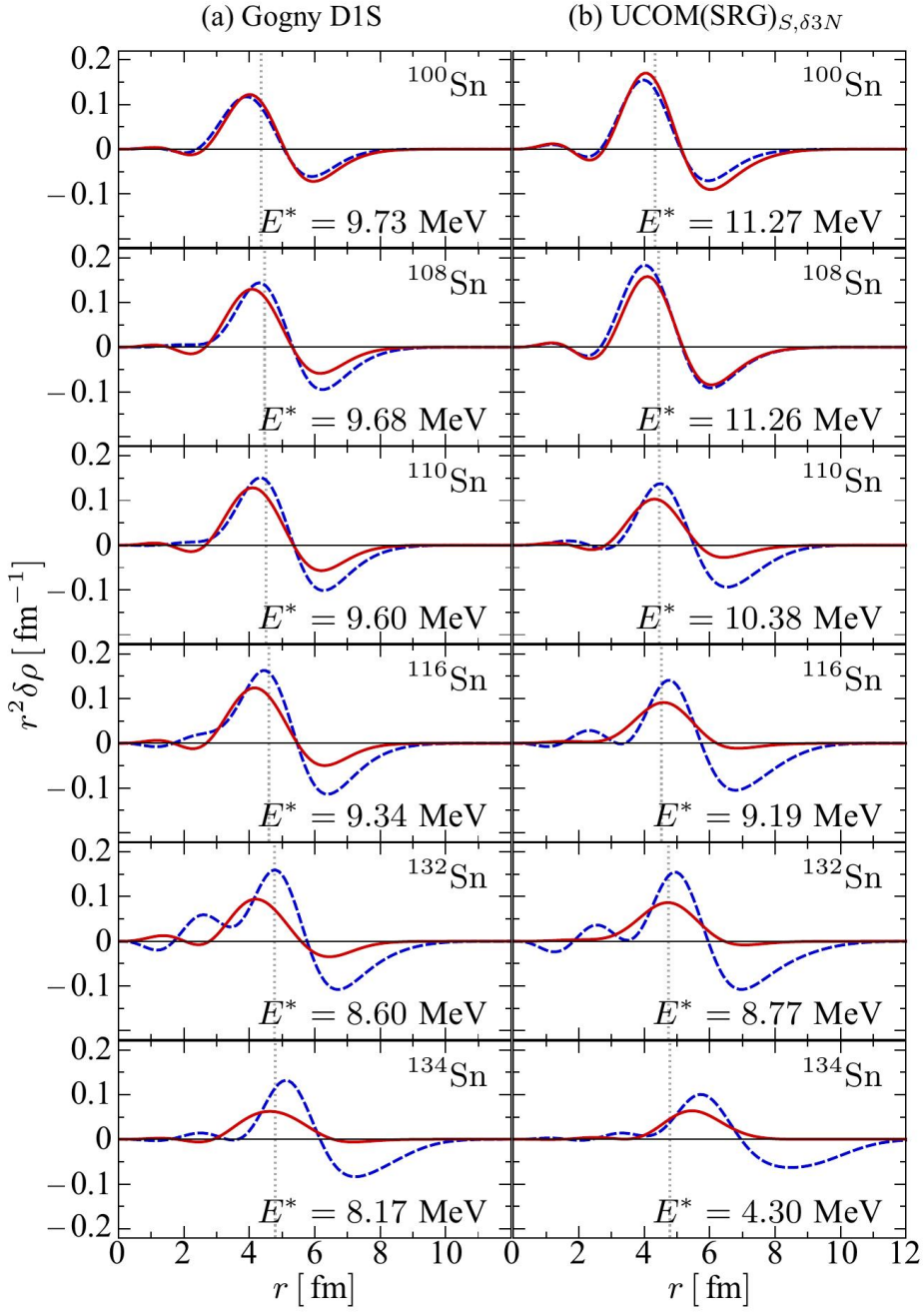

Figure 2.4.: The calculated transition densities in the nuclei for the isoscalar mode as a function of the radius for defined excitation energies. The solid red line represents the protons and the dashed blue line the neutrons. The left row shows the transition densities calculated using the Gogny interaction and the right row shows the same calculated with the Argonne V18 interaction. Reprinted figure with permission from [PHPR14]. Copyright (2018) by the American Physical Society.

3 Experimental Setup and Simulation

3.1 Isotope In-Flight Separation Technique

Radioactive Ion Beams (RIB) offer the opportunity to study nuclei from the valley of stability up to the drip-lines of protons or neutrons. Thus, with RIBs our knowledge about the nuclei, their production mechanism, and abundance in the universe are increased. To produce RIBs mainly two different techniques are available, the Isotope Separation On-Line (ISOL), and the In-Flight method, both showing different advantages.

The ISOL-method uses a primary beam of light ions, like protons or α-particles, to impinge them on a thick primary target [Got16]. The produced fragments diffuse to the surface of the source. The isotopes of interest are selected by chemical or physical interactions in the source [BCE+07] or for example by a two step Laser ionization [FKM12]. Afterwards the ions are accelerated and transported to the experimental areas. This method provides ions with low energies, which can be accelerated afterwards to a few 10 AMeV and due to the diffusion it takes quite some time to extract the isotopes. On the one hand, this limits the method to a minimum lifetime of the ions. Chemical and physical processes in the target restricts the output to limited chemical species. this method is highly selective, ensuring a beam with almost no contamination. Moreover, high-intensity beams can be achieved as thick targets are used, of course depending on the selected isotope. Examples of such accelerator facilities are ISAC at TRIUMF [BHK16], ISOLDE at CERN [Bor16], and the future SPES at LNL [Pre16]. The institutes are located in Canada, Swiss, and Italy, respectively.

The In-Flight method uses a target with thickness of a few grams per square centimeter to fragment or fusion evaporation a heavy beam instead of the target. Due to the thinner target and the high energy of the primary beam, the fragments will have a velocity similar to the primary beam after traveling through the target. The secondary beam is transported and focused to experimental setups. While transporting the beam it is necessary to identify the produced isotopes and separate them. Due to overlapping momenta and spacial distributions of the generated isotopes caused by the production mechanism the secondary beam consists of a cocktail of different isotopes, depending on the choice of the primary beam (isotope and energy) and target. Examples for this kind of facility are A1200 at NSCL/MSU [SMNW91], the BigRIPS at RIKEN [KKS+12], and the FRS at GSI [GAB+92], which is being upgraded to the future FAIR facility at the moment [hMNW99]. Those facilities are located in the USA, Japan, and Germany, respectively.

For the experiment reported in this thesis, the In-Flight method was used and is described in the following.

3.1.1 Production

The In-Flight method uses a high energy primary beam of a few 100 MeV, which is shattered into many different isotopes of smaller mass by a target with a thickness on the order of 1 $\frac{\mathrm{g}}{\mathrm{cm}^2}$ by means of fission or fragmentation[1]. In peripheral interactions with the target nuclei, some nucleons might be removed. Due to the high velocity of the projectile the reaction products lie within a narrow forward cone. As such an electromagnetic separator can accept an higher percentage of fragments if the velocity is higher.
The distribution of velocity, charge, and mass can be described using microscopic or macroscopic models [DM79].
The fission mechanism produces mainly neutron-rich isotopes.

3.1.2 Separation and Identification

The separation of the ions after the reactions in the primary target is based on the different magnetic rigidity $B\rho$ of the fragments. This quantity depends on the velocity in βc, where β is the velocity in units of the speed of light c, and the charge-to-mass ratio $\frac{A}{Q}$. If the magnetic field B is orthogonal to the trajectory of the ion the quantities are connected via the equation

$$B\rho = \frac{P}{Q} = \frac{\gamma m v}{Q} = \gamma\beta\frac{A}{Q}c\mathrm{u}, \tag{3.1}$$

ρ the bending radius, v the velocity, c the speed of light, $\beta = \frac{v}{c}$ the relative velocity to c, $\frac{1}{\gamma} = \sqrt{1-\beta^2}$ the relativistic factor, Q the charge of the ion, and u the atomic mass unit. In the case of fully stripped ions, $\frac{A}{Q}$ can be rewritten as $\frac{A}{Z}\frac{1}{e}$ with Z being the proton number and e the elementary charge. Using one dipole magnet allows to separate and select isotopes of certain $B\rho$. In practice most separators are using two magnets in order to focus the beam after separation. The focusing can be done in the achromatic or chromatic mode. In the achromatic mode the isotopes with the same magnetic rigidity are focused on one point in a focal plane ignoring their different momenta $p = \gamma m\beta$. Whereas in the chromatic mode the ions with the same momenta are focused on one point. All planes between the focal planes are called dispersive. As done in [FKO+13], the transport can be described in first order by the equation

$$x = (x|x)x_0 + (x|a)a_0 + (x|\delta)\delta_0. \tag{3.2}$$

Here, x and a represent the coordinate and angle of the particle in respect to the horizontal plane. δ refers to the deviation in momenta of the particle to the central trajectory. The index "0" refers to the initial value, and the coefficients in brackets "()"

[1] This corresponds to 5.5 mm thick beryllium target

represent the matrix-elements of the ion-optical transportation matrix. In addition to the dipole magnets, quadrupole magnets are focusing the beam and higher order magnets can be used to correct ion-optical aberrations.
In order to differentiate between ions with similar $B\rho$, energy loss methods can be used. For this purpose a material is inserted into the beam line. The energy loss of the beam particle can be described by the Bethe-Bloch formula [Kno00]

$$-\frac{dE}{dx} = \frac{4\pi e^2 Z^2}{m_e v^2} Z_m \rho_n \left(\ln \frac{2m_e v^2}{I} - \ln(1-\beta^2) - \beta^2 \right) \tag{3.3}$$

$\frac{dE}{dx}$ refers to the energy loss per length unit, Z_m and ρ_n are the atomic and density number, and I is the average excitation and ionization constant of the material.
Ions with the same $\frac{A}{Q}$ but with different momenta p are focused using wedge-shaped degrader. As the energy loss depends on the Z^2 of the projectile, ions with the same $\frac{A}{Q}$ but different momenta p are focused using such degrader. As the energy loss depends on the velocity, and the momentum (velocity) distribution is a function of the radius, the inserted amount of material is also a function of the radius. Particles with higher velocity will pass through more material than particles with less velocity. With a second dipole-stage the ions can be further separated. This described method is the so called $B\rho - \Delta E - B\rho$ separation method. This method is used at the in-flight separation facilities mentioned above.
Even after the separation the secondary beam consists of a cocktail of different isotopes. These ions have to be identified on an event-by-event basis. The same equations, as for the separation, 3.1 and 3.3 can be used for the identification of the particles. The proton number Z is determined by using the energy-loss method and measuring the velocity. The energy loss can be measured for example with gas-chamber detectors. The deposited energy in the volume is proportional to the number of created charge-carriers. By applying an electric field the charge can be collected and the energy-loss signal is determined. The velocity can be evaluated using two Time-Of-Flight (TOF) detectors (start and stop) with a distance of Δz to each other. With these two quantities the proton number Z can be calculated according to equation 3.3. The TOF detectors usually consist out of fast plastic detectors read out by two or more Photo Multiplier Tubes (PMT) [Kno00]. The magnetic rigidity $B\rho$ is calculated by reconstructing the trajectory of the ions. Therefore, velocity and the x- and y-location at different focal planes are mandatory. To reconstruct the position in the planes, position-sensitive detectors for example silicon-strip detectors, fiber detectors, or multi-wire drift chambers, can be used. With the extracted positions the magnetic rigidity is determined. Using the first order transport equation 3.2 and replacing δ by $\frac{p-p_0}{p_0}$

$$\begin{aligned} B\rho &= B\rho_0 \cdot (1+\delta) \\ &= B\rho_0 \cdot \left(1 + \frac{(x|x)x_0 + (x|a)a_0}{(x|\delta)} \right) \end{aligned} \tag{3.4}$$

the rigidity is calculated in first order. The equation shows that the position, angle and velocity have to be measured to define the mass-over-charge value. AOQ-value is the abbreviation for this, as Q stands for the charge and A for the mass-number of a nucleus.

3.2 Experimental Setup

The experiments to investigate the *E1*-response of the isotopes Sn-128 and Sn-132 were performed within a campaign at Radioactive Isotope Beam Factory (RIBF) at RIKEN, Japan . The facility is operated by the RIKEN Nishina center and Center of Nuclear Study (CNS). The campaign included the scattering of Ni-70 on a gold target and scattering different oxygen isotopes on gold and helium [NHB17]. All experiments used the same γ-detector setup.
In the campaign the isotopes of interest were produced by impinging a primary beam onto a primary target. BigRIPS separator was used to identify and purify the beam, using the described $B\rho - \Delta E - B\rho$ method, see section 3.1.2. The selected and identified ions were transported to the liquid-helium target, which was surrounded by 103 scintillating γ-detectors. The array consisted of two different types of detectors, namely 95 DALI2 [TMT+14] and eight LaBr:Ce Hector [GPR+13] crystals. After the target the ZeroDegree Spectrometer (ZDS) identified the outgoing beam particles.

3.2.1 Production of the Primary Beam

With the SuperConducting Electron Cyclotron Resonance (SC-ECR) ion-source [NKH+08] and the RIKEN heavy Ion Linear Accelerator 2 (RILAC2) [NSA14] the primary U-238 beam is extracted and in a first stage accelerated to 0.67 AMeV. In the four following ring cyclotrons, the RIKEN Ring Cyclotron (RRC), the Fixed-frequency Ring Cyclotron (fRC), the Intermediate-stage Ring Cyclotron (IRC), and the Superconducting Ring Cyclotron (SRC), the beam is further accelerated. The isotopes reached energies after each step of 11, 50, 127, and 345 AMeV. Between the RRC and fRC, the ions are stripped to the 69+ charge state by a helium gas stripper [OFH+14][IOK+12]. Further stripping follows with a rotating beryllium disk between fRC and IRC to the 86+ charge-states [HOK+15], see figure 3.1. After the last acceleration in the SRC the beam is delivered with an intensity of 1030 enA to the primary target. It consisted of Be-9 and had a thickness of 3 mm located at F0, at the entrance to the BigRIPS.

3.2.2 BigRIPS and ZeroDegree Spectrometer

The primary target for producing the rare isotope beam marks the beginning of the large acceptance separator, BigRIPS. The high acceptance is needed as the produced

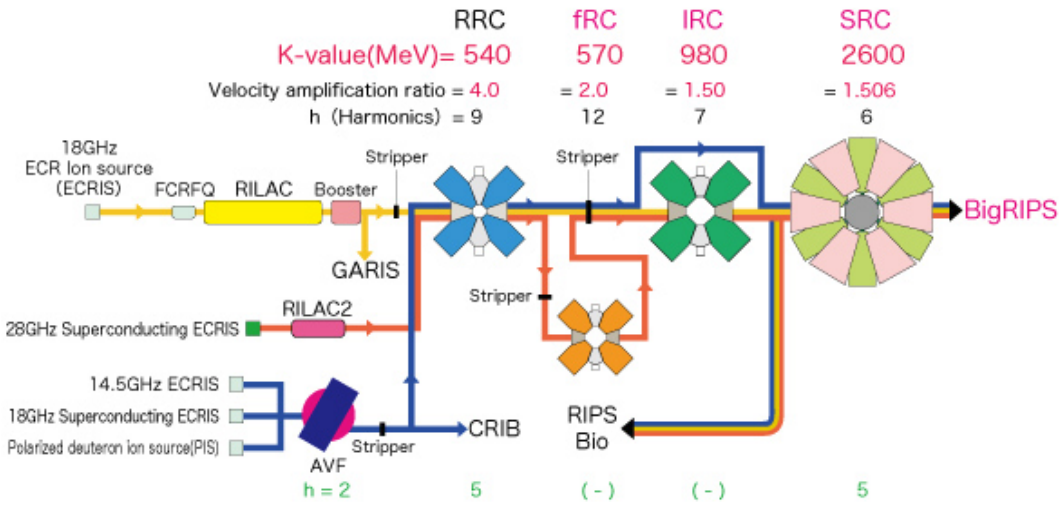

Figure 3.1.: The accelerator stages at RIBF. Using the fixed energy mode and the SC-ECR ion source together with the RILAC2 injector the primary U-238 beam is produced. With all four cyclotrons the ions are accelerated to the maximal available energy of 345 A MeV. The image is taken from [acc].

fragments have a big angular spread. BigRIPS consists of two stages, the first one serves to accept, separate, and focus the beam, see figure 3.2. This stage with two dipole magnets operates in the achromatic mode and has a degrader wedge to separate isotopes with the same magnetic rigidity. The second stage is needed to identify the ions on an event-by-event basis through four dipoles and several position and TOF-measurements, done with Parallel Plate Avalanche Counters (PPAC) and plastic-detectors, respectively. These detectors are distributed over a distance of about 46.5 m. A degrader to enhance the separation was used at the focal plane F5, focal planes are labeled with F#. The TOF is determined between F3 and F7 with a distance of 46.6 m, while the positions are taken at F3, F5, and F7. The energy loss is measured at F7, using a MUltiple Sampling Ionization Chamber (MUSIC) between the PPACs and before the plastic-detector. BigRIPS leads and focuses the beam towards the secondary target located at F8 to study the reaction $\mathrm{Sn}(\alpha, \alpha'\gamma)$. F8 is the beginning of the ZDS, which was used in the large acceptance achromatic mode, see table 3.3 and figure 3.3. It has two dipole and six quadrupole magnets and as a Total-Kinetic Energy-counter (TKE) a NaI(Tl)-scintillator has been used at F11. About 1 m in front of the target the last detector is placed before the target, though this may vary with the setup. To identify the outgoing isotopes, the positions are measured before the target and after the target, while the TOF is determined using plastic detectors before the target at F8 and after the target at F11 with a distance of 36.8 m.

Table 3.1.: Listed here are the locations of the in-beam detectors.

Focal plane	PPAC	TOF
F3	x	x
F5	x	-
F7	x	x
F8	x	x
F10	x	-
F11	x	x

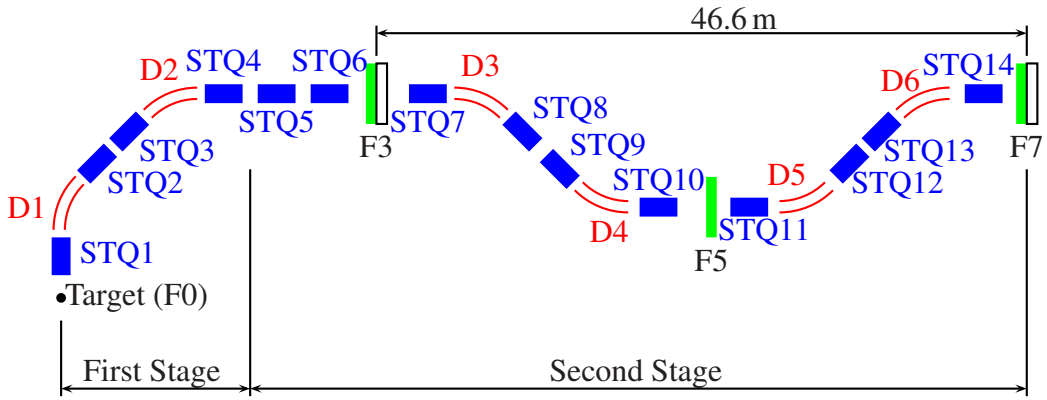

Figure 3.2.: Schematics of BigRIPS. In the first stage from F0 to F2 the fragments of the primary reaction are produced and separated. The second stage from F3 to F7 is used to further separate and identify the isotopes. In solid blue the quadrupole magnets, STQ1 to STQ14, are represented, while the dipole magnets, D1 to D6, are hollow red. The plastic detectors are shown in hollow black, while the position is evaluated at focal planes with green rectangles. Different from other sketches, the beam starts in the lower left corner.

Table 3.2.: Important parameters of the BigRIPS fragment separator. The two values for the momentum resolution are for two different detector setups [KKS+12].

horizontal acceptance	±45 mrad
vertical acceptance	±45 mrad
momentum acceptance	±6%
momentum resolution $\frac{p}{\Delta p}$	1260/3420
max. magnetic rigidity	9.5/8.8 Tm
length	78.2 m

Table 3.3.: Important parameters of the ZeroDegree Spectrometer. In the experiment the large acceptance achromatic mode was used [KOT+09].

mode	large acceptance	medium resolution	medium resolution	high resolution
type	achromatic	achromatic	dispersive	dispersive
horizontal acceptance in mrad	±90	±40	±40	±30
vertical acceptance in mrad	±60	±60	±60	±30
momentum acceptance in %	±6	±6	±4	±2
momentum resolution $\frac{p}{\Delta p}$	1240	2080	4070	6410
max magnetic rigidity in Tm	8.1	9.7	9.8	10.2
length in m	← 36.5 for all →			

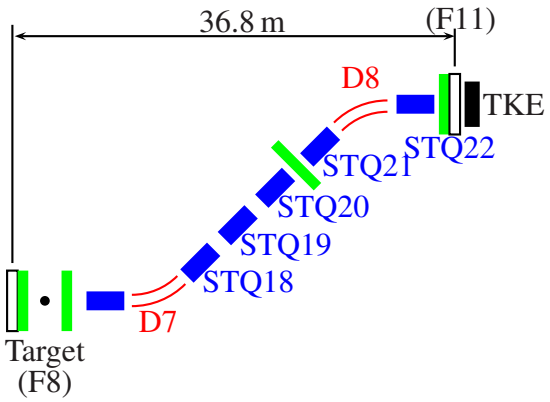

Figure 3.3.: The ZeroDegree Spectrometer identifies with two dipoles, D7 and D8 in hollow red, the outgoing beam from the secondary target. The quadrupole magnets, STQ17 to STQ22 in solid blue, are used to focus the beam. Position measurement are represented in green and the plastic detectors for TOF in hollow black. Different from other pictures the beam starts in the lower left corner.

3.2.3 In-Beam Detector

To identify the in- and outgoing isotopes using energy loss and magnetic rigidity different types of detectors are needed. For the charge determination velocity and energy loss are used, whereas for the magnetic rigidity at least two positions and the velocity are needed. The PPAC detector is position sensitive, whereas the two plastic scintillator detectors are used to obtain TOF and the MUSIC detector measures δE. In combination these detectors ensure a distinct identification of the isotopes.

Parallel Plate Avalanche Counters

The PPACs [KOF+01, KOF+13] are used to measure the position to determine the AOQ-value. A PPAC consists of an anode layer between two cathodes and is filled with C_3F_8 gas, see figure 3.4. The anode has a thickness of 4 μm whereas each cathode has 2.5 μm. They are made up by 2.4 mm wide strips with an inter-strip distance of 0.15 mm. The electrodes are 4.3 mm apart and the total sensitive area is 240 x 150 mm^2. To reduce noise and to have redundancy the PPACs are placed in pairs, called double PPAC. Further, they are electrically isolated from the beam line.
The PPACs are read-out with the delay-line method. Therefore, each of them gives five signals per event: x_1, x_2, y_1, y_2, and the anode-signal. The signals are sent first to a fast

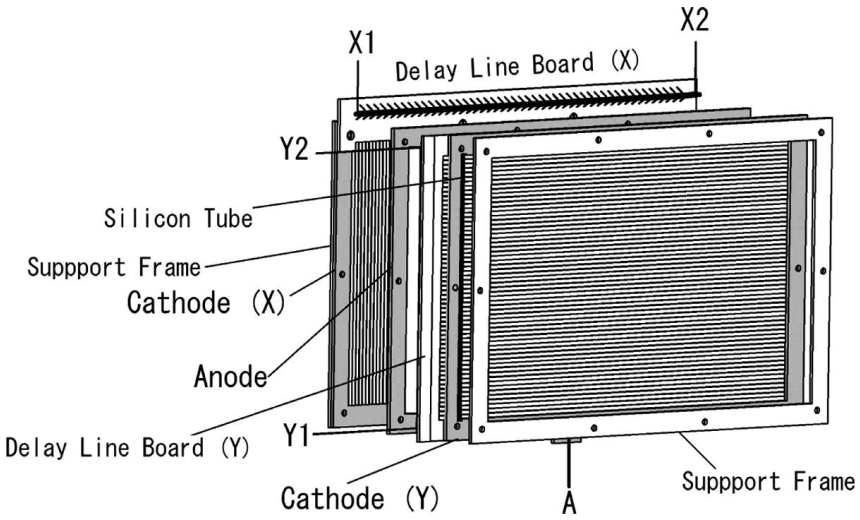

Figure 3.4.: Schematic view of the PPAC with the two cathodes and the anode. Reprinted from [KOF+13]. Copyright (2018), with permission from Elsevier.

amplification unit and after passing the discriminator they continue to a Time-to-Digital Converter (TDC). The position is then extracted from the timing by

$$x = k_x \frac{T_{x_1} - T_{x_2}}{2} + x_{\text{offset}}. \tag{3.5}$$

The y-position is extracted likewise. Here, T denotes the time, k_x the slope parameters for the delay-line, being in the order of 1.2 $\frac{\text{mm}}{\text{ns}}$. The offset parameter takes delay-line differences and geometrical misalignment into account. For consistency an event has a constant sum of timestamps, for this reason the quantity T_{Sum} defined as

$$T_{\text{Sum}} = T_{x_1} + T_{x_2} - 2T_{\text{Anode}} \tag{3.6}$$

can be used to veto background events stemming from δ-rays and multiple hits.

Multiple Sampling Ionization Chamber

The charge of the nucleus Z – the chemical element number – is determined using the energy loss of the ions in a gas. The energy deposition δE depends on the charge and velocity of the nucleus, compare to equation 3.3. The MUSIC detector measures

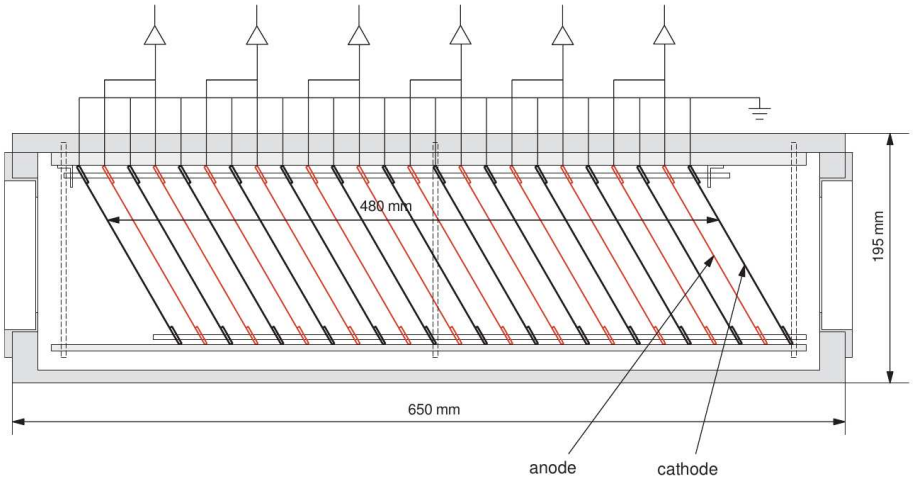

Figure 3.5.: A schematic view of a MUSIC detector is shown. The chamber is represented in gray, and the connected cathodes are black. The 12 anodes, shown in red, are bundled in two. The read-out channels are indicated. Reprinted from [KIK+05]. Copyright (2018), with permission from Elsevier.

the deposition and it is built up from thirteen cathode and twelve anode planes, see figure 3.5. The planes are placed alternating every 20 mm and are tilted by 30° to reduce the electron-hole recombination probability. The Aluminium chamber has a total length of 650 mm and is enclosed by 50 μm thick Kapton windows, see figure 3.5. A gas-mixture of Ar (90%) and CH_4 (10%) is used as filling gas. Two anodes are connected, resulting in six signals. The signals are passed through a shaping amplifier and are processed by a charge(Q)-to-Digital Converter (QDC). The cathodes are all connected to each other and have a common ground.
Two MUSICs have been used, one placed at F7 for the incoming and at F11 for the outgoing beam particles. To deduce the atomic number, the geometrical average of the signals is built and the element is identified based on the Bethe-Bloch-equation 3.3

$$Z = k\beta\sqrt{\frac{\Delta E}{\ln\frac{2m_e c^2\beta^2}{I} - \ln(1-\beta^2) - \beta^2}} + k_{\text{offset}}. \tag{3.7}$$

Here k and k_{offset} are calibration parameters, which have to be determined for each experiment, and I is a material constant.

Plastic Scintillators

To determine the velocity, thin plastic scintillators are placed in the beam at F3 and F7 for incoming and at F8 and F11 for outgoing particles. Each scintillator is read

out by two PMTs attached to it on the left and right. The signal of the PMT is split for time and energy measurements. The time signal is processed by a leading-edge discriminator and a multi-hit capable TDC. The time difference between the two PMT signals is proportional to the punch through point x

$$x = \frac{c_{\text{eff}}}{2}(t_1 - t_2), \tag{3.8}$$

with c_{eff} being the effective speed of light in the scintillator and $t_{1/2}$ the time stamp of the PMTs. The position can also be determined by the energy signals. They are related to the position of the energy deposition of the incoming particle. The relation is

$$\begin{aligned} q_1 &= q_0 \exp(-\frac{L/2 - x}{\lambda}), \\ q_2 &= q_0 \exp(-\frac{L/2 + x}{\lambda}), \end{aligned} \tag{3.9}$$

with $q_{1/2}$ the measured charge, q_0 the total charge, λ the attenuation length, L the length of the scintillator [Kno00]. The three equations above can be combined, leading to

$$\ln \frac{q_1}{q_2} = -c_{eff}(t_1 - t_2). \tag{3.10}$$

With this equation background events can be rejected.
For the timing the average of the time stamps t_1 and t_2 is used to reduce the dependency on the position. The TOF between the Focal Planes (FP) is then

$$\begin{aligned} TOF_{37} &= t(\text{FP7}) - t(\text{FP3}) + t^{37}_{\text{offset}} \\ TOF_{811} &= t(\text{FP11}) - t(\text{FP8}) + t^{811}_{\text{offset}} \end{aligned} \tag{3.11}$$

where the offset parameters have to be adjusted experimentally. For the velocity of the particle one needs to take into account the material budget in between. For the ZDS the velocity is given by

$$\beta_{811} = \frac{1}{c}\frac{L_{811}}{TOF_{811}}. \tag{3.12}$$

For the BigRIPS the wedge-shaped degrader has to be taken into account, which leads to

$$TOF_{37} = \frac{1}{c}\left(\frac{L_{35}}{\beta_{35}} + \frac{L_{57}}{\beta_{57}}\right). \tag{3.13}$$

The indices indicate the focal planes and L is the distance between the plastic scintillators.

Total-kinetic energy-counter

Another method to identify the mass of an isotope is to measure its total-kinetic energy. This is usually done with a scintillating detector. The0 TKE is placed at the end, as per design the beam is stopped by this kind of detector. The deposited energy in the detector depends only on the velocity and the mass of the incoming particle. Therefore, this method gives the opportunity to determine the mass independent of the charge. Note, that however the energy signal depends on the element number due to quenching effects. The effect describes the dependency of the light output on the incident energy deposition per unit path-length [Leo87].
The detector was placed to enhance the discrimination of the isotopes Sn-132 and Sn-129. The isotope Sn-129 is produced in the secondary target via three-neutron removal-reactions. Its charge state 49+ has a AOQ-value of 2.633 (Sn-129) similar to 2.640(Sn-132). The nominal resolution of the ZDS in terms of σ is about 1 ‰, having an overlap already in the 2 σ region.

3.3 In-beam γ-spectroscopy

When a reaction takes place in the target, the incident ion might be excited. The ion can de-excite by emitting a γ-ray after a time t. The time is of the order of about the lifetime τ of the state. If the flight length before de-excitation is small, the γ is emitted in or close to the target. The target area is therefore surrounded by γ-detectors. As the ejecting particle is moving, the energy of the photon is Doppler shifted. Knowing the velocity during the de-excitation process and the emitting angle this effect can be corrected by [Kno00]

$$E^{\gamma}_{\mathrm{CM}} = E^{\gamma}_{\mathrm{Lab}} \frac{\sqrt{1-\beta^2}}{1-\beta\cos\theta}. \tag{3.14}$$

E^{γ} denotes the energy of the photon in the reference system, CM the Center-of-Mass and Lab in the laboratory system. θ is the angle between the momenta of the projectile and the photon. If the scattering angle and the lifetime is small θ can be approximated with the angle of the detector in the laboratory frame with respect to the target center and the beam axis. The uncertainty of the E^{γ}_{CM} is given by

$$\begin{aligned}\left(\frac{\Delta E^{\gamma}_{\mathrm{CM}}}{E^{\gamma}_{\mathrm{CM}}}\right)^2 = &\left(\frac{\beta\sin\theta}{1-\beta\cos\theta}\Delta\theta\right)^2 + \\ &\left(\frac{\beta-\cos\theta}{(1-\beta^2)(1-\beta\cos\theta)}\Delta\beta\right)^2 + \\ &\left(\frac{\Delta E_{\mathrm{Intr}}}{E^{\gamma}_{\mathrm{Lab}}}\right)^2\end{aligned} \tag{3.15}$$

The first term in the equation refers to the angular resolution, which is mainly limited by the geometry of the detector and its distance in respect to the target. The second term represents the uncertainty of the momentum caused by straggling, energy loss in the target, and uncertainty of determining β of the projectile when emitting the γ. The last term is the intrinsic resolution, which is detector specific. It depends on the energy in the laboratory frame.
Figure 3.6 shows the energy resolution as a function of the emitting angle θ together with the different contributions of such a system. An intrinsic resolution typical for NaI-scintillator detectors and a velocity $\beta = 0.55$ comparable to the one in the experiment are chosen. The resolution, in this case, is dominated by the intrinsic resolution. The resulting energy resolution depends on the angular resolution of the detector system. As the photons are emitted isotropically in the CM-system they are mainly emitted in the forward direction in the laboratory frame due to the Doppler boost. For this reason a good resolution and high efficiency are required in the most forward direction, covering angles from 0° to 45°.
As already mentioned the spatial reconstruction resolution of the *x*-, and *y*-position at the target and its length limit the precision, resulting in a broader angular resolution. Moreover, the lifetime of the excited state may lead to a higher energy loss and straggling of the ion before de-excitation than expected. This influences the θ- and β-resolution, even further, as the emitting-point is shifted in beam-direction. To solve this problem active targets and vertex-trackers have been developed. Examples for the vertex tracker are the R^3B Si-tracker [BLT+16] and Minos [ODA+14].

3.4 γ detector

For the γ-detection an array of two different detector-types were used. In forward direction eight high efficiency $LaBr_3$:Ce crystals (LaBr) from HECTOR [GPR+13] are placed and 95 DALI2 [TMT+14] crystals cover the target at higher angles. This setup covers the full ϕ-range and in the θ-range from 30° to 150°. The full detector setup is shown in figure 3.7. In red are the LaBr represented, while in white the DALI2 crystals, and in violet the beam pipe together with the extension for the target chamber are shown.

3.4.1 DALI2

DALI2 stands for Detector Array for Low Intensity radiation 2 and is the follower of the original DALI setup, which was used before the accelerator complex of RIKEN was upgraded.
The DALI2 crystals are made of NaI(Tl) encapsulated with a thin MgO coating and a 1 mm Aluminium housing. They are read-out by Hamamatsu PMTs and are produced by three different companies with different sizes. 88 crystals are made by Saint-Gobain

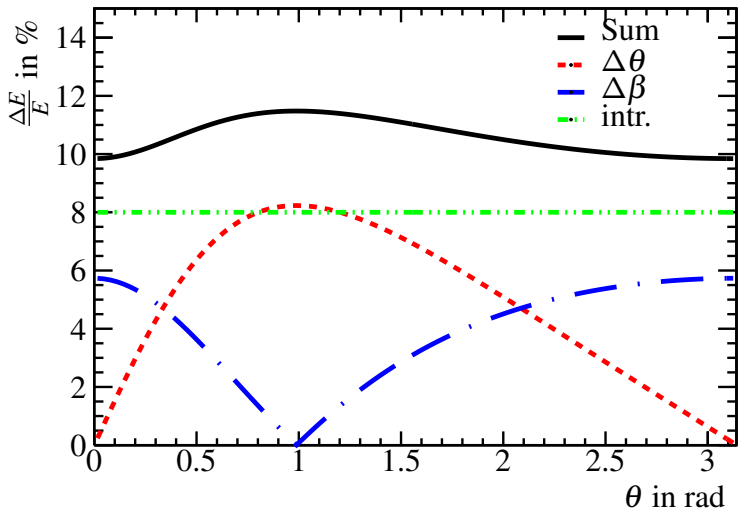

Figure 3.6.: Contribution to the uncertainty of the detected γ-rays due to the Doppler effect are shown for $\beta = 0.55$, an intrinsic resolution (intr) of 8%, typical for NaI-crystals, such as the used DALI2 detectors at an energy of 0.7 MeV, an angular uncertainty $\Delta\theta = 120$ mrad, and $\Delta\beta = 0.01$.

with a volume of 45 x 80 x 160 mm^3, 66 crystals are produced by Scionix with a volume of 40 x 80 x 160 mm^3, and 32 crystals are produced by Bicron with a volume of 60 x 60 x 120 mm^3. A summary is given in table 3.4 where also the number of used crystals is displayed. In addition, table 3.5 summarizes their geometrical distribution within the array. The resolution of the crystals is typically 8% FWHM for the Cs-137 γ-line at 662 keV.

The crystals are mounted on six metal planes resulting in eleven layers. Each layer corresponds to a different polar angle θ with respect to the target center and the beam line. The DALI2 array covered an angular range from 43° to 150°. The distance of the detectors to the target varied between 280 and 380 mm. Each layer covered the full azimuthal angle ϕ and the detectors were rotated and were overlapping in ϕ, see figure 3.7(b).

The crystals were powered by about 800 V to provide a dynamic region up to 30 MeV. The voltage was applied such that the crystals had a similar gain. The DALI2 signals were sent to shaping amplifiers and split into a timing and an energy branch. The energy signal was sent to an ADC, while the time signal was processed by a Constant Fraction Discriminator (CFD), and sent to a TDC.

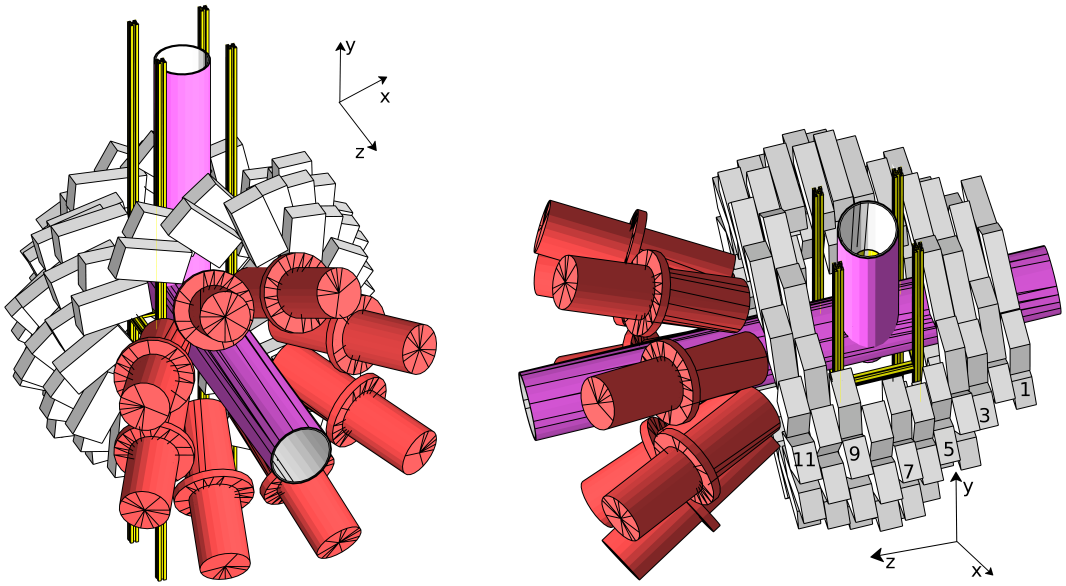

(a) beam-up direction (b) side view

Figure 3.7.: The used setup for detecting the photons from the reaction. In white the DALI2 crystals are presented and in the forward direction the LaBr from Hector, in red, are placed. The beam pipe is shown in violet and the construction to support the beam line at target position is displayed in yellow. 3.7(a) shows the setup looking from above against beam direction, while 3.7(b) shows the side view, also from above. Not shown are planes to hold the detectors.

Table 3.4.: Properties of the 3 different DALI2 crystal types and their connected PMTs.

Producer	#Crystals	# used Crystals	Size in mm^3	PMT	PMT ∅ in mm
Saint-Gobain	88	44	45 x 80 x 160	R580	38
Scionix	66	51	40 x 80 x 160	R580	38
Bicron	32	0	60 x 60 x 120	R1306	50

Table 3.5.: Distribution of the γ-detectors into 12 layers. The θ-angle and the radius with respect to the center of the target are listed. Sc stands for Scionix and SG for Saint-Gobain. The Bicron crystals were not used.

type	layer	#crystals	θ	distance to target-center in mm
DALI2 Sc	1	6	150.5°	339
DALI2 Sc	2	6	145.8°	296
DALI2 Sc	3	8	133.3°	284
DALI2 Sc	4	10	118.7°	302
DALI2 Sc	5	6	109.7°	282
DALI2 Sc	6	7	98.1°	319
DALI2 Sc	7	8	89.2°	351
DALI2 SG	8	8	80.8°	360
DALI2 SG	9	8	71.6°	356
DALI2 SG	10	14	62.3°	360
DALI2 SG	11	14	54.0°	378
LaBr	12	8	30.3°	436

3.4.2 LaBr Detectors

In forward direction under 30° with a distance of 436 mm the second γ-detector type, LaBr, is placed. Those large active volume detectors from HECTOR have 3.5" ($\approx$9.5 cm) diameter and a depth of 8" ($\approx$20 cm). As the detector has a huge density, they have a high detection efficiency and due to the large light output per deposited energy the resolution is one of the best for scintillators. The energy resolution is typically described by

$$\text{FWHM} = \sqrt{a + bE + cE^2}, \tag{3.16}$$

where the parameters can be identified: a with electronic noise, b with the scintillating light production, and c with and gain drift [GPR+13].

When using LaBr for γ detection its intrinsic radiation has to be considered. The detectors contain natural occurrence of the radioactive La-138 isotopes. And the chemical analogue of Lanthanum, Actinium, with its radioactive Ac-227 isotope contaminates the crystals. La-138 decays to Ba-138 through electron capture with a successive γ-ray of 1436 keV and an X-ray of 5 or 36 keV, depending on the electron shell. The detected energy is the sum of both photons. The other decay-mode is the β^+-decay, which produces a continuum and where Ba-138 emits a γ-ray of 789 keV. The Actinium contamination decays via a series of α-decays to Pb-207, see also figure 3.8. Due to quenching effects the light-output of the α-particles is reduced to about 2 to 2.6 MeVee (MeV electron-equivalent) [Wie]. On the one hand intrinsic radiation

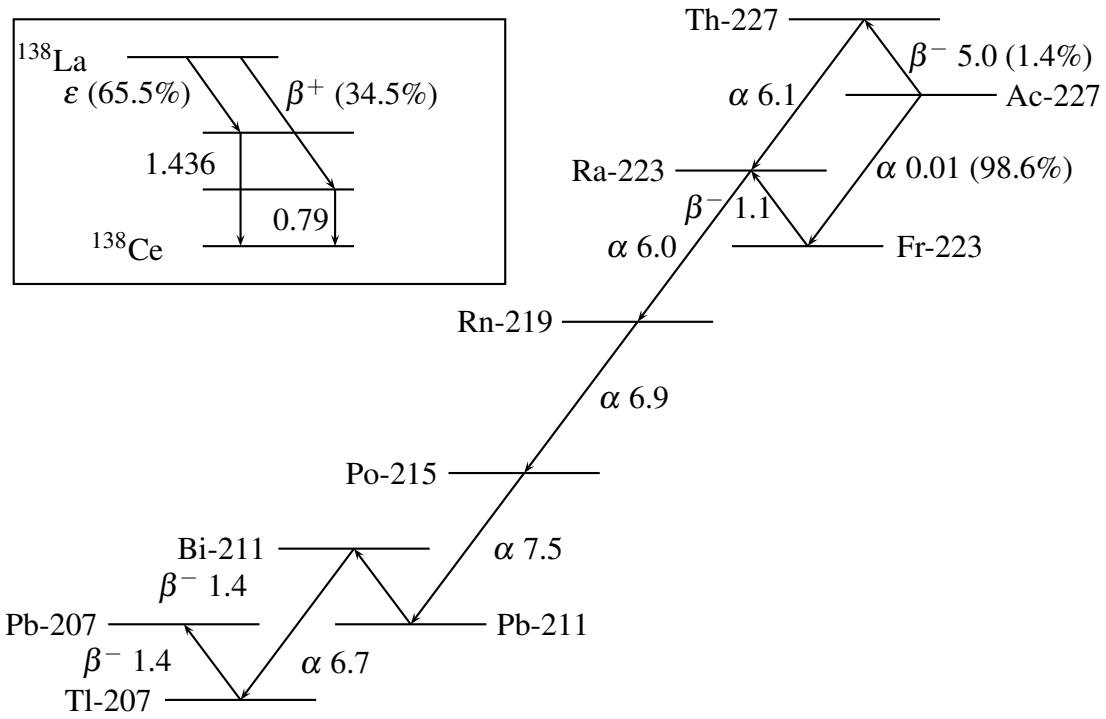

Figure 3.8.: The decays occurring in the LaBr crystals, intrinsic radiation, are displayed. For the decay chain of Ac-227 the Q-value is given in MeV. This chain causes the α background, which appears up to about 3 MeV electron equivalent. The decay of La-138 is shown in the upper left corner with emitted γ energies in MeV. The two decay modes are electron capture ε and β^+-decay.

reduces the sensitivity at low energy, therefore the trigger should be set above the intrinsic radiation. On the other hand the intrinsic radiation can be used for calibration and monitoring the gain stability [Wie, ZPM+17]. As we expect to have the states of interest well above these energies, the intrinsic radiation might only be a problem if the state decays in a cascade.

As the crystals have high efficiency, even for high energies, they are placed in most forward direction, because the Doppler effect boosts the photons in forward direction. The crystals compensate this by their good time and energy resolution. The detectors have a typical time resolution of about 0.5 ns and an energy-resolution of about 2% at 1.3 MeV in terms of FWHM. These scintillators are read-out by Hamamatsu R10233-1000SEL PMTs, afterwards the signal was divided, where one branch was processed like a DALI2 signal, The other branch is handled by a charge(Q)-to-Time-Converter (QTC) followed by a TDC.

3.5 Target

To perform the experiment, α-particles were chosen as target material. They are of isoscalar character and have spin 0. As such they predominantly excite isoscalar transitions in nuclear reactions. With their small charge number $Z = 2$, Coulomb excitation is negligible. Furthermore, helium is quite stable with the first excited state lying at 20.210 MeV. This 0^+-state could be clearly separated, if it was excited during the experiment. The neutron threshold is even slightly higher (20.58 MeV), whereas the proton threshold is lower located in energy (19.81 MeV) [nnd].

Target chamber

The target chamber CRYPTA, short for CRYogenic ProTon and Alpha target system, embodies the helium [RKM+05]. It is designed for a thickness of about 300 $\frac{\mathrm{mg}}{\mathrm{cm}^2}$. The gas had a temperature close to 4 K and a pressure of about $p = 85$ kPa. In figure 3.9 the transverse section together with the needed equipment is shown. The chamber consists of an Aluminium cylinder with length $l = 25$ mm and radius $R = 20$ mm. The two windows are made of a special foil, called Alloy foil, whose constituents are given in table 3.6 . This Alloy foil is designed to be thin and tear-resistant to withstand the pressure difference. To protect the chamber from heating up, the windows are further surrounded by an Aluminium foil. During the experiment the temperature and pressure were monitored and found to vary little over the time of the experiment. The pressure changed within the uncertainty while the temperature changed by less than 0.2 K. With these quantities the thickness of the helium-target can be determined. Taking into account the outwards bending of the windows due to the pressure difference between chamber and beam pipe. This outward bending can be described by a bulge function. For the effective thickness this function is then folded with the beam profile $f(r)$ to get the weighted thickness:

$$\frac{m}{A} = \rho d + 2 \int_0^R \omega(r) \cdot f(r)\, \mathrm{d}r. \tag{3.17}$$

Here m is the mass of the target, A the cross section, ρ the density of the target, d the length of the chamber, and $\omega(r)$ the bulge as a function of radius r. The windows contribute to the total cross section with a density of 8.3 $\frac{\mathrm{g}}{\mathrm{cm}^3}$ and a thickness $d = 10\,\mu$m. Adding the Aluminium foil with a thickness of 7 μm, corresponding to 1.9 $\frac{\mathrm{mg}}{\mathrm{cm}^2}$, results in a total window thickness for entrance and exit windows, of about 20.4 $\frac{\mathrm{mg}}{\mathrm{cm}^2}$. This additional material has to be considered when interpreting the data. Furthermore, both foils are not selective in means of the excitation mode, isoscalar or isovector. Therefore, the contribution of the foils was estimated with an empty-target run.

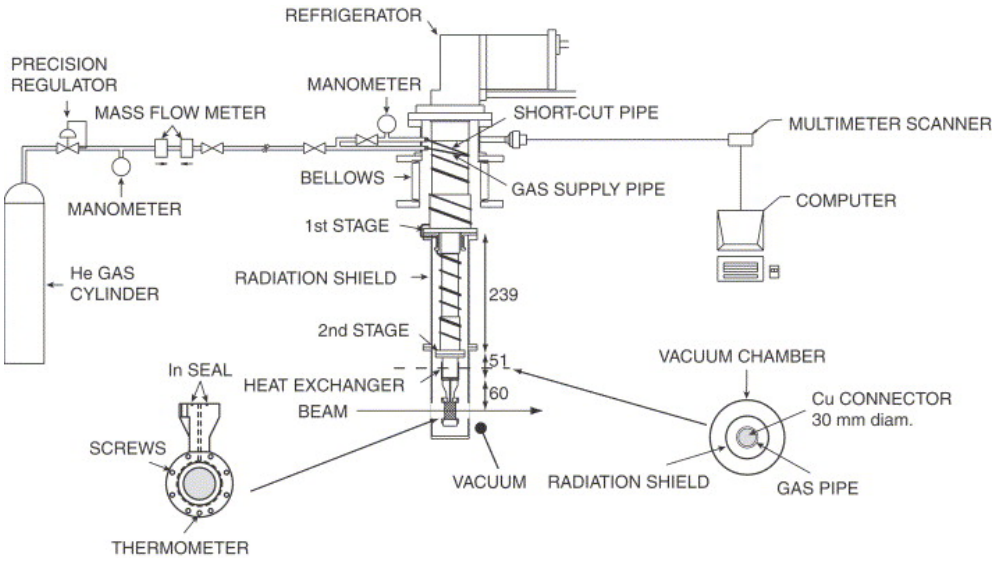

Figure 3.9.: Cross section of the target chamber with the needed equipment. Reprinted from [RKM+05]. Copyright (2018), with permission from Elsevier.

Table 3.6.: Composition of the Alloy-foil [Hamb].

element	mass portion in %
Co	42.5
Cr	20.0
Ni	13.0
W	2.80
Mo	2.0
Mn	1.60
C	0.20
Be	0.04
Fe	balance

Table 3.7.: The different DS-factors for experimental runs.

Beam	Target	run	DS
Sn-132	empty	1-3	1
Sn-132	empty	4-8	22
Sn-132	LHe	9-10	22
Sn-132	LHe	11-13	200
Sn-132	LHe	14-63	400
Sn-128	LHe	100-151	400

3.6 Data Acquisition System

In the experiment the RIBFDAQ was used as the Data AcQuisition system. It is provided by RIBF. Events were selected and recorded with different conditions. The so called minimum-bias trigger used was just a for a BigRIPS event. If the beam produced a signal in the plastic detector at F7 every n-th event was taken. The factor n was changed several times during the experiment. The factor is called Down-Scale (DS). There are also three different γ-triggers available, all of them are not DS and in coincidence with the plastic detectors located at F7 and F11. The triggers are LaBr-Or, DALI2-Or, and DALI2-Sum. For the Or-trigger each crystal was taken individually, while for the sum only the most forward layers (8, 9, 10, 11) are used, their signals are summed up. Based on the sum the trigger decision was made. The condition of two plastic detectors at F7 and F11 having fired, is called beam trigger. A schematic overview of the trigger system is given in figure 3.10.
The trigger window has a width of 2.5 μs with respect to the time stamp of the master trigger, which opens the gate for data taking. The data recording is blocked as long as the system is in busy mode. However, the DS-factors were chosen such that the lifetime was above 90%, they are summarized in table 3.7

3.7 Experimental Runs

To adjust the beam beforehand a *LISE++* [TB08] calculation was done to optimize for the transportation and purity of the beam. This was adjusted in-beam by the BigRIPS-team. First, the setting of BigRIPS for the isotopes Sn-132 and Sn-128 had been evaluated. With the start of each setting the ZDS magnets were set and optimized. First, the empty-target run was taken for almost 3 hours using only Sn-132 beam to estimate the contribution of the windows to the total cross section. Afterwards the target was filled and for each isotope about 23 h of beam time was taken. For the magnetic settings and the beam characteristics, see table 3.8.
The beam had an energy of about 207 MeV at target position and the energy loss through the windows was about 1 AMeV, while with a filled target the energy loss

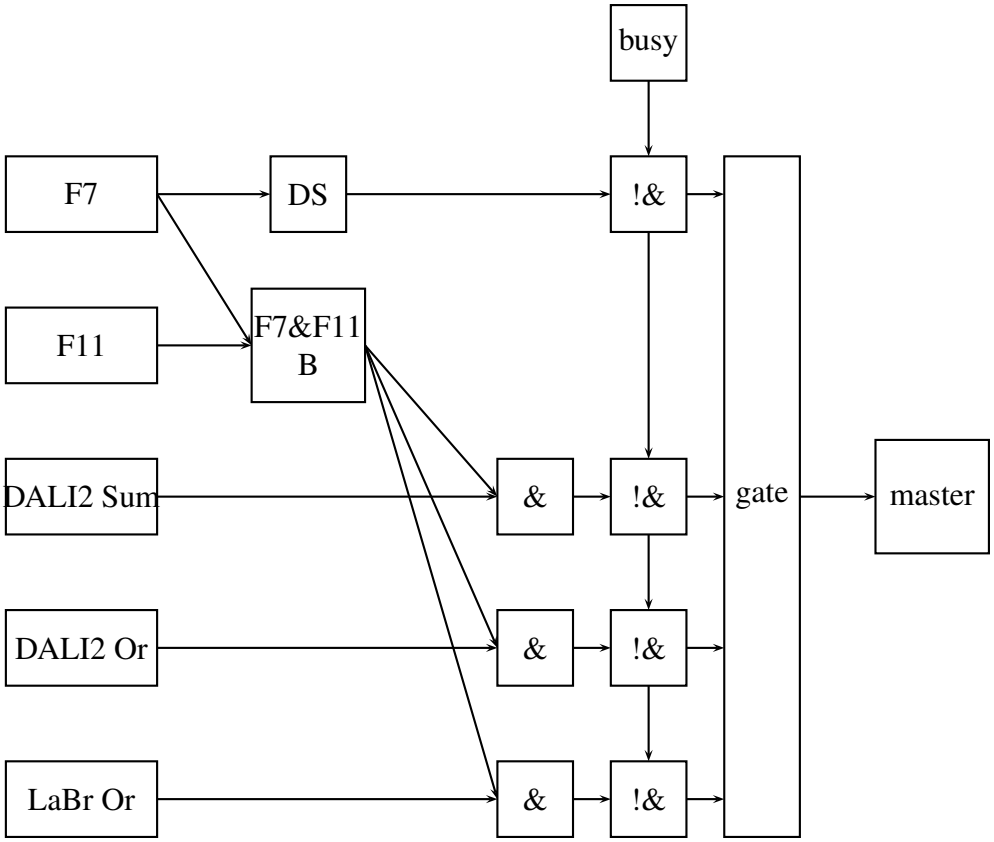

Figure 3.10.: The used triggers. F7 stands for the signal of the plastic detector at F7. The & is used for a coincidence, DS for Down-Scale, and B stands for Beam-trigger, both plastic detectors at F7 and F11 registered a hit in coincidence. The DS-factor was at the beginning varied, and later set constant to 400. The three different γ-triggers, LaBr-Or, DALI2-Or, and DALI2-Sum, are only used if coincident with a beam-trigger.

Table 3.8.: Summarized beam time and settings of BigRIPS and ZDS slits and magnets. The not mentioned slits had been opened to the maximum. For the magnet settings see also figures 3.2 and 3.3. Aluminium degraders are used at F1 and F5.

Device	Sn132 filled		Sn128 filled	
	left	right	left	right
F1 Slit	2	2	0	5.35
F2 slit	10	10	22	1
F5 slit	40	30	20	20
F7 slit	25	25	6	4
Degrader F1 in mm	6		4.5	
Degrader F5 in mm	1		1	
D1 in Tm	7.441		6.992	
D2 in Tm	6.219		6.043	
D3 in Tm	6.211		6.032	
D4 in Tm	6.178		6.006	
D5 in Tm	6.179		5.745	
D6 in Tm	5.917		1.866	
D7 in Tm	5.919		5.604	
D8 in Tm	5.750		1.298	
purity in %	36.6		28.3	
beam time in h	22:48:36		22:46:25	

was about 30 AMeV. The energy loss through the target was a bit higher than expected and resulted in an effective thickness of 335(2) $\frac{\text{mg}}{\text{cm}^2}$, see for more details section 4.3.

3.8 Simulation

In order to interpret the derived γ-spectra from the experiment a simulation, called shogun-sim [PD], based on Geant4 [AAA+03] was used. The simulation allows to evaluate the response. The spectra are produced in three steps. First, a beam is impinging on the target and a defined reaction takes place. Second, the ejected particles are transported and are interacting with matter, corresponding to the chosen theoretical models. The energy deposition is folded with the detector resolution. Third, the same algorithms as for the experimental data are used to reconstruct the events and analyze the simulated data.
In the first step the projectile, ejectile (such as γ's), and the target are defined. The beam start-conditions are randomized. Their distribution was adapted to be similar to the experimental, angular, spatial, and β profile using distribution functions indepen-

dent from each other. The energy loss due to material budget is simulated accordingly, and the interaction point is uniformly distributed over the target length, while the ejection point of the γ-rays is set with an exponential distribution, with the given halflife time, after the interaction point. The Atomic-BacKGround (abkg) can be simulated, too. Therefore a calculation specific for the target and projectile was performed for the input parameters by D. Rossi [Ros] using script, called abkg. As input parameters are the energy, mass, and chemical element number used. The script accesses a database for x-ray transitions in atoms.
In the following second step the setup is built and simulated. Here, the interactions of γ-rays with matter and the energy deposition in the detectors are simulated. Also the responses of the γ-detectors, the reconstruction of interaction point, and β-resolution are simulated by Gaussian distribution. Here, experimental data from source measurements are taken into account to modify the energy-resolution of the crystals in a realistic manner.
In the third step the events are reconstructed, using all methods like in the real event reconstruction, see section 4.4.3. Also the efficiency calculated with the simulation is compared to the experimentally evaluated efficiency using an Y-88 source, see section 4.4.5.

4 Data Analysis

This chapter describes the performed data analysis. It starts with the analysis of the beam, calibration of in-beam detectors followed by isotope-identification, transmission-rate, and determination of the target thickness. Afterwards the analysis steps done for the scintillating crystals are described, calibration of energy and time stamps, clustering detectors for add-back routine, and reconstruction of the reaction point to obtain the emitted energies in the frame of the moving isotopes. At the end of this part the efficiency is evaluated with a source measurement and the simulation is compared to it.

4.1 BigRIPS and ZeroDegree Spectrometer

The analysis for BigRIPS and ZDS are similar and follow the same structure. Their analysis is ordered in two steps. In a first step, the in-beam detectors, PPAC, Plastic, MUSIC, and TKE are calibrated and background-rejection procedures for detectors are investigated. In the second step, the beam is reconstructed to eventually identify the in- and outgoing particles.

4.1.1 Position Measurement

The beam positions at the different focal planes of the beam are inter- or extrapolated using PPACs[1]. Making use of equation 3.5, the position in x- and y-direction is determined on each PPAC. A check for the linearity of the PPACs was done using the plastic detectors. The time difference between the PMTs signal of each detector should be linearly correlated to the x-position of the closest PPACs, before and after the plastic detector. A behavior that is shown in figure 4.1(b), the evaluated positions in the detectors are strongly correlated. To remove background events equation 3.6 was used. This equation is a consistency check to reject for example δ-electrons. In figure 4.1(a) a T_{Sum}-spectra can be seen for the first PPAC at F7. A rather broad gate was used to maximize statistics. An event is rejected, if less than two PPACs at one focal plane fire or rather less than two signals are accepted.
Another important point of the PPACs is their efficiency. As they are always doubled, the efficiency is evaluated using one of them as a gate for the other one and vice versa. Counting the number of events in PPAC A and in the case both PPACs, A and B, register an event, the efficiency p for PPAC B is given by their ratio $p_B = \frac{B}{A \cap B}$. This results in an efficiency of more than 90% for almost all PPACs, see figure 4.2. As for the

[1] Depending which PPACs fired at a focal plane

reconstruction of the beam trajectory the position at the focal plane is important, two PPACs per focal plane are at least needed to extrapolate the trajectory, justifying the above described event-rejection. Therefore, the beam is reconstructed with almost an efficiency of 100%, as there are at each focal plane four PPACs.
Starting from run 49 the leakage current of PPAC 7 at F3 started to rise and the detector was shut down later at the beginning of run 53.
The precision of the PPACs was estimated using the doubled PPAC structure. With the first PPAC-pair the position and angle was determined. Using those quantities the expected position on the next PPAC can be calculated. The distribution of the difference between the propagated and measured value is directly connected to the resolution of the PPACs. The difference D is given by

$$\begin{aligned} D &= \left(x_1 + \frac{d_2}{d_1}(x_1 - x_2)\right) - x_3 \\ \Delta D &= \sqrt{\left(\left(1 + \frac{d_2}{d_1}\right)\Delta x_1\right)^2 + \left(\frac{d_2}{d_1}\Delta x_2\right)^2 + \Delta x_3^2} \end{aligned} \tag{4.1}$$

with d_1 being the distance of the first two PPACs, d_2 the distance of the first PPAC to the third PPAC, and $x_{1/2/3}$ the measured position on the different PPACs. Assuming that the uncertainties for all PPACs are equal $x_1 = x_2 = x_3$, as they are of the same type, the uncertainty of one PPAC is then read as

$$\Delta x = \frac{1}{\sqrt{2 + 2\frac{d_2}{d_1} + 2\left(\frac{d_2}{d_1}\right)^2}} \Delta D. \tag{4.2}$$

With the values at F8, $d_1 = 37.4$ mm, $d_2 = 500$ mm, and $\Delta D = 9.03$ mm this results in a resolution of 0.46 mm (FWHM) for one PPAC and to 2.33 mm for the target position in x- and y-direction. For the target position the assumption is made, that all PPACs fire and that the reaction takes place at the target center with a distance of 1518 mm from the first PPAC pair. For the calculation of the PPAC resolution the implicit assumption of no struggling or almost no angular broadening was made.

4.1.2 Time-of-Flight

By using plastic detectors the (TOF) was measured between F3-F7 and F8-F11 for the incoming and outgoing beam, respectively. To remove background a consistency check according to equation 3.10 was performed. For all four plastic detectors the plots of $(t_2 - t_1)$ versus $\ln \frac{q_1}{q_2}$ are shown in figure 4.3. To remove further background gates for the time stamps of each PMT were set. The time of the signal is then calculated to be the mean value of the remaining PMT signals. The time offset of the detectors to

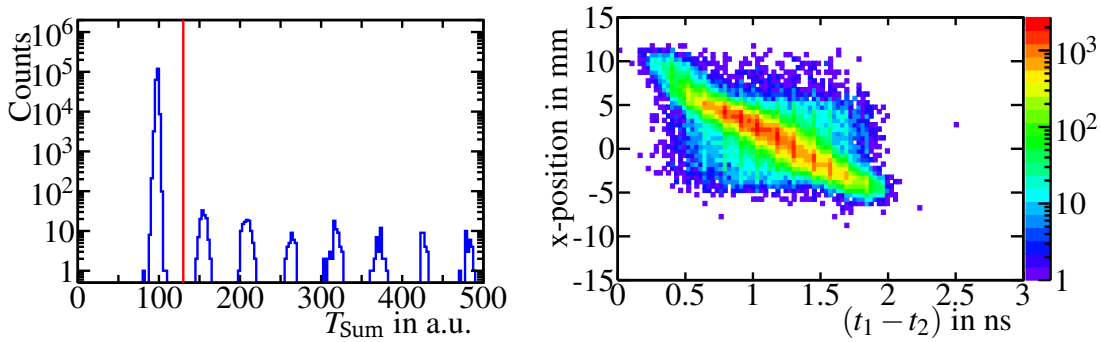

(a) T_{Sum} check of PPAC (b) PPAC versus plastic detector

Figure 4.1.: The left figure shows the consistency check based on equation 3.6 for PPAC 18 at F7. Events with T_{Sum} smaller than 130 a.u. are accepted, the red line marks the upper acceptance limit. The gate was applied to reduce the background. The right figure shows the correlation of the reconstructed x-position using the same PPAC versus the time difference of the two PMTs of the plastic detector at F7. As the time difference is proportional to the x-position a linear correlation is visible. Note, that the background in this figure is not suppressed.

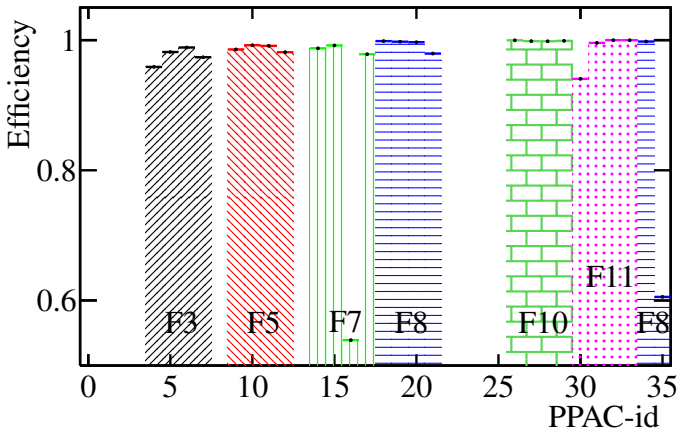

Figure 4.2.: The PPAC efficiency is displayed for Sn-132 isotope setting. The difference of the PPAC efficiency between the settings is not visible, except for PPAC 7 at F3, which was shut down. The efficiency is higher than 95%. The drop for PPAC-16 was caused by a damage of the detector. The reconstruction efficiency for the beam is even higher, as per focal plane only two PPACs are needed. The last PPAC pair, 34 and 35, was located just after the target at F8. It was used to reconstruct the emitting angle, see figure 4.23.

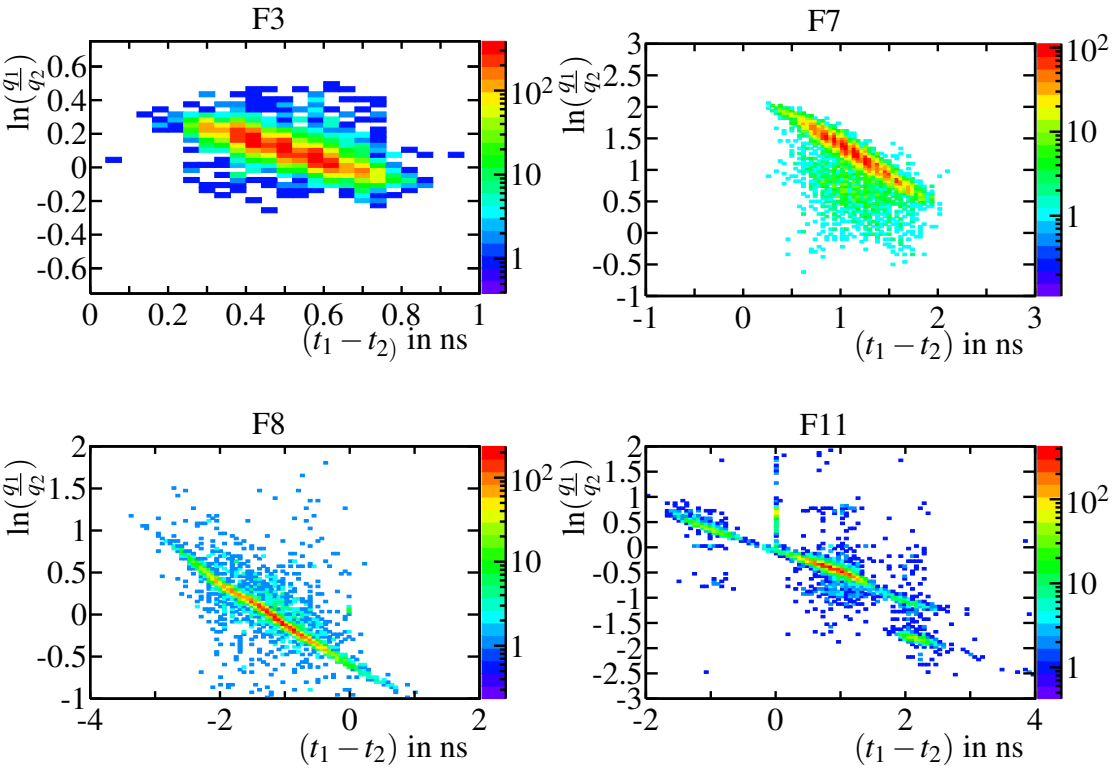

Figure 4.3.: For all plastic detectors the correlation between energy signals and time difference of the PMTs of one plastic detector according to equation 3.10 is shown. For all the plastic detectors this correlation is shown. The detector at F11 shows an artefact for time differences equal to 0. These inconsistent events were rejected.

each other was evaluated with the centered Sn-132 beam. The energy dependence of the time signal was investigated and found to be negligible.
In order to measure the TOF it is necessary to determine the time offset between the detectors at F3 and F7, and F8 and F11. The offset takes the delays in electronics and different path lengths into account. The offset parameter was determined by evaluating the AOQ-spectra with different time-offset values. The centroid of the identified Sn-132 nuclei is estimated by a Gaussian fit. The fit and centroids as function of the offset parameter are shown in figure 4.4. A linear function is used to specify the offset. The best fitting offset-value can be selected. For the BigRIPS a time offset of 299.74 ns, while for the ZDS an offset of -158.54 ns were taken. The time resolution of the plastic detectors is estimated using the spread of the velocity difference in the empty-target runs. The velocity at target position is determined with a precision of $\frac{\Delta\beta}{\beta} = 0.22\%$ (FWHM).

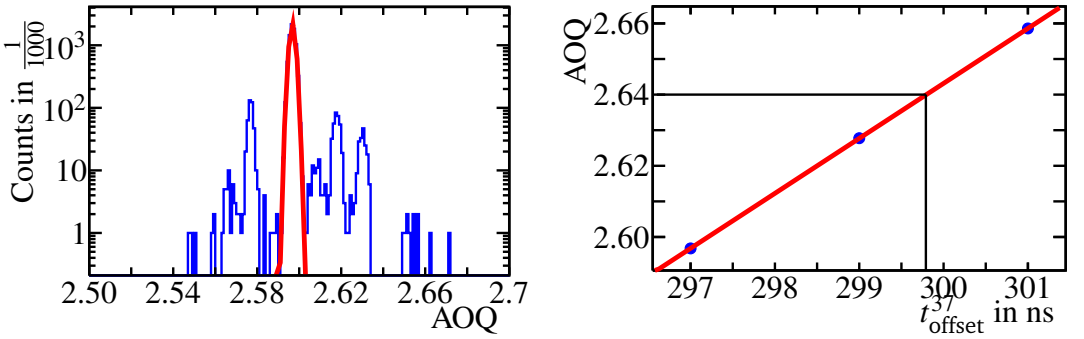

(a) (b)

Figure 4.4.: Determining the time-offset parameter. Shown here, as an example, is the BigRIPS-spectrometer time-calibration. Panel 4.4(a) shows the AOQ spectra for tin-isotopes with a time offset of 297 ns. A Gaussian fit was applied to get the centroids of the isotope of interest, Sn-132. Panel 4.4(b) shows the variation of the centroids with the offset parameter. A linear fit is applied to determine the overall offset which is marked by the black lines.

4.1.3 Energy Loss

The energy deposition ΔE in the MUSIC was obtained by the geometric average $\Delta E = \sqrt[n]{\prod_{i=1}^{n} e_i}$ of the anode signals e_i. The calibration parameters, k and k_{offset}, in equation 3.7 were then fitted to the spectra. Gating on the AOQ-value, introduced later, the peaks can be assigned to the chemical element. Using this information, the parameters of equation 3.7 are adapted. As the calibration was done already during the beam time to watch data taking the slope is equal to 1, see figure 4.5. Further, the energy-deposition was checked for spacial, angular, and β dependencies. As an example see figure 4.6(a), where the energy deposition in the MUSIC at F11 versus the angle in the x-z-plane is shown. The dependency is corrected by a linear fit to the region corresponding to $Z = 50$. The same procedure was done for both MUSIC-detectors for all mentioned variables.

During the runs a shift for energy signals of both MUSICs was observed and corrected by an offset for the geometrical average of the deposited energy in equation 3.7, leading to

$$Z = k\beta \sqrt{\frac{\Delta E + E_{\text{offset}}}{\ln \frac{2m_e c^2 \beta^2}{I} - \ln(1-\beta^2) - \beta^2}} + k_{\text{offset}}. \tag{4.3}$$

The offset is time dependent and caused by temperature and/or pressure change [Doo]. For each run a new offset was derived. The change of the offset can be seen in fig-

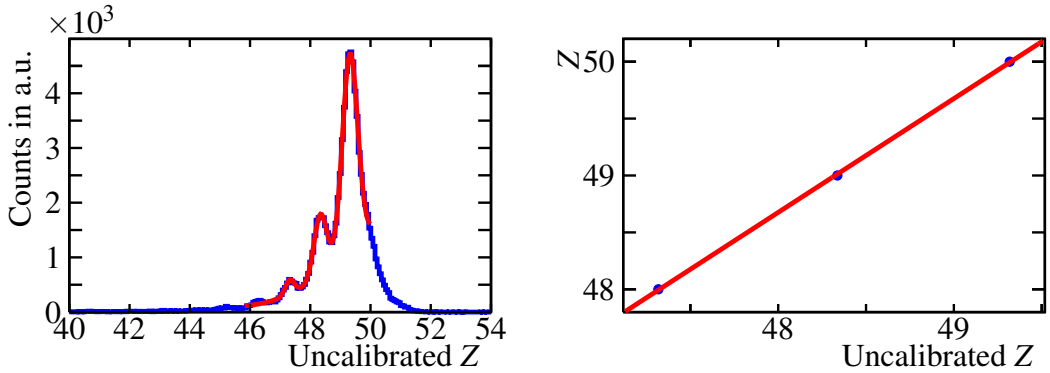

Figure 4.5.: Calibration of the MUSIC at F11. Left is the uncalibrated Z-distribution which was fitted with a sum of Gaussian functions to evaluate the mean energy deposition for each chemical element. The right figure shows the linear fit to the centroids of the peaks. Through the fit the calibration parameters are obtained.

ure 4.6(b). The obtained resolution is 1.22% and 1.50% in FWHM for the incoming and outgoing particles, respectively.

4.1.4 Total-Kinetic Energy

The energy deposition in the TKE counter was inspected. As expected a dependency of the total energy to the velocity for tin is observed as the energy depends on the velocity and mass, see figure 4.7. Selecting in ZDS once Sn-132 and once Sn-129 beam, the energy signal in dependence of the velocity β was studied. This leads to the marked areas. Further investigations of angular and position dependency were started, but they failed to improve the resolution. The decision was made to skip this detector for event selection, as not even the particles Sn-132 and Sn-129 can be distinguished, based on their energy deposition as a function of their velocity.

4.2 Event Selection

With the data, obtained from the calibrated detectors, the AOQ-value is calculated and the isotopes are determined specifically on an event-by-event basis. Three possibilities exist for evaluating the AOQ-value, for both spectrometers BigRIPS and ZDS. The evaluation for BigRIPS can be performed with three different possible combinations of the two stages: the single use of F3 to F5, F5 to F7, or a combination of both. For ZDS the possibilities are to use F8 to F10, F10 to F11, and combine both (F8 to F11). The TOF-detectors and therefore the flight-length are fixed to F3-F7 in the cases of

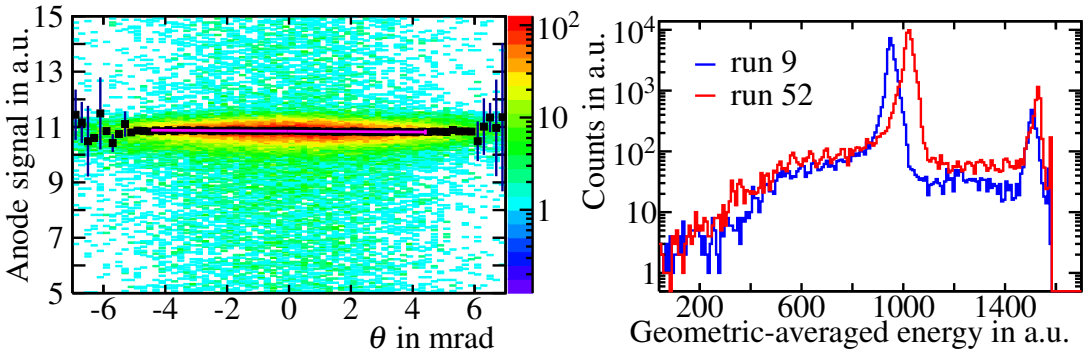

(a) Angular correction of the MUSIC

(b) Drift of the energy signal

Figure 4.6.: Correction of the dependencies of the MUSIC at F11. Panel (a) shows, as an example, the angular dependency of the deposited energy signal of the last anode pair. To improve the Z resolution a linear fit (purple) was performed to correct the dependencies. Each slice of the histogram was fitted with a Gaussian to get the centroid (black rectangles). The same was done for the spacial- and β-dependencies. Panel (b) shows the geometric mean of the energy signal with a gate set for AOQ values corresponding to Sn-132. The data are from run 9 and run 52, corresponding to the start and almost the end of the Sn-132 beam time with filled target. The changes from run to run are corrected by adding an offset parameter to the average energy-signal. The variation corresponds to a shift of 5 Z-units during two days.

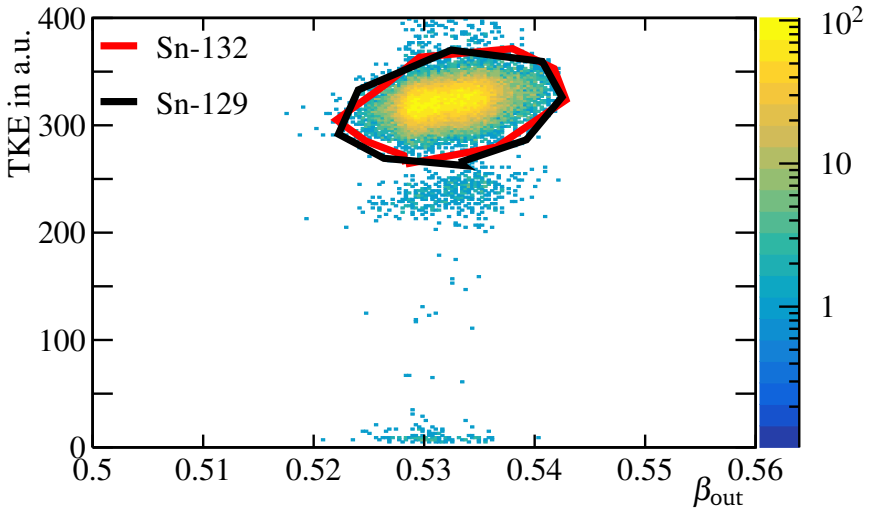

Figure 4.7.: Light yield of TKE counter versus β. The red and black ellipse show the region for outgoing Sn-129 and Sn132 particles, identified with ZDS. Due to the huge overlap this method was not used.

BigRIPS and F8-F11 in the case of ZDS. The differences of the resulting values are shown in figure 4.8 for the ZDS for F8-F10 and F8-F11. For BigRIPS the identification method F3-F7 is used as it gives the best resolution, although the methods show similar resolutions. In the ZDS F8-F11 is chosen, but both methods show comparable resolutions after correction, which will be introduced in the next paragraph.
The AOQ-value resolution can be further increased by introducing corrections to compensate for aberrations. Selecting the tin-isotopes of interest, the dependency of the AOQ-value on the different variables, angle and position, at the different foci are considered and corrected using polynomials. An example is shown in figure 4.9 for the x-position-dependence at F11 (ZDS). The obtained resolutions for AOQ and chemical element Z, defined as $\frac{\Delta AOQ}{AOQ}$ and $\frac{\Delta Z}{Z}$ in means of FWHM, are listed in table 4.2. These values correspond to the design values of the spectrometers. In figure 4.10 the achieved improvement is shown for ZDS, selecting incoming Sn-132 ions.
To reject events with a charge change of the ion during the flight another selection criteria based on the $B\rho$ difference is applied. If the $B\rho$ changes it affects the trajectory. This change δ with respect to the central trajectory is monitored and should stay almost constant. If this does not hold true it indicates an alteration of the magnetic rigidity. This may be caused by electron capture or other reactions with, *e.g.*, the in-beam detectors. This method can be applied for both spectrometers but is expected to happen mainly in the ZDS as the energy is lower than before the target in BigRIPS. An example is shown in figure 4.11. The δ is compared for Sn-132 between the focal planes F3 and F7 (BigRIPS), and F8 and F11 (ZDS). Several linear correlations are visible.

Table 4.1.: Number of gated events for the incoming and outgoing beam. The last row is the calculated amount of gated ions.

		Sn-132	Sn-128
incoming	beam trigger	1673573	637621
	γ-trigger	8930473	3504218
	DS x beam + γ-trigger	555505087	258552618

The correlation crossing (0/0) is the no charge-changing branch, which is selected to enhance the identification.
For the atomic number no further corrections are applied, as this was already done during the evaluation of the energy deposition in the MUSIC. The elemental number was calculated according to equation 4.3.
Incoming particles were accepted, if the AOQ-value was within a 2.2 σ window around the isotope of interest. No further Z criteria is applied as the beam was rather clean. The incoming beam is extrapolated to the target center in order to ensure that the ions travel through the target gas and are not hitting the target chamber. If the beam is within a radius $r = 18$ mm around the target center and the incoming angles in x-z- and y-z-plane are within 20 mrad and 40 mrad, respectively, the incoming ion is accepted.
The outgoing particles were selected using an elliptical selection in the AOQ versus Z plot. The ellipse had radii of 2.5 and 2.0 in terms of σ for AOQ and Z, respectively. Additionally, the no charge-changing branch was selected. An overview of the conditions are listed in table 4.3.
The γ-spectra were obtained by requiring the γ-trigger, DALI2 Or, DALI2 Sum, and LaBr Or, see section 3.6. This resulted in the number of events listed in table 4.1.
Furthermore, using the empty-target run, the transmission rate was estimated. Comparing the number of ions at F7 plastic before the target to the number of ions at F11 after the target results in an overall transmission rate of 97.6%, for the tin ions within the geometric acceptance-cut. For this, the dependence on the position and incident angle have been investigated and afterwards folded with the beam profile of the runs with the filled target. The acceptance as a function of the x-position and angle is shown in figure 4.12.

4.3 Target Thickness

For the estimation of the target thickness two methods were used, the thermodynamic and the energy-loss method. For the first mentioned method the temperature and pressure were observed, while the other one uses the difference in velocity before and after the target. Both methods give results which are in agreement with each other.

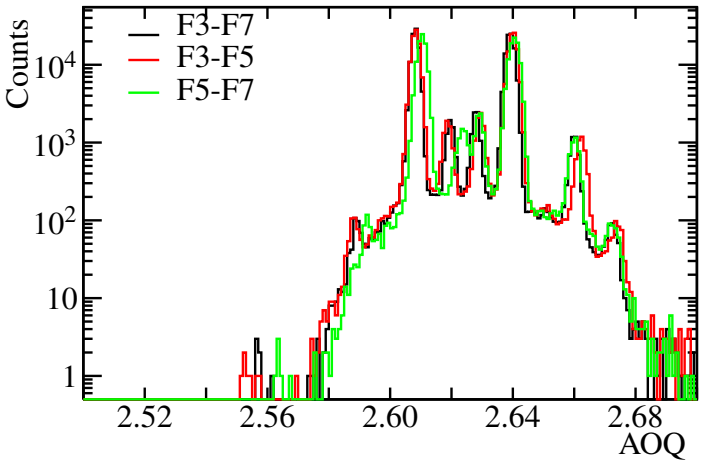

Figure 4.8.: Different combination of PPAC-detectors in BigRIPS to determine the AOQ-value.

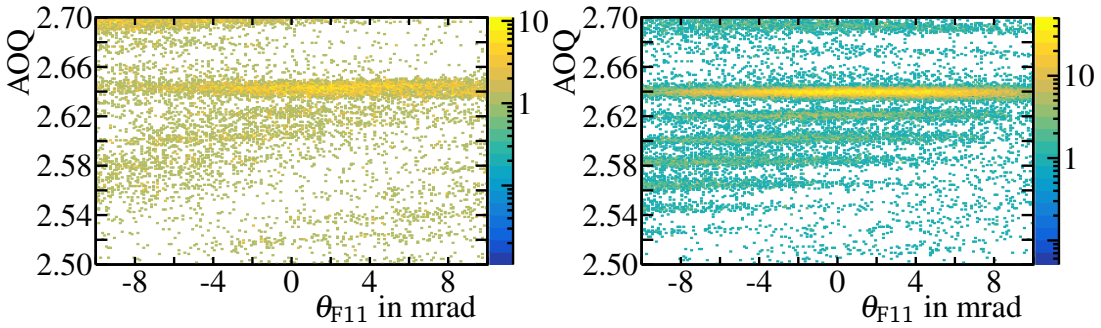

(a) no correction applied

(b) all corrections applied

Figure 4.9.: Correction of the AOQ dependency. Panel (a) shows the dependence of the AOQ-value with the x-position for the tin-isotopes at F11. A polynomial was fit to the plot and subtracted from the AOQ-value. Panel (b) shows the result after the applied corrections of all variables.

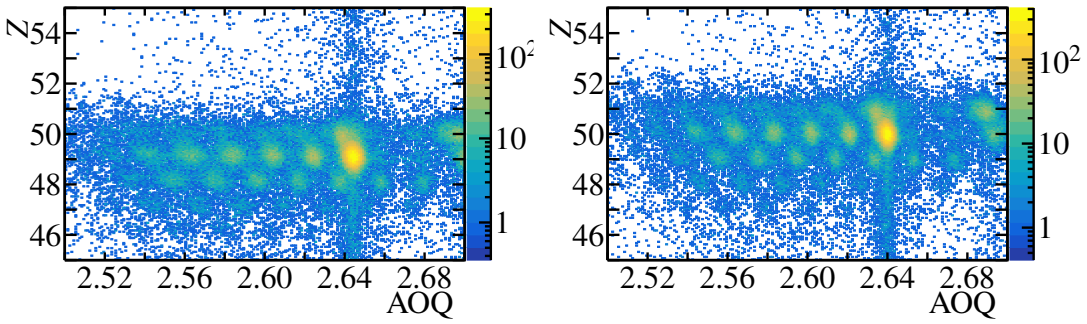

(a) no correction (b) all corrections

Figure 4.10.: Particle identification before and after applying the corrections in the ZDS. Left panel shows the particle identification before the correction, while the right panel shows the same after applying all used corrections.

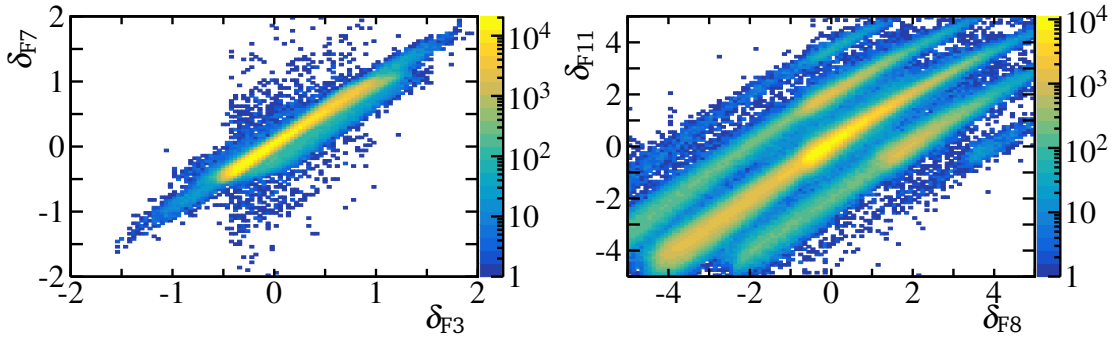

(a) BigRIPS (b) ZeroDegree

Figure 4.11.: Identification of ions changing their magnetic rigidity, mainly due to electron-capture or stripping, see text. The correlation crossing (0/0) corresponds to no changes in magnetic rigidity (no charge-state change). In panel (a) the difference for the BigRIPS spectrometer to the central trajectory at F3 versus F7 is plotted. While in panel (b) the same is displayed for the ZDS at F8 and F11.

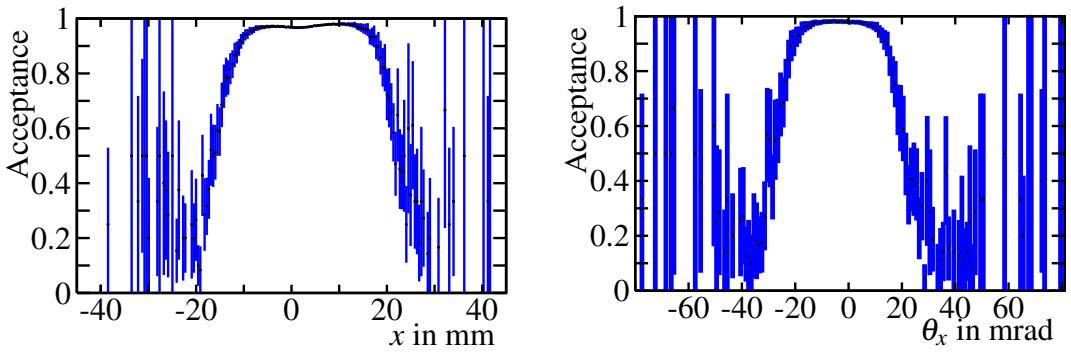

(a) (b)

Figure 4.12.: Acceptance of the ZDS for Sn-132 ions. This plot is created by dividing the distributions at F8 of incoming ions and ions reaching F11, which are identified as Sn-132 particles. The empty-target runs are used. An acceptance of 97.6(2)% within the selection criteria was achieved.

Table 4.2.: The obtained resolution for the particle identification in terms of FWHM. For the different settings the resolutions are listed with the range. The resolution gets worse with increasing run number as the detectors degenerate. The best resolution was always achieved in the first run. The decrease of the BigRIPS resolution is due to the damage of the PPAC 7 at F3.

	BigRIPS in %	ZDS in %
AOQ	0.18 - 0.40	0.20 - 0.23
Z	1.0 - 1.2	1.4 - 1.5

Table 4.3.: Here are the selection criteria for incoming and outgoing ions listed.

	incoming	outgoing
AOQ in terms of σ	2.2	2.5
Z in terms of σ	-	2
δ	-	$\lvert\delta_{\mathrm{F8}} - \delta_{\mathrm{F11}}\rvert \leq 0.9$
TKE -	-	
r in mm	≤ 18	-
θ_{xz} in mrad	≤ 20	-
θ_{yz} in mrad	≤ 40	-

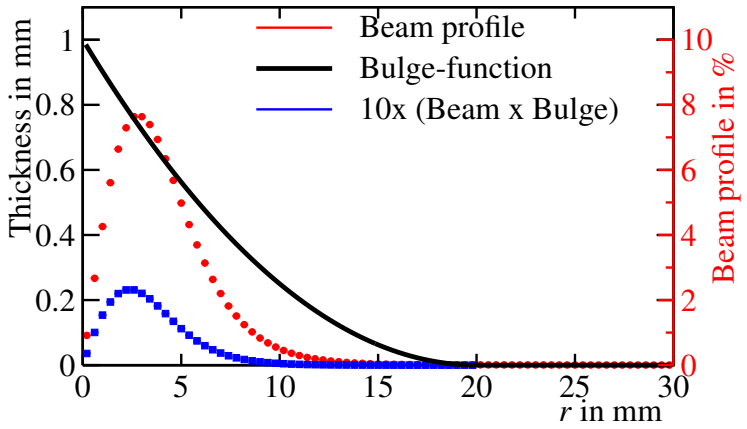

Figure 4.13.: Weighting the beam profile with the bulge-function of the window returns the effective additional depth of the target-chamber. The integral of the folded function results to 0.36 mm.

T and p Method

The temperature and pressure within the liquid-helium target were monitored during the experiment. Those quantities were stable during the experiment with values of $T = 3.93$ K and $p = 78.1$ kPa. As the pressure in the target chamber is higher than in the beam pipe, the windows are bulged. The maximum bulge was measured after the experiment in the laboratory to be a =1 mm. The bulge-function used is

$$\omega(r) = a \cdot (1 - \frac{r}{R})^2 \tag{4.4}$$

with R the maximal radius of the target chamber. Weighting the function with the beam profile over the target-chamber diameter results in an effective target-length of 25.72 mm, see figure 4.13. The contribution of one bulged window to the total length is 0.36 mm (1.5%). The density of the helium filling is determined to 130.1(5) $\frac{\text{mg}}{\text{cm}^3}$, resulting in an effective thickness of 334.6(21) $\frac{\text{mg}}{\text{cm}^2}$. The uncertainty estimation takes into account the temperature, pressure, and bulge-maximum a, the uncertainties are $\Delta T = 0.2$ K, $\Delta p = 1$ kPa, and Δa =0.1 mm.
As a reminder: The windows add to the total thickness two times about 8.3 $\frac{\text{mg}}{\text{cm}^2}$ for the Alloy- and about 1.9 $\frac{\text{mg}}{\text{cm}^2}$ for the Aluminum-foil, see section 3.5.

Energy-loss Method

Using the measured velocity β in BigRIPS and ZDS the energy loss can be calculated and the thickness of the target is evaluated. The calculation was done using *LISE++*.

Table 4.4.: Listed are the used sources with their main emitted γ energies to calibrate the crystals.

Sources	Energy in keV
Co-60	1173
	1332
Y-88	898
	1836
Cm-C	6130

Before and after the target the velocity β was 0.585 and 0.532, respectively. This results in an effective target thickness of about 340(40) $\frac{\text{mg}}{\text{cm}^2}$. Here the uncertainty is higher, due to the broadening and uncertainty of β.
The results of both described methods are in agreement with each other within $1\,\sigma$. Furthermore, they agree with the measurement of N. Nakatsuka [NHB17]. They used the same target one month later in the same campaign.

4.4 γ-Detection

4.4.1 Energy Calibration

For the energy calibration of the crystals the γ-sources Co-60, Y-88, Cm-C, and Ni+Cf haven been used, see table 4.4. The Cf+Ni source was used only for the LaBr as the time after the experiment was limited and the plates had to be placed in front of the crystals to get a higher rate. Further, the transition caused by neutron caption of the Ni nuclei was not observed. Instead the transition of Aluminium capturing a neutron and decaying afterwards with about 7.1 MeV was evident. The calibration measurements were taken before and after each setup and during beam breaks. The sources were placed on the beam pipe at different positions for the backward and forward detectors. The length of the calibration runs vary with the sources and available time, 10 to 30 minutes. After the experiment Y-88, was placed at the target center to evaluate the efficiency of the two arrays.

DALI2

The DALI2-crystals were calibrated using Y-88 and Co-60. To the energy spectra a second order polynomial together with a Gaussian was fitted to obtain the mean value of the transition peaks. The spectra together with the fit, for an Y-88 source, are shown in figure 4.14. Using all four transitions of the sources the crystals are calibrated using a linear fit, see figure 4.15(a).

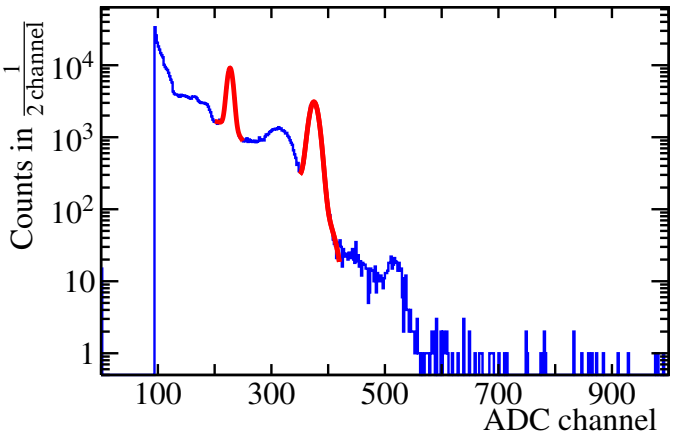

Figure 4.14.: The raw spectra taken with an Y-88 source with DALI2 before the empty-target runs, the two photopeaks were fitted with a Gaussian and polynomial second order .

The change of the detectors' gain is investigated. The gain drift can be explained by different causes: Radiation might damage the crystals, as such changing their light output. A slight change in the magnetic settings for the different beam setups might influence the gain of the PMTs. Additionally, the PMTs might undergo slight temperature variations or are damaged themselves. The relative gain-drift of the crystals is shown in figure 4.16 for the different settings. The drift is calculated according to

$$\text{Gain drift} = \frac{\text{Channel}_{\text{before}} - \text{Channel}_{\text{after}}}{\text{Channel}_{\text{before}}} \tag{4.5}$$

at an energy of 0.9 MeV and 1.8 MeV, corresponding to the Y-88-source. To check the impact of the drift the hypothesis drift of a 10 MeV energy deposition is checked, as this is the expected energy range of the γ-rays in forward direction. The crystals 6, 23, 44, 55, 69, 89, 113, and 121 are excluded from the γ-spectra because of their huge gain drift.
The resolution is obtained by the used sources. A linear function is adapted to the obtained data points. The linear function is used to extrapolate the resolution in the simulation. The resolution in means of FWHM for an energy of 1836 keV varies from about 80 keV to 130 keV. The worst resolution is obtained for the crystals in backward direction. The resolution for the crystals extrapolates to about 250 keV at 6 MeV. The impact on the isotope of interest can be estimated by using the first excited 2^+-state of Sn-132. It has an energy of 4 MeV, due to the Doppler boost the γ-energy in the laboratory frame is shifted to about 6 MeV.

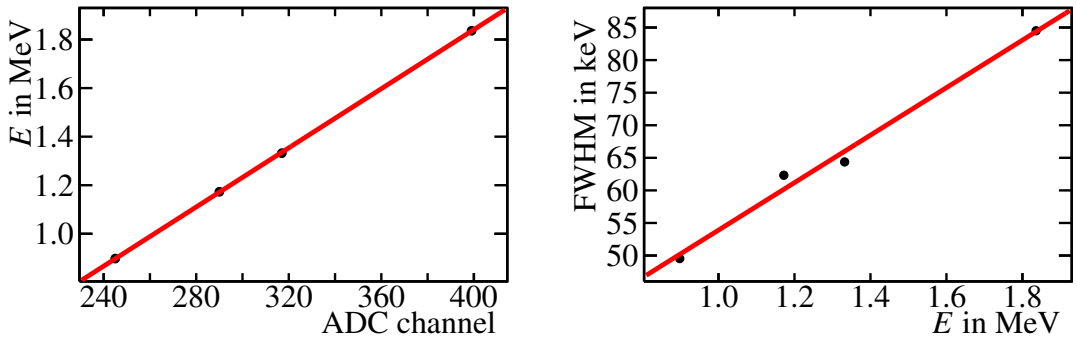

(a)

Figure 4.15.: Panel (a) shows the measured centroids for the transitions for the crystal 120. A linear fit is applied, to obtain the calibration parameters for the energy. Panel (b) shows the DALI2 resolution as a function of the energy for the crystal 120. The resolution was measured with Co-60 and Y-88. A linear fit to extrapolate the resolution is also shown with the parameters 0.036 for the slope and 17.4 keV for the offset.

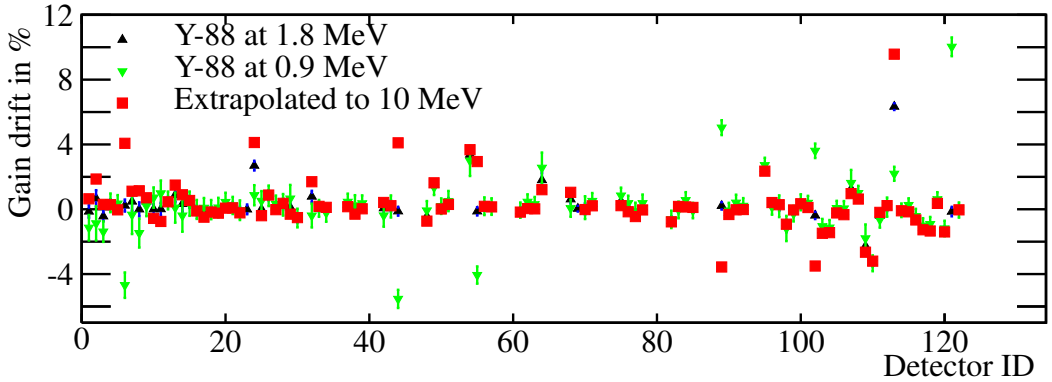

Figure 4.16.: Gain drift of DALI2 crystals after two days of beam-time. In red and green are the source-data, while in red the extrapolated drift is shown for an 10 MeV energy-deposition. Crystals with a gain drift of more than 4% are excluded. The crystals 23 and 69 have a shift out of plot-range.

LaBr

The LaBr crystals were energy calibrated just for the two different QTC-channels, namely the Mid- and Lowgain. The third channel, the Highgain, had a range below 3 MeV and was covered with the Midgain down to 1 MeV. The Midgain was calibrated using the γ-sources listed in table 4.4 and with the intrinsic radiation of the crystals. The Lowgain was calibrated afterwards, using the (linear) correlation to the Midgain and fitting a straight line within the overlapping range of the different gain channels. The Midgain covered an energy range from 0.5 MeV up to 15 MeV, while the Lowgain covered a range from 3 MeV to 70 MeV. The LaBr-array were rather stable during the experiment, but using the intrinsic radiation, the crystals had been monitored and recalibrated every ten runs.
For a calibration example, crystal 1 is used. The spectra shown in figure 4.17 is taken with the Y-88 source. The different structures, source peaks and intrinsic radiation, are marked in the spectra. The low energy peak (898 keV) of the source cannot be used, due to the intrinsic radiation. On the other hand the intrinsic and the higher lying γ-peak for the calibration can be used. The γ-peaks in the spectra were fitted with different functions for the background depending on the energy of the peak. In figure 4.18(a) a linear function is fitted to the centroids of the γ-transitions to obtain the slope and offset parameter for the energy calibration. The Lowgain is then calibrated using this correlation. A line is fitted in the overlapping proportional region.
Using the calibrated spectra the intrinsic radiation peaks have a well-defined energy-signal. This was then used for the energy monitoring and recalibration during the beam time. The change of the parameters shift only slightly, see figure 4.19(a) and is within a few percent, resulting in a change of about 150 keV in the region of 10 MeV. For more information see also section 3.4.2. A second quantity to influence the energy resolution is the intrinsic resolution of the detector. It is about 60 keV at 1.84 MeV. The evaluated resolutions for the crystal 1 are shown in figure 4.19, together with an adapted function according to equation 3.16.

4.4.2 Time Calibration

As the beam sets a time stamp at F8, which is 1198 mm before the target, the flight time from the plastic detector to the target is subtracted from the time stamp of each detector. Also the trigger time, corresponding to the time stamp of F7-plastic is subtracted. For the read-out with ADC-modules, the time is taken using a CFD, which gave an energy independent time signal. The read-out system was used for both LaBr and DALI2-crystals. The DALI2-crystals have been aligned in time. For this purpose the time signal is matched with a Landau function, see figure 4.20. A time resolution of about 3 ns (FWHM) for the DALI2-crystals was achieved. For the LaBr-array the correlation between the ADC and QTC branches was used to remove the energy dependence of

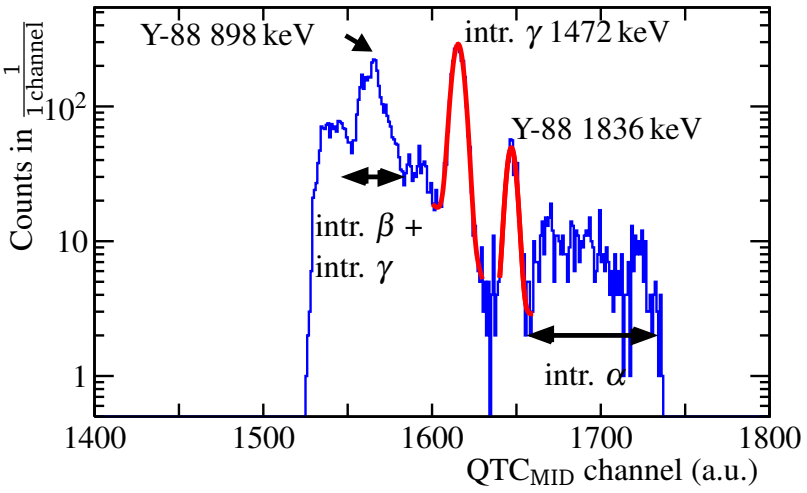

Figure 4.17.: Example of the LaBr calibration. The figure shows the raw spectra of LaBr-detector 1 obtained with a Y-88 source placed at target position. The spectra was fitted using two Gaussians for the photopeak and α-peak for the source peak. For the intrinsic γ-peak a Gaussian. A polynomial is used in both cases for the background. different peaks are marked, but for the calibration with this source only the higher and intrinsic radiation are used.

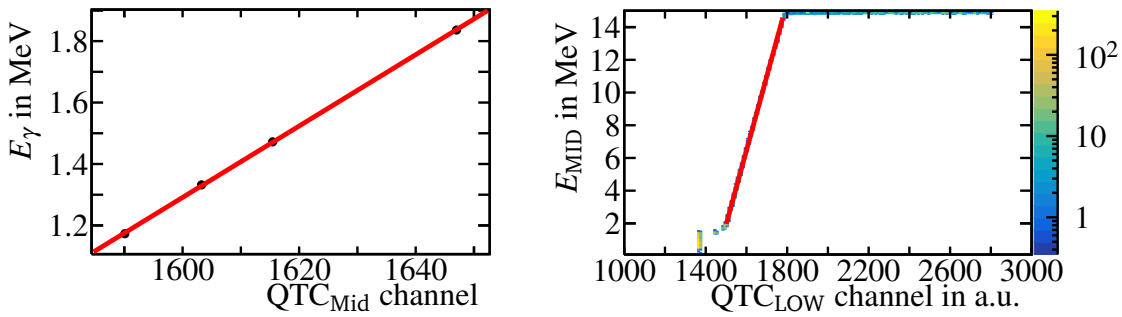

(a) (b)

Figure 4.18.: The left panel shows the linear fit to the obtained centroids of the source peaks. The right panel shows the calibration of the LaBr-Lowgain branch using the correlation to the already calibrated Midgain branch of the same crystal.

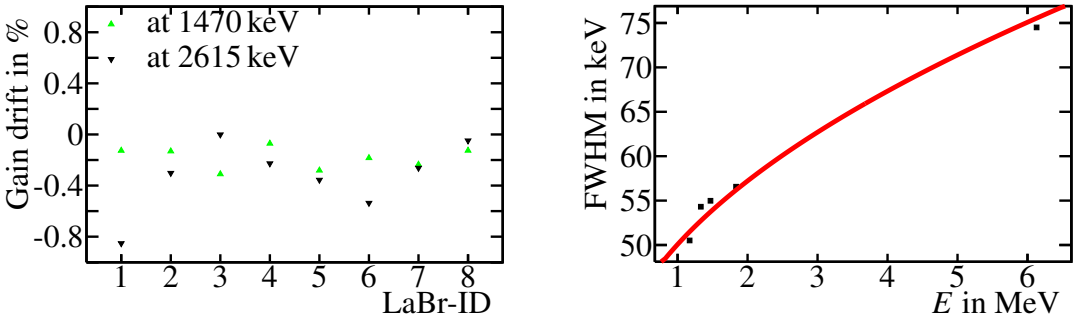

(a) (b)

Figure 4.19.: The left figure shows the change of the peak position of the intrinsic radiation. The γ-peak at 1.47 MeV and the α-peak at 2.6 MeV were used to do a recalibration of the LaBr during the experiment. All crystals had a small walk which is corrected. The right figure shows the resolution of the crystals determined with Co-60, Y-88, Cm-C sources and the γ transition at 1.5 MeV. These sources cover a range from 0.90 to 6.13 MeV.

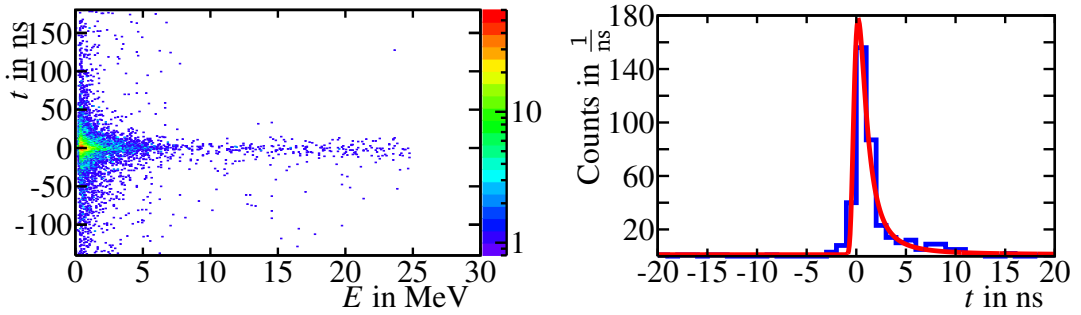

(a) (b)

Figure 4.20.: Time calibration of the DALI2 crystals. The flight-time and trigger-time are subtracted from the time-stamp. Panel (a) shows the typical peak structure of one crystal using in-beam data. Panel (b) shows the time-signal of beam-data for all crystals after alignment.

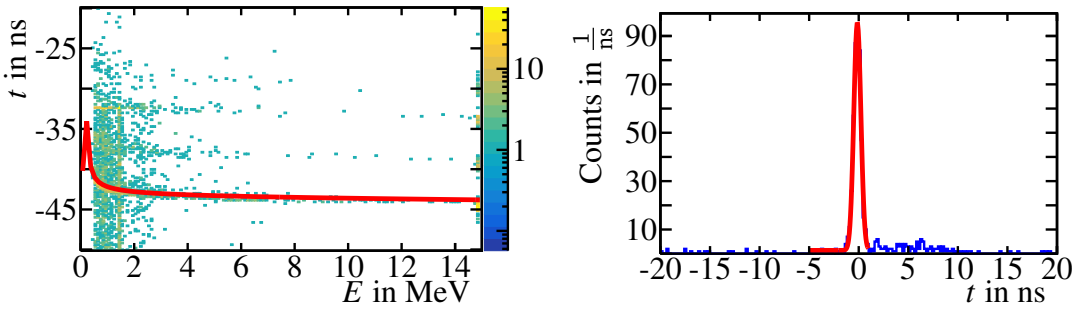

(a) (b)

Figure 4.21.: Time calibration of the LaBr crystals. The time of flight and the trigger time were subtracted from the time stamp. Panel (a) shows the typical energy dependence of the time stamp in the QTC-branch after selecting the events in the ADC-branch. Panel (b) shows the time spectra of one crystal in coincidence with the beam. The achieved time resolution is 700 ps.

the time signal in the QTC-branch. A time window was set for the ADC-branch, which uses a CFD, to study the time signal as a function of the energy signal. The resulting time spectra for the QTC branch is shown in figure 4.21. A clear energy dependence of the time signal is visible and was accounted for using the formula

$$t = a + bx + cx^2 + d\log|x-g| + e\log|x-g|^2 + f\log|x-g|^3. \tag{4.6}$$

The obtained parameters a to g are listed in table 4.5. Afterwards additional smaller corrections with a polynomial are added. A time resolution of 700 ps (FWHM) was achieved.

4.4.3 Addback Routine

The addback routine is performed to enhance the photopeak efficiency and to suppress the Compton-background, see also section 3.4.1. For these purposes, the experimental distance of the hits was analyzed, see figure 4.22. It can be seen, that a distance from 15 to 20 cm should be used, as there was a gap. The crystal with the highest deposited energy was chosen as the first impact of the γ-ray to apply the Doppler correction. In the spectra called addback, always the remaining single crystals are included.
The LaBr-crystals are not included in the routine, as they have a large volume and are shielded higher towards the sides. Due to the huge volume an addback routine is not expected to increase the efficiency significantly.
If in the following the spectra are called single, it shows the energy of (multiple) single crystals, while the sum spectra denotes to the sum of the deposited energy in the crystals, after Doppler correction, per event.

Table 4.5.: Parameters to correct the energy-dependence of the QTC time-signal for each LaBr-crystal. The equation 4.6 was used.
The time signal of the ADC-branch showed no dependency.

crystal	a in ns	b in $10^{-}3$ ns	c in 10^{-9} ns	d in ns	e in ns	f in ns	g
1	-308.7	0.166373	-3.02	-48.4155	71.1	-0.382	1506.79
2	-127.5	1.59423	-35.37	-135.244	205.5	-1.073	1425.76
3	-282.4	0.175805	-7.64	-58.9498	87.2	-0.4664	1437.45
4	-304.9	0.430991	-15.18	-44.4171	61.3	-0.315	1524.11
5	-276.9	1.43624	-38.60	-64.4813	92.0	-0.466	1421.49
6	-64.0	0.310712	-9.33	-152.694	223.5	-1.128	1357.95
7	-239.9	1.27036	-31.91	-78.5006	119.0	-0.639	1481.01
8	-352.0	0.949944	-26.95	-20.5423	20.2	-0.0816	1392.68

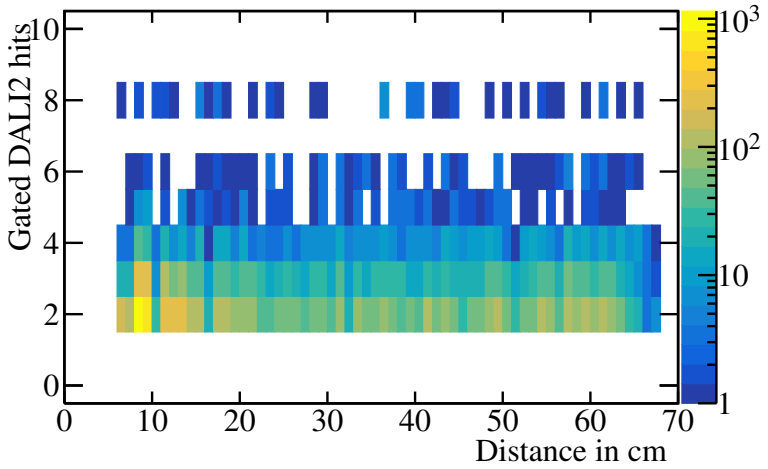

Figure 4.22.: Experimental distance of all gated DALI2 single hits versus their number per event. The plot was created using the reaction-channel Sn-132 → Sn-132. A gap is visible at a distance of about 15 cm and 2 to 3 gated crystals. The distance is used later on, to limit the addback routine.

4.4.4 Doppler Correction

To obtain the energy of the γs in the CM system the Doppler correction was applied, see equation 3.15. Based on the outgoing measured TOF, the velocity β during de-excitation is estimated. Therefore, the material of in-beam detectors and target is taken into account. As interaction and de-excitation point of the ion the center of the target is assumed. The velocity was calculated based on the average energy-loss using the TOF. Using a linear function with the parameters of 0.682 for the slope and 0.190 for the offset, the velocity of the ions at the emitting point is estimated. As the emitting point the center of the target is taken, as only a very short lifetime is expected.
To obtain the angle of the emitted photon the outgoing pointing vector of the ion and the interaction point are needed, see figure 4.23.
The interaction point is calculated by prolongating the direction obtained from the PPACs in front of the target to the target center in z-direction. Thus, the x- and y-position is given. The outgoing vector is evaluated with the help of the PPAC after the target. The impinging point through the PPAC and the target position contain the information of the outgoing vector. The needed vectors, in order to set the angle θ, are calculated according to the following equations:

$$\begin{aligned} \vec{x}_{\text{int}} &= \vec{x}_{\text{PPAC}}^{\text{before}} + \vec{v}_{\text{in}} \cdot d_{\text{in}} \\ \vec{v}_{\gamma} &= \vec{x}_{\text{det}} - \vec{x}_{\text{int}} \\ \vec{v}_{\text{ion}} &= \vec{x}_{\text{PPAC}}^{\text{after}} - \vec{x}_{\text{int}} \cdot d_{\text{out}} \end{aligned} \tag{4.7}$$

with the distance $d_{\text{in/out}}$ from target-center to the PPACs before and after the target, $\vec{x}_{\text{det}}$ the detector position, and $\vec{x}_{\text{int}}$ the interaction point. In the case that the PPAC after the target did not fire, the incoming vector is used as the outgoing vector. The angle θ is then given by

$$\cos(\theta) = \frac{\vec{v}_{\gamma} \cdot \vec{v}_{\text{ion}}}{|\vec{v}_{\gamma}||\vec{v}_{\text{ion}}|}. \tag{4.8}$$

The target position in x- and y-direction can be determined with an uncertainty of about 2.3 mm, increasing the uncertainty of the emitting-angle θ, which is dominated by the opening angle of the crystals and the z-resolution due to the target thickness of about 26 mm. Having the Doppler correction performed, offsets in the x-, y-, and z-directions are estimated. For the first two directions the LaBr-array is used and changed until all the crystals were aligned for the first 2^+-state in Sn-132 with an energy of 4.04 MeV, see figure 4.24. The z-offset was done using the different layers of DALI2 and the LaBr. The offset was adjusted until all Doppler-corrected layers had the same transition energy and best resolution. The results are listed in table 4.6 and are in the order of a few mm.

Table 4.6.: The in-beam detector-offset at target position compared to the position obtained by aligning the Doppler-corrected energy of the crystals.

coordinate	offset in mm
x	3.5
y	5.3
z	-2.0

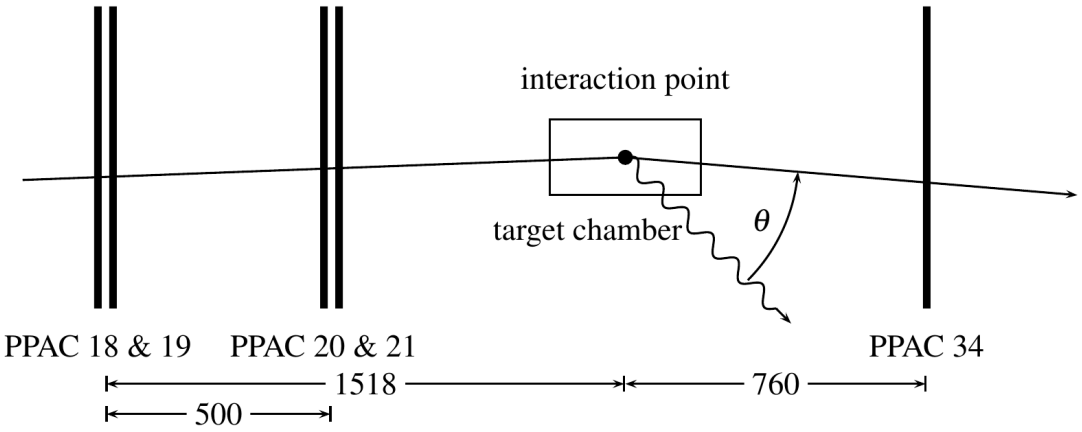

Figure 4.23.: Reconstruction of the emitting angle θ of the γ. The interaction point is reconstructed using the first two PPAC pairs at F8, while for the outgoing vector a direct line from the interaction point to the PPAC after the target is assumed. The interaction point is set to the center of the target.

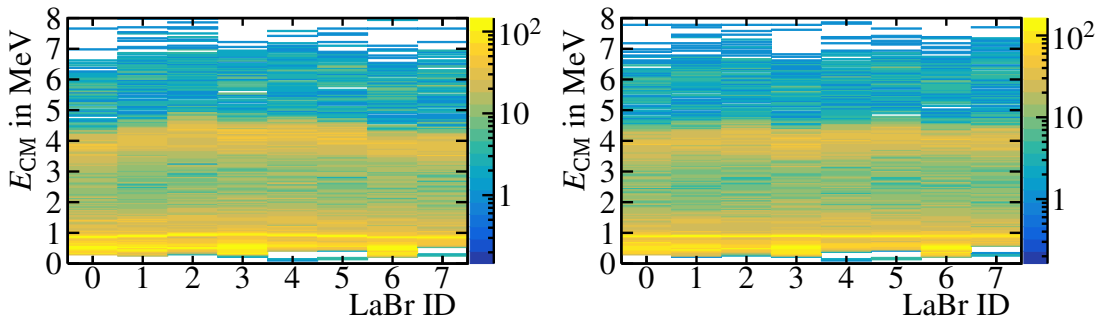

Figure 4.24.: The in-beam detector offset is estimated at target position. Using the LaBr-crystals the 2^+ transition should appear for all crystals at the same energy. Comparing the crystals 1 to 4 in figure (a) with the other four crystals the x-offset can be adjusted. The same can be done comparing the crystals 3-6 with the other four. Using all photodetectors the same procedure can be applied to obtain the z-offset. This results in a crystal independent γ-ray energy, see figure (b).

4.4.5 Efficiency

The efficiency of the array was estimated using an Y-88 source at target position, see also section 4.4.1. The calibration run took about 1.3 h. The two photons stemming in coincidence from the source with energies of 1836 keV and 898 keV are used. Although, the lower energy peak is superimposed with the internal radiation of the LaBr and usually cannot be used as a gate, the DALI2 array offers the opportunity to do so. Setting a gate on this low energy peak with the DALI2 array and observing within a small time window the higher lying peak, will give the efficiency for both arrays at 1.8 MeV in return. The intensities of the transitions are 93.7% (898 keV) and 99.2% (1836 keV). The states have lifetimes of less than a 1 ps [nnd]. However it holds true that if a γ with an energy of 898 keV is detected, then there will be a second one with 1836 keV.
The procedure is as follows: The observation of an energy in a 2σ-window around the 898 keV opens a time window of 20 ns. A cut on the number of observed photons reduces the background originating from random coincidences. The now observed energies at the second transition should be almost background free. The number of gates and photons in coincidence is corrected by estimating the background in this region with a fit function. In addition, gates above and below the energy of the γ are used to correct for random coincidences. The full-energy peak-efficiency is estimated to be 0.89(5)% for the LaBr- and 5.71(12)% for the DALI2-crystals. For the fits see fig-

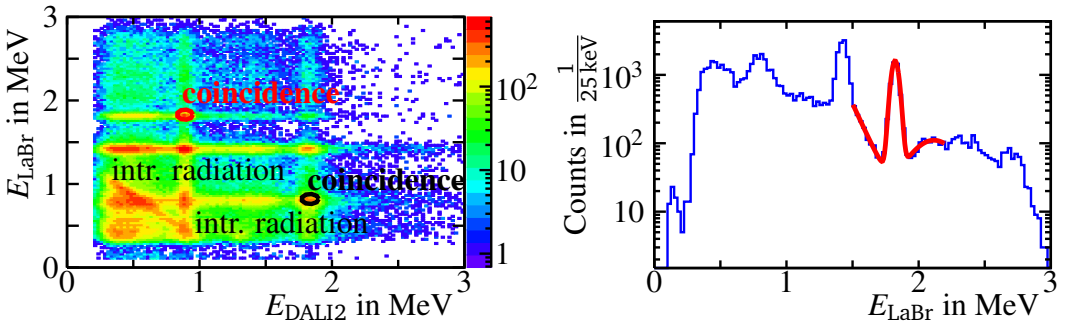

(a) (b)

Figure 4.25.: Using an Y-88 source the efficiency was evaluated. Panel (a) shows the coincidence matrix of the source data. Panel (b) the γ-spectra taken with LaBr in coincidence with a 898 keV transition. In the left panel the red marked area is used for coincidences, while the other marked area is not used. In the left panel the used fit is shown in red.

ure 4.25. The effect of the angular distribution was taken into account, which is about 3%. Using the LaBr-array this results in an detection efficiency for de-exciting ions with $\beta = 0.55$ of 9.0% and 3.8% for γ-energies of 4 and 7.4 MeV, respectively. The energies correspond to the first 2^+-state in Sn-132 and the second energy is just above the particle threshold for the same isotope.

4.5 Simulation

The simulation is used to obtain the detector response to emitted γ-rays. In a first step, the EventGenerator simulates the beam conditions and sets the reaction and de-excitation point. In addition, angular broadening and energy loss are included. The input parameters were adjusted to match the experimental beam profile and velocity. The profile of the beam was simulated using Gaussian distributions of the quantities β, x-, y-position and the angular distributions, see figure 4.26 as an example. The target chamber and holding structures are set according to their dimensions (see section 3.5) and density. The filling gas helium in the target chamber is also set to the values measured during the experiment. As a check the velocity distribution after the target is calculated. The difference between the experimental and simulated energy loss due to the target are less than the experimental uncertainty. In the second step, called the EventBuilder, the crystals are placed including their mounting-construction. The beam-pipe in the simulation included the lead and tin shielding together with the target housing. For the reconstruction the resolutions of the plastic detectors and PPACs are passed to the simulation. The x-, y-position, and β are folded with the detector

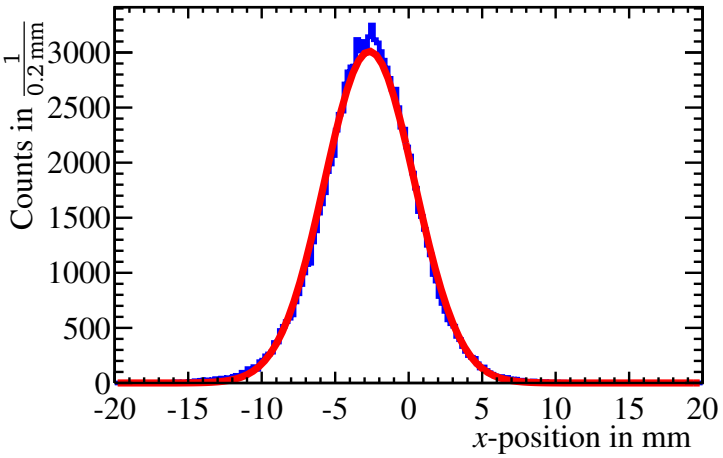

Figure 4.26.: The beam profile is shown here as a function of the x-position together with a Gaussian fit to it. The fit parameters width σ and centroid μ of the distribution are used for the simulation.

response, which is Gaussian and the width corresponding to the resolution. The resolution of the γ-detectors is transfered to the simulation by functions of the form given in the sections 3.4.2 and 3.4.1. In the last step, the so called RikenReconstructorDLB reconstructs the events in the same manner as for the experimental data.
All the parameters and structures in the simulation are adapted until the efficiency for γ-detection at 1.8 MeV can be reproduced. Figure 4.27 shows the comparison between Y-88 source data and the simulation for the DALI2 array. They are in good agreement. In order to compare the data taken with beam to the simulation, background has to be included. The atomic background can be simulated, too. The difference between the spectra with and without this background source was checked and found to be negligible, see figure 4.28. To save computing time, this option is switched off. Other background channels are estimated with the help of experimental data. Such are the neutron-background, stemming from contamination in the particle identification, and non-coincident background such as internal radiation, see next section.

4.6 Estimating the Background

To adapt the simulation to the dataset, it is quite important to estimate the shape and intensity of the background. Therefore, the background not in coincidence with the beam, called offbeam, is used as one source, *e.g.*, to estimate the intrinsic radiation of the LaBr-crystals. This background is taken in a time window well before the incident beam. The beam itself can contribute with a resonant contamination. This contamination is estimated by a time window shortly after the beam. In this resonant background

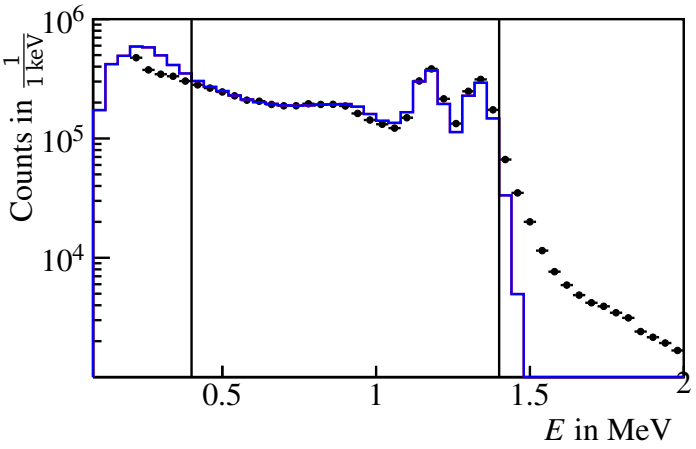

Figure 4.27.: The simulation of the source Y-88 is fitted to the source measurement of Y-88 with the DALI2 arrays. The source is placed at target position within the target chamber. The black lines show the limits of the fit. The upper one is due to the simulation limit, while the lower limit is due to hardware thresholds.

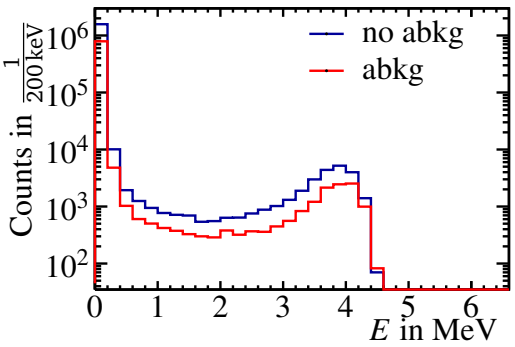

Figure 4.28.: The influence of the atomic background to the spectra is shown. In red the spectrum with simulated atomic background is shown, while in blue the spectrum is shown without background.

the offbeam background is already included. This background stems mainly from slow neutrons and has a huge tail. The neutrons and intrinsic radiation are subtracted. In the case of the LaBr-array an contribution below 4 MeV remains, while the entries located at higher energies are in agreement with zero. Moreover, the background might be due to wrongly identified particles. As BigRIPS has the much better identification, only the misidentified isotopes in ZDS are taken into account. In the case of tin, such are the one and three neutron-removal reactions, and the one proton and one/two neutron or one deuteron/triton removal channels. These channels lie closest to the magnetic rigidity and atomic number of Sn-132 and Sn-128. For the 3n-removal reaction this is only true for the 49+ charge state. The charge-state contribution can be directly estimated using the experimental data and identifying the 49+ charge state of Sn-132. The number of Sn-132^{49+}-states identified is 75000 while the total accepted number of events is 125000. From those events some may be a contamination due to the other background channels. Their contribution is small and contributes also to the 3n-removal channel. Therefore the percentage of the 49+ charge-state is about

$$p(\mathrm{cs}) = \frac{N_{\mathrm{cs}}}{N_{\mathrm{Sn}-132^{50+}}} \overset{cs=49+}{=} 6.03\%, \tag{4.9}$$

with cs denoting to charge state, and N the number of isotopes in the 2σ region around AOQ=2.64 and $Z = 50$. For the other isotope the value for the charge-state contamination is 7.54(3)%. The higher value caused by a lower velocity. Note, that with the charge state contribution is of the same size as the charge-state loss. Contributions of other charge states are neglected here, as first of all the stripping probability is higher, therefore, they are rejected by the δ-selection criteria, and second the contribution is be small compared to the 49+ charge state.
For later the coefficient of the 3n-removal channel $p_{3\mathrm{n}}$ can be estimated. This leads to an expected coefficient in the order of $a \cdot p(\mathrm{cs}) = 5\%$, with a the overlapping integrated area of a Gaussian distribution with the resolution of ZDS as width and the centroids of the states for the 3n contamination (for both isotopes). This value might actually be higher, as the γ-trigger rate for removal reactions will be higher. Furthermore, will the 1n channel also contribute to the neutron channel, a fact that could be absorbed in the 3n channel. This kind of background has a broad distribution and might have additional photon-peaks, see figure 4.30. For DALI2 the background contribution can be different from this, as the main background stemming from particles should be distributed in the most forward detectors. Charge-changing reactions can also contribute to the spectra. For this the 1n1p and 2n1p-removal reaction-channels are checked, see figure 4.30(b). The contribution should be close to zero, assuming a Gaussian distribution. The region is more than 0.4 and 2 σ away in AOQ and Z, respectively. The particle contamination was assumed to be purely coming from the 3n-channel.
The contamination due to the target chamber was checked with an empty-target run,

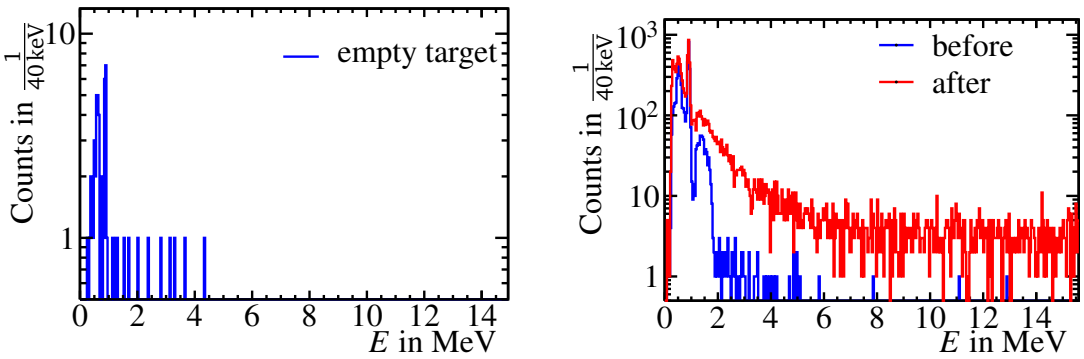

(a) empty (b) offbeam

Figure 4.29.: Experimental background response of the LaBr-array using the reaction Sn-132 to Sn-132. Panel (a) shows the background events taken with an empty-target run. Panel (b) shows the response of the LaBr-crystals offbeam, before(red) and shortly after (blue) the beam passes the target.

see figure 4.29(a). The contribution was found to be negligible, as only a few counts including the internal radiation were registered. For more details of the particle contamination see the next chapter.

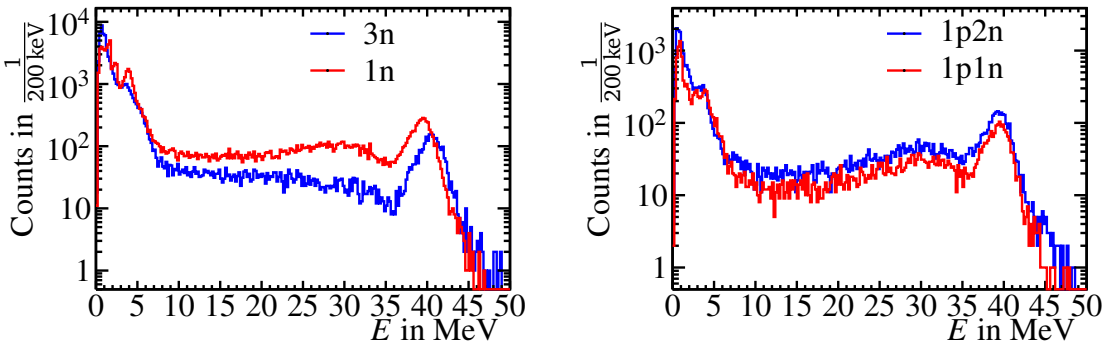

(a) 1n,3n

(b) 1n1p,2n1p

Figure 4.30.: Experimental response of the LaBr-crystals gating on the background channels, 3n, 1n removal in Sn-132. The contribution at energies higher than 7 MeV is almost flat, while peaks are visible at energies lower than 6 MeV. Those peaks correspond to known transitions in the isotope Sn-131 at energies around 4 MeV and 1.6 MeV.

5 Conclusion

5.1 Determination of the Cross Sections

To estimate the cross sections to excite the two different isotopes to the excited states, following assumptions have been made:

- the probe, α, excites predominantly *E0*, *E1*, and *E2* transitions at small angles,
- the decay time, if not known, is short, as is typical for those transitions.

The expected particle background, see section 4.6, is fitted to match the high-energy tail of the spectra, well above the neutron-separation threshold S_n. The offbeam background is subtracted, too. Whereas the atomic background is not included. Also the background stemming from the target cell is neglected, described before.
The procedure for the estimation of the cross sections are for both isotopes the same, nevertheless the contribution of the background differ. In the next two section the results for the two isotopes are presented. In section 5.2 the systematic uncertainty is evaluated and finally compared to other experiments in the section 5.3 to other experiments and the prediction of the theoretical framework presented in section 2.2. In the following the concept of determining the cross section is summarized.

The cross section σ is defined as the interaction probability p divided by the number of scattering centers per area unit ρ_n.

$$\sigma = \frac{p}{\rho_n} \tag{5.1}$$

The probability is obtained by comparing the number of particles hitting the target and the number of particles populating a certain state,

$$p_{\text{state}} = \frac{\text{number of particles populating certain state}}{\text{number of particles hitting the target}}. \tag{5.2}$$

The particles hitting the target is estimated using an incoming beam trigger, *e.g.*, the downscaled F7 trigger, see section 3.6. The number of particles populating the state of interest is estimated from simulations. After adapting the simulation to realistic conditions of the beam profile and detector setup, the response of the detectors is fitted to the experimental background-subtracted spectra. The fit value is directly proportional to the number of ions populating the state of interest. For each observed peak one state is simulated and the transition energies with the lowest χ^2 are chosen. The state may

Table 5.1.: Important parameters to calculate the cross section.

	Sn-132	Sn-128
target thickness in $\frac{\text{mg}}{\text{cm}^2}$	334.6(21) for both	
transmission coefficient in %	97.65(21) for both	
selection criteria in %	90.0(1) for both	
reconstruction efficiency in %	99.8(1)	99.7(1)
charge-state loss in %	6.03(2)	7.54(3)
number of events	758M	323M

cascade, which can be included in the simulations. The previous variables are used to determine the reaction probability, the missing number of scattering centers ρ_n is calculated using the determined target thickness, see section 4.3.
Other effects may alter the obtained cross section. Such effects are reconstruction efficiencies of detectors, transmission efficiency and acceptance of devices afterwards, *e.g.* ZDS, loss of "good" events due to a change of the charge-state in or after the target, and the selection criteria. The impact of those effects have to be evaluated and the cross section adapted accordingly. In table 5.1 those important parameters to calculate the cross section are summarized.
Before adapting the simulation to the experimental data, the evaluation of the background is mandatory. Therefore, different experimental background channels, namely offbeam and 3n-removal reactions, are scaled to the data, it is explained later. In more detail, the offbeam data is scaled to match the same total time as the selection of the γ-acceptance window, while the 3n-removal channel is scaled to match the spectra at energies above 10 MeV. Background introduced, for example, due to the target chamber was estimated using the empty-target runs (about 2.5 h) show no significant amount of detected γ-rays in particular above 3 MeV, see section 4.6. The amount of atomic background was simulated and found to be negligible, see section 4.5.
The procedure for the estimation of the cross sections are for both isotopes the same, nevertheless the contribution of the background differ. Note, that the (known) level density is for Sn-128 much higher than for the closed shell nuclei Sn-132. As such the single states are not resolved in the first mentioned isotope.

5.1.1 Sn-132

In a first step the background stemming from random coincidences and knock-out reactions was subtracted. Therefore, following assumptions are made. The particle background is mainly due to the 3n-removal reaction, as this channel with its charge state 49^+ is the closest in means of AOQ- and Z-value. In addition, this experimental background-channel reproduces with the best goodness of the fit the data at energies above 12 MeV. The 3n-removal channel dominates the spectra above 10 MeV. After

subtracting the 3n background and the offbeam-channel and fitting the spectra, LaBr single and DALI2 with addback-routine, simultaneously and each individually a huge discrepancy between the fit values of the arrays was at hand. The LaBr-single spectra showed significant remaining strength below 3 MeV all and, at the same time, an overestimation at 4 MeV. The remaining strength can be explained by assuming a resonant background and an exponential function modelling the rest of the strength below 2 MeV. For the resonant background a time-window from 1.3 ns to 2.7 ns after the beam. The channel is apparently contaminated with neutron-channel and the intrinsic radiation, both are subtracted to avoid a double subtraction. In figure 5.1 the background subtraction is shown and in figure 5.3 the subtracted spectra is displayed, in both cases for LaBr- and DALI2-array. With this procedure the overestimation in the peak at 4 MeV vanished, too.
The background-subtracted spectra is fitted with simulated transitions. For the known excited states, see figure 5.2 for a level scheme, all known information are passed to the simulation – their decay schemes, lifetimes, and energies. The unknown states are assumed to have a short life time, in the order of 1 ps. The spectra are all fitted simultaneously in a range of 2 MeV to 8 MeV. Transitions at 4 MeV (2^+-state), at 6.25 MeV, and at 7.1 MeV were observed, see table 5.2.
The sum spectrum, summing up the observed γ-ray energies in DALI2 and LaBr arrays event-by-event, provides sensitivity to cascades. As a 10 MeV state is visible in Sn-132 excitation with an isovector probe, see section 2.1 and in reference [KPA+07], it would be intriguing to observe such a state. A more detail check was done for a coincidence between the 6.25 MeV state and the 2^+-state. For possible observed coincidences, the γ-γ-matrix is shown in figure 5.4. If all transitions of the 6.25 MeV peak are cascading via th 2^+-state, this would lead to a sum-peak height of about the same size as the background, see figure 5.5. Using a coincidence gate for the high-energy peak about 20 and 25 events should be observed with γs depositing energy between 3 MeV and 4 MeV, according to simulations. In the simulations considering an angular correlation for transitions between 1^--2^+-0^+ states and no angular correlation of the γs are considered. Fitting the simulated sum spectra to the experimental data up to 12 MeV leads to an upper limit for the cross section of 4.4(4) mb for a state decaying over a cascade of γs with energies of 6.25 MeV and 4.04 MeV, reducing the 2^+ cross section by the same size. However, the simulated sum-spectra of the crystals overestimates systematically the background subtracted spectra at energies above 8 MeV with one standard deviation for each data point. The coincidence cannot be ruled out, but seems to be unlikely. Therefore the state with 6.25 MeV is of isoscalar nature.
Above the neutron-separation threshold $S_n = 7.3$ MeV no transition is observed. However, in the single spectra of both arrays an underestimation of the strength is visible. As the branching ratio between particle emission and γ transition for decays above the threshold is unknown, it is difficult to estimate the sensitivity, an upper limit is 1.5 mb for a pure direct γ-decay with no lifetime and a confidence-level of 5 σ, including the

Table 5.2.: Cross section of the transitions in Sn-132.

Known states			
Multipolarity	2^+	3^-	
Energy in MeV	4.04	4.35	
Cross section in mb	$22.4(16)^{+1}_{-0.4}$	$8.11(68)^{+0.5}_{-0.1}$	
New states			
Multipolarity			
Energy in MeV	6.25(10)	7.10(15)	10
Cross section in mb	$4.03(30)^{+0.21}_{-0.015}$	$0.258(16)^{+0.027}_{-0.011}$	< 1.5

systematic uncertainty.
One question to describe the spectra remains open: What is the origin of the enhancement in the LaBr-spectra below 4 MeV? Although, the background is described, this kind of background estimation is not needed for the other isotope. An exponential fit, can be related to atomic background, but this source was beforehand excluded by simulations and is not present for the other isotope, with similar energy and same element number. Unresolved strength via cascade could also provide strength as in the isotope several excitation states exist, but then they should be observed in both arrays. The argument that in Sn-128 the background is not used to describe the data, leaves open the point, that the DALI2-array is excluded in the procedure of fitting the spectra, see next section. But the discrepancy between the two arrays was one of the point searching for an additional background source.

5.1.2 Sn-128

The background is subtracted with the same techniques as described in the previous section. The background is estimated using the 3n-removal channel and scaling the data to the spectra above an energy of 12 MeV. The background subtraction is shown in figure 5.6 for both detector-arrays. The 3n-removal channel describes the spectra slightly better as the 1n-removal channel or the charge-changing channels. Again a mixture of the channels was not favored in the fit procedure. The random coincidences are subtracted as before. The resonant background was investigated in the same manner as in the previous section. The channel was found to have no or just little strength in contrast to Sn-132.
The DALI2 spectra can be subtracted in such a way, that almost no strength is left, not even the first excited state at 1.17 MeV is visible. The fit of the background favors a particle background, which seems to be unreasonable high with values above the actual number of observed 3n-removal events. The detector array is therefore excluded to determine the cross section, as any obtained result is in agreement with zero within

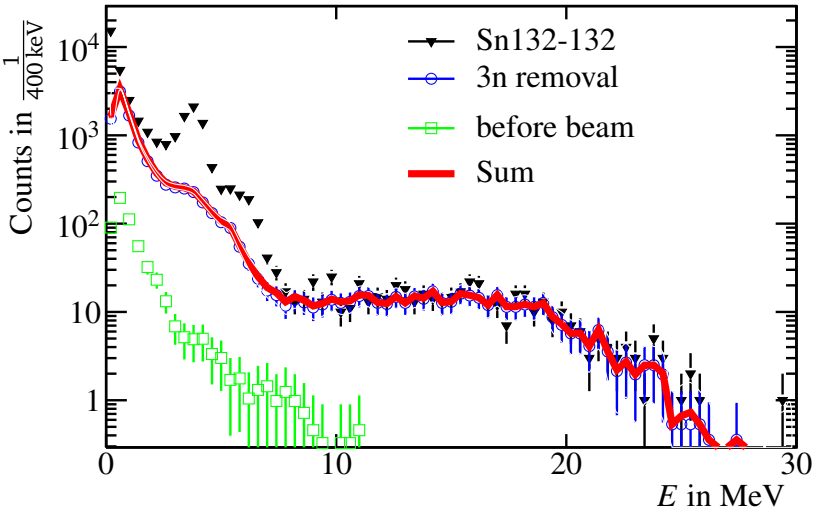

(a) DALI2 with add-back

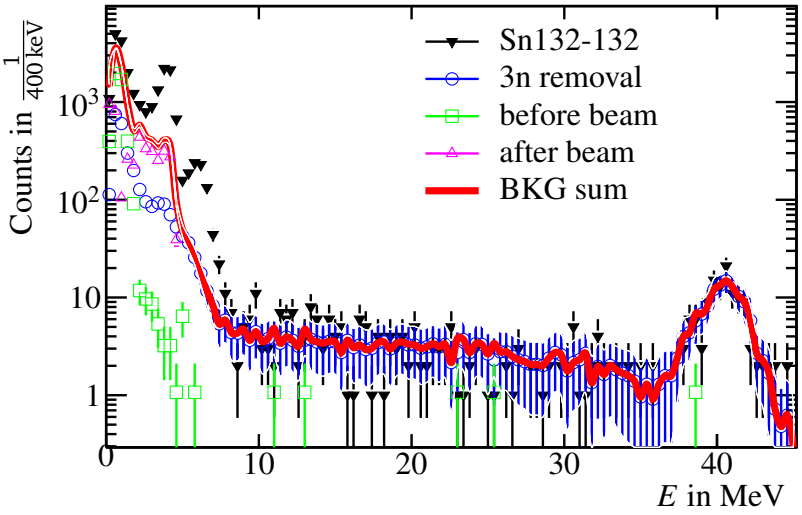

(b) LaBr array

Figure 5.1.: The background is subtracted by fitting the experimental 3n-removal channel to the spectra above 12 MeV, as there are no γ-rays expected and scaling the offbeam-channels to the same amount time as the on-beam data. The left and right figures show for the two different γ-detector type the fitted background. For the LaBr-array, panel (b) additional background sources are included, see text. The enhancement at about 40 MeV is the Doppler shifted overflow.

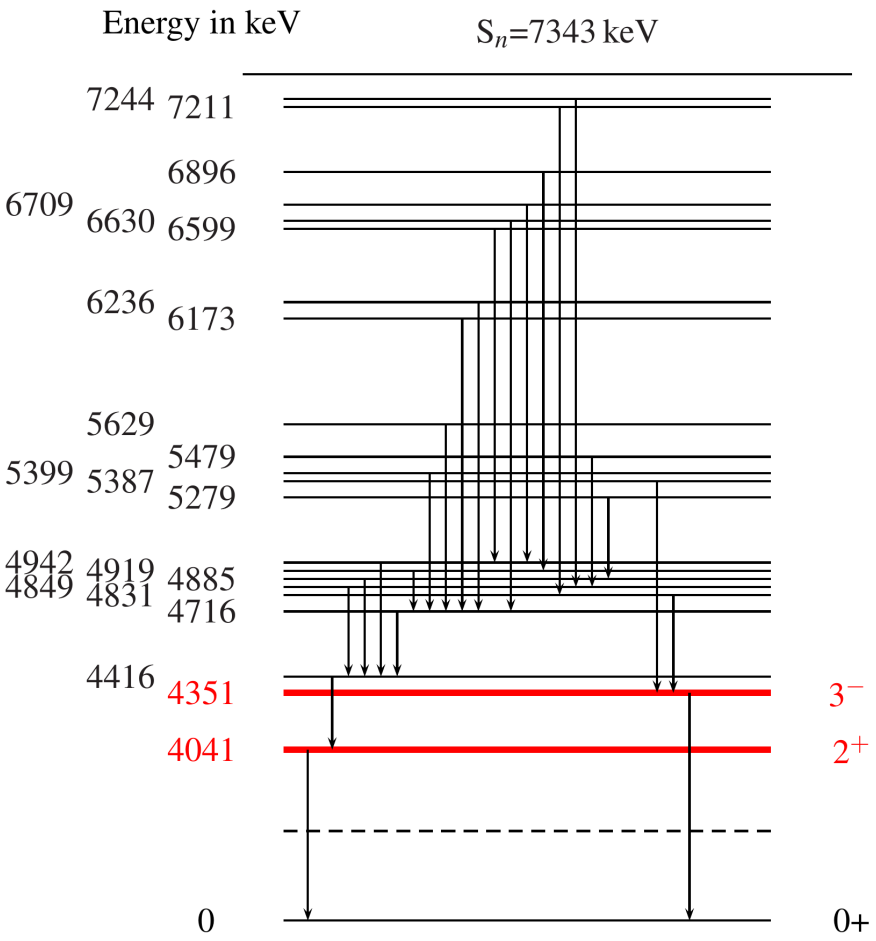

Figure 5.2.: Level scheme of Sn-132 with all levels and the main transitions and known lifetimes. If the low-lying dipole state cascades, it should be in coincidence with the 2+-state. As such the state should be observable in coincidence. Transitions and state used as fit parameters are presented with thick red lines. J^π are shown only for the states included in the simulation. The 8^+-state having an energy of 4849 keV is an isomer with a halflife time $t_{1/2} = 2.03\,\mu$s. The data are taken from [nnd].

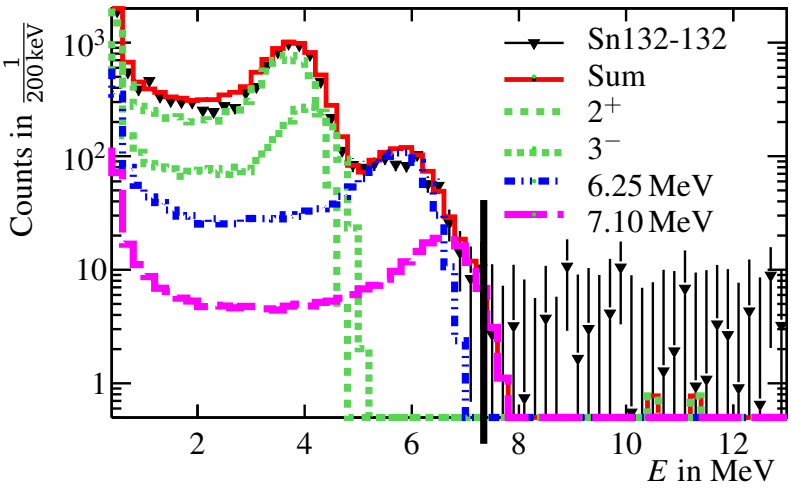

(a) DALI2 with add-back

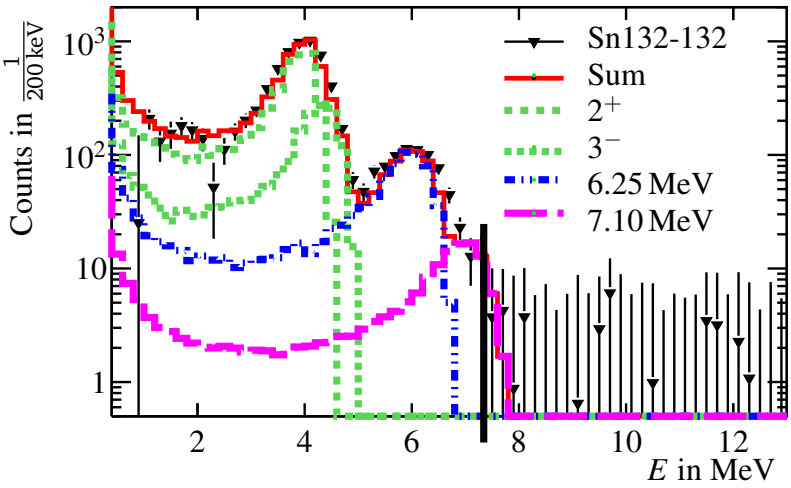

(b) LaBr array

Figure 5.3.: Both figures show the simultaneous fit of the simulated response to the experimental data. Figure (a) shows the DALI2 response with the addback-routine, while figure (b) shows the single spectra of LaBr. The fit to the sum of both is not shown, see figure 5.5. The thick black line indicates the neutron-separation threshold, above the threshold no strength is visible.

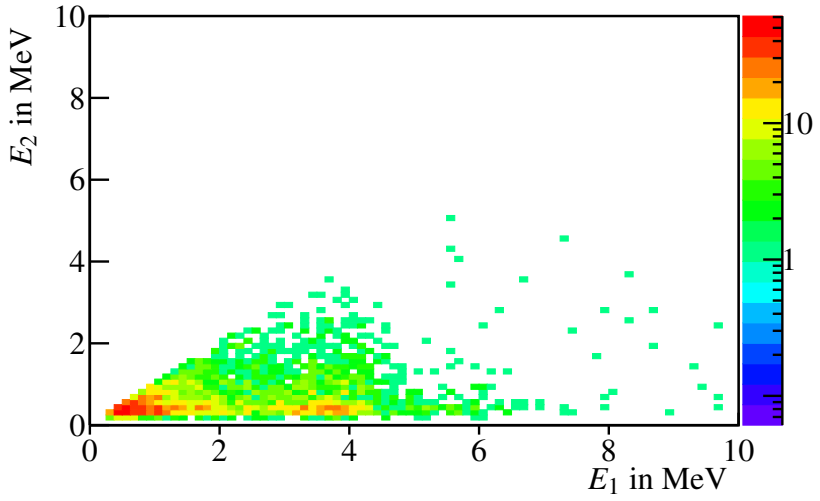

Figure 5.4.: Shown here is the γ-γ-matrix for Sn-132 obtained in the experiment. No coincidences are visible.

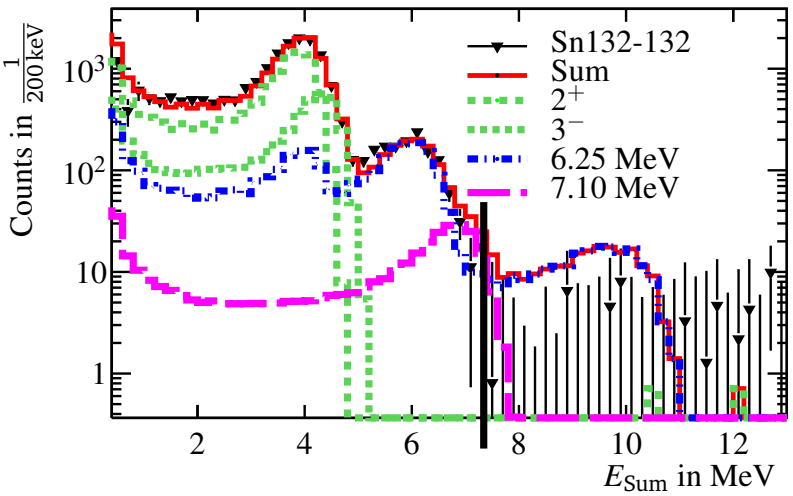

Figure 5.5.: The figure shows the sum spectra together with a simultaneous fit of a hypothesis cascade with 6.25 MeV and 4.04 MeV (2^+-state) to the experimental beam data. The black line indicates the neutron-separation threshold. A systematic overestimation of the data above an energy of 8 MeV, within 1.5 σ per bin, is visible.

Table 5.3.: Cross section of the transitions in Sn-128. The first rows show the cross section for known 2^+-states.

Known states			
Energy in MeV	1.17	2.10	3.52
Cross section in mb	$1.1(2)^{+0.1}_{-0.1}$	$0.76(10)^{+0.07}_{-0.01}$	$0.27(4)^{+0.27}_{-0.03}$
Energy in MeV	4.04	4.08	4.30
Cross section in mb	$0.397(50)^{+0.126}_{-0.004}$	$0.308(39)^{+0.39}_{-0.03}$	$0.357(45)^{+0.004}_{-0.5}$
New states			
Energy in MeV	5.45(15)	6.35(15)	10
Cross section in mb	$0.112(29)^{+0.082}_{-0.001}$	$0.079(29)^{+0.057}_{-0.001}$	< 0.2

three or less sigma using only this array. Furthermore, the systematic uncertainty due to the performed background subtraction is high. The following covers only the analysis performed for the LaBr array.

The background-subtracted spectra does not show a clear peak structure as for Sn-132, except for the transition of the first excited 2^+-state to the ground state, see figure 5.8 and figure 5.7 shows reduced level scheme. The first excited state in Sn-128 is in the region of the Doppler-shifted intrinsic radiation. The intrinsic γ-radiation at 1.47 MeV is due to the Doppler-effect reduced in energy to about 1.1 MeV, almost overlapping with the energy signal of 1.17 MeV.

For the remaining strength in the spectra of Sn-128 six other known 2^+-states with their decay-channels are fitted. For the remaining enhancement two gamma peaks are chosen with energies of 6.50(15) and 5.45(15) MeV to explain the strength. Those transition energies are selected with two criteria, minimize the χ^2-value and minimize the number of transitions.

In analogy to the isotope Sn-132, the coincidence-matrix including and excluding the DALI2 array was investigated. No coincidence between transitions above 2.5 MeV were observed, see figure 5.9, even though the known fitted 2^+-states cascade, see figure 5.7. But this might be due to the many competing states and thus the cascade splits into several branches. Thus, the statistic per excited cascading state is small and the remaining second transition might then be hidden within the other transition energies varying from 1 to 4 MeV. For the two new states the cross section was determined to be 1.72(42) and 1.21(45) mb for 5.45 and 6.35 MeV respectively. The evaluated cross section have a significance of 4.0 and 3.0, respectively. The cross sections with their uncertainties are summarized in table 5.3.

For the strength abobe the neutron-separation threshold at 10 MeV for again the pure γ-decay can be given with 0.2 mb with a 5 *sigma* confidence-level.

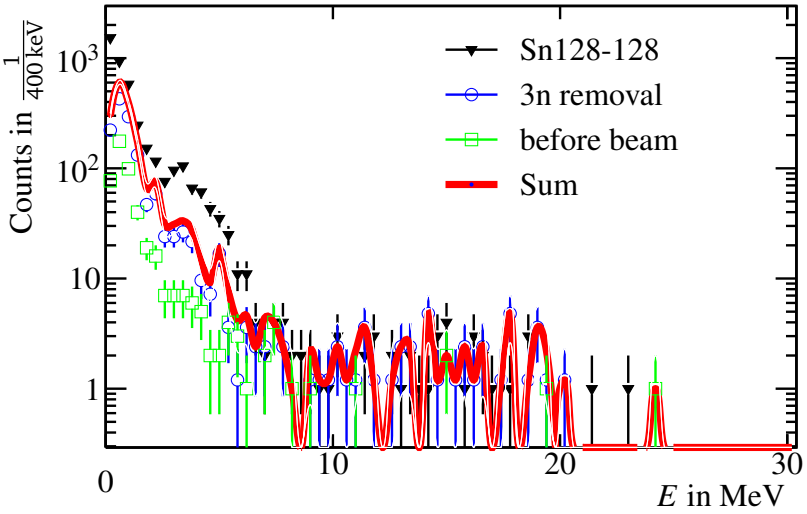

(a)

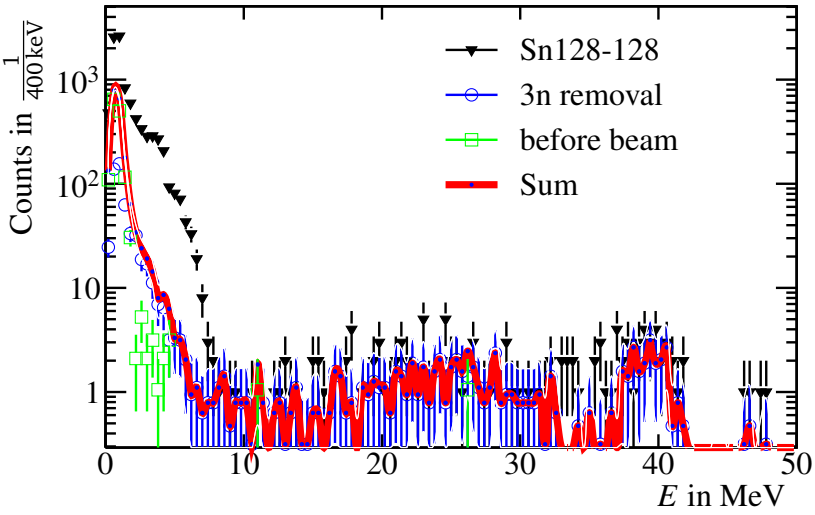

(b)

Figure 5.6.: Background subtraction for the Sn-128 isotope. Figure (a) shows the subtraction for the DALI2-array, while figure (b) shows the same for the LaBr-crystals.

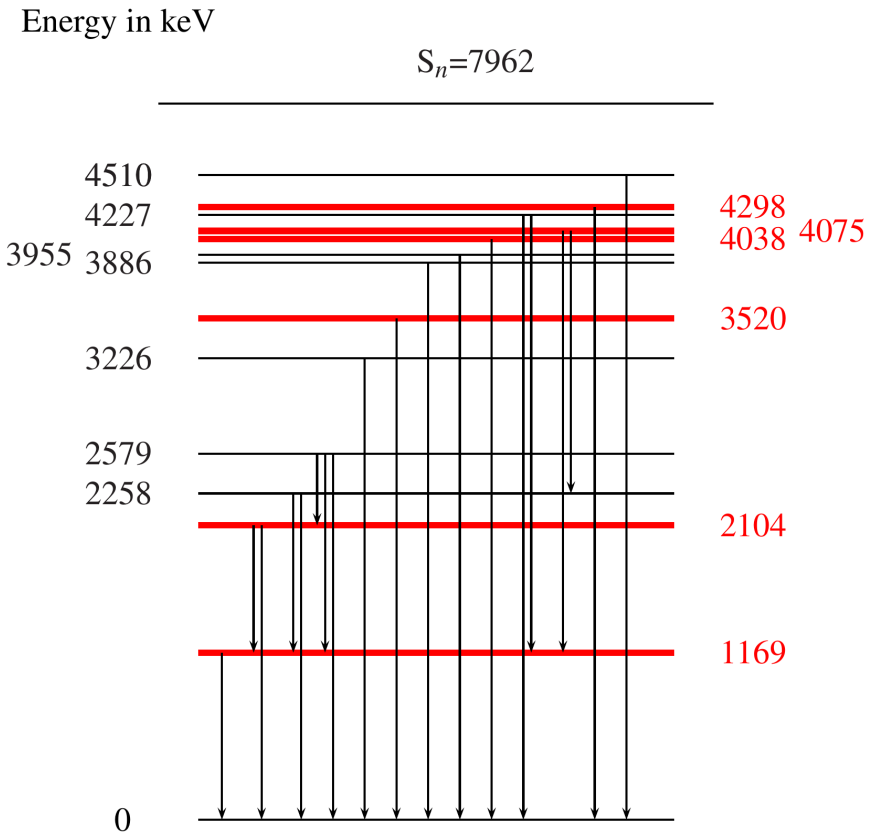

Figure 5.7.: Reduced level scheme of Sn-128. Only the 2^+-states are included. The states are mainly decaying directly to the ground state or through another 2+-state. The used states and their decay path are marked with red and thick lines. The first excited state has a lifetime of 1.63 ps. Data taken from [nnd].

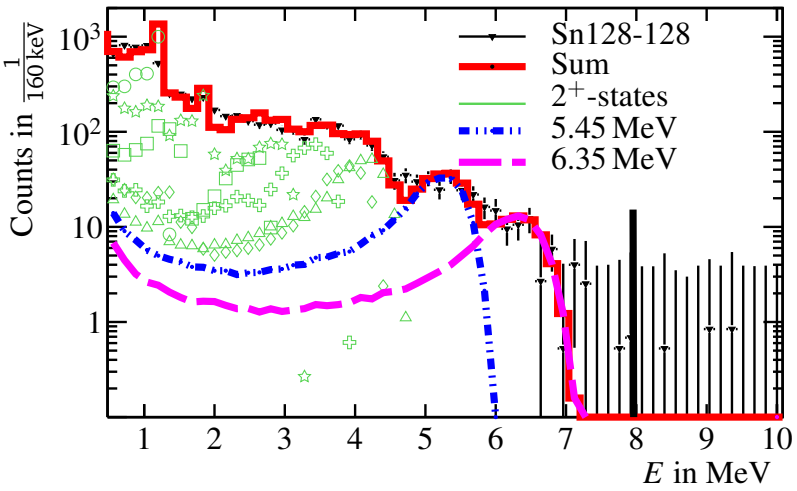

Figure 5.8.: The background is subtracted from the LaBr response. In addition the γ transitions are fitted. The known transitions are represented in blue, while the unknown transitions are represented in green.

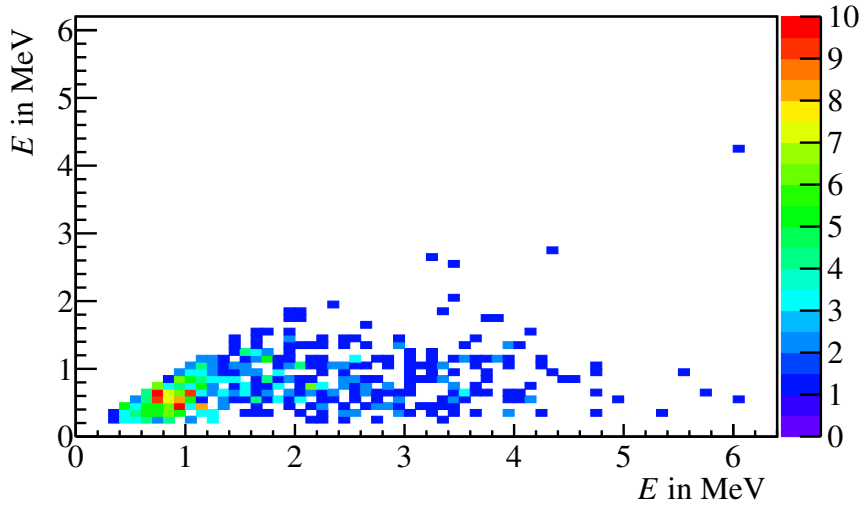

Figure 5.9.: The γ-γ coincidence-matrix for the Sn-128 isotope including DALI2. As the DALI2 spectra can almost be described solely by the 3n removal channel, a coincidence gate would clean the spectra.

The systematic errors are estimated by varying different parameters of the event reconstruction and simulation. The selection criteria were softened and hardened to obtain their influence on the cross section. Moreover, the calibration is changed within the uncertainty. The simulated efficiency is changed by a variation of the detector distances within the experimental obtained efficiency. The add-back routine for DALI2 does not have an impact onto the cross section as the cross section is evaluated with three different obtained spectra, namely the total sum, DALI2 with add-back routine, and the single LaBr. Although the third spectra is directly connected to the other two. The highest uncertainty is due to the particle selection criteria. These criteria influences the cross section by up to 2%, see figure 5.10(a) for the AOQ selection criteria and figure 5.10(b) for the dependency on the radius. Choosing a different source of background, *e.g.*, the 1n-removal reaction is negligible. The goodness of the fit rejects high contribution from this channel, and the influence is less than 0.1% of the calculated cross sections, if a pure 1n-background is assumed.
The influence of the systematic uncertainty of the simulated efficiency is explored and estimated to be about 3%. It originates due to the uncertainty of the measured efficiency. The total systematic uncertainty is estimated to be about 5% for the cross section. The systematic uncertainty for the energy is estimated by the offset between the detector systems of the known transitions. The simulated energy offset between the detector arrays with the best fit value for the new state in Sn-132 is up to 50 keV at 6.2 MeV and is therefore symmetric and of the same size as the uncertainty obtained with the fit. The change of the parameters transmission coefficient, reconstruction efficiency, and charge-state loss were investigated using different selection criteria. They are independent within statistic uncertainty of the selection criteria used. Of course the transmission coefficient drops if the geometric selection criteria are opened to wide. They have been chosen such, that the target was hit without hitting the target chamber. The influence of the different target-thickness determinations, see section 4.3 is about 1%.
For Sn-128 the size of the bins influence the fit-values significantly, for example the first excited 2^+-state is distributed to other states decaying via this state. In addition, the impact of the cross section for the transitions at energies at 5.45(15) and 6.35(15) MeV is the main contribution to their systematic uncertainty towards higher values. This is in contrast to the other isotope. For Sn-132 the main systematic influence has the selection of the incoming ions, decreasing the cross section with increasing width of the AOQ-selection window. The selection criteria of the beam profile, in terms of the incoming angle in the x-z-plane, has the opposite effect. If the angular selection cut is increased the cross section increases, too. The increase is more than the expected rise due to the longer path length through the target.

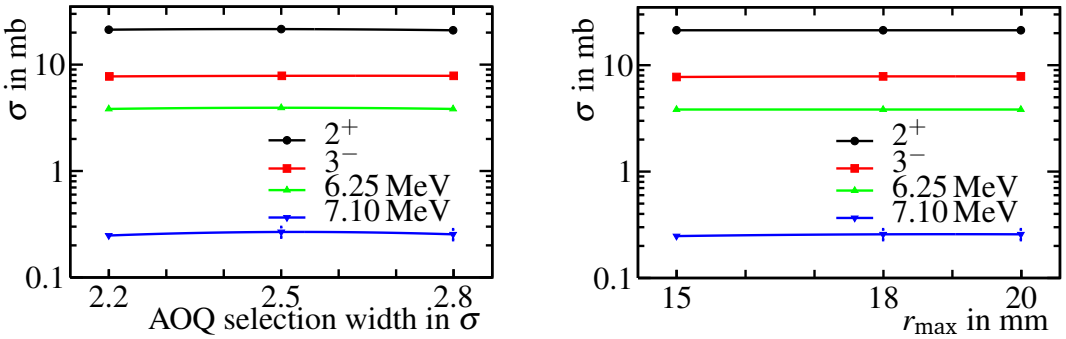

(a) (b)

Figure 5.10.: Systematic error estimation. The figures show the cross section in dependence of the beam-spot radius, right, and the outgoing AOQ selection-criteria. The cross section is almost independent of the maximal radius, and shows a small dependency of the AOQ selection-criteria width.

5.3 Comparison to Theory and Experiments

Although the observed transitions cannot be assigned to a polarity, the results obtained in this thesis are compared to the calculated isoscalar mean excitation energy using the introduced theoretical framework, see section 2.2. This yields in an energy difference of about 2 to 3 MeV. More specific, for Sn-132 the calculated energy is 8.6 to 8.77 MeV depending on the used interaction, while the obtained transitions are located at 6.25(10) and 7.10(15) MeV. For the other isotope, Sn-128, the energies are 5.45(15) and 6.35(15) MeV. As a reminder, the framework overestimates the energies with up to 3 MeV as discussed for the Sn-124 isotope by P. Papakonstantinou [PHPR14]. With this in mind the evaluated energies are in agreement withe the calculations. However, comparing the increase of the excitation energy with the number of excess neutrons contradicts the theoretical framework. It favors a decrease or constant excitation energy with increasing asymmetry $\left(\frac{N-Z}{A}\right)^2$ or neutron excess for the two isotopes, see figure 5.11.

Other experiments evaluated for the stable nuclei, Sn-120 [ZDS+15], Sn-124 [ELS+10], Ba-138, and Ce-140 [ESB+09], evaluated the strength distribution in normal kinematics using the isoscalar probes α or deuteron as beam. For the stable isotopes high resolution was achieved, resolving single transitions in the low-lying dipole region. In order to compare the results, the transition with the highest cross section was chosen. The experimental evaluated excitation energies do not show a clear trend with the number of excess neutrons. On the one hand following the isotopic chain of tin, the energy drops to the point of Sn-128 and is for Sn-132 higher again. The rise of

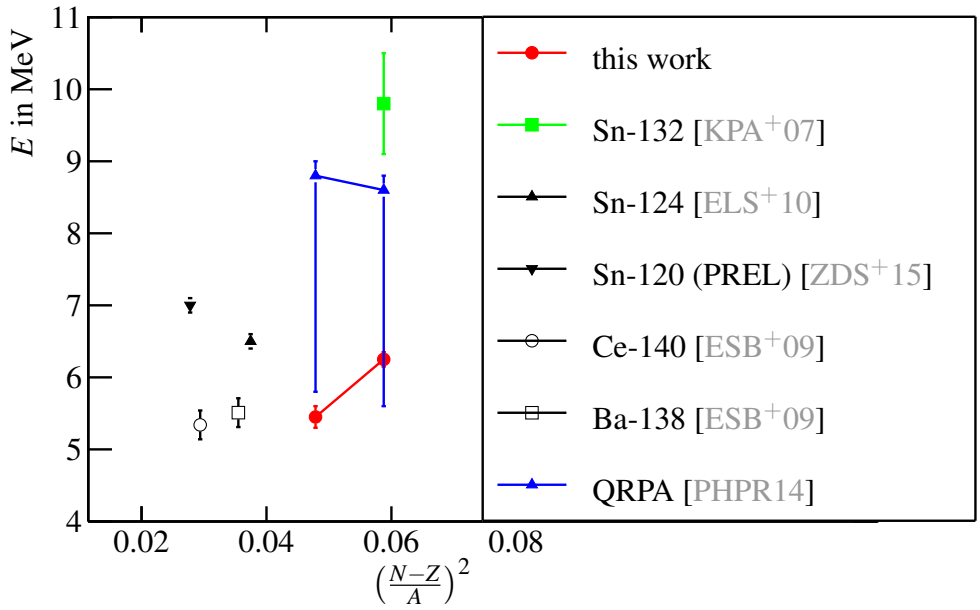

Figure 5.11.: Comparison of the excitation energy using isoscalar probes for different isotopes. In analogy to figure 2.2 from [KPA+07], the energy is plotted against the asymmetry of the nuclei. The excitation energy with the highest transition probability in the low-lying dipole region are chosen to compare with. The value for Sn-120 is preliminary and taken from the figure in reference [ZDS+15]. In color are the isotopes Sn-128 and Sn-132. The full black symbols are tin isotopes, while the open symbols are isotons of N=82, except Sn-132. In addition, the excitation energy of Sn-132 obtained in Coulomb excitation is shown.

the excitation energy for Sn-132 might be the closed neutron-shell. On the other hand following the closed neutron-shell, Sn-132, Ba-138, and Ce-140, an increase with the excess neutrons is visible.
The comparison between the excitation energies using an isoscalar and isovector probe for the Sn-132 isotope shows a splitting. The isovector probe excites dipole transition above the neutron-separation threshold at energies of 9.8(7) MeV [KPA+07], while with the α-particle energies below the threshold. The splitting in excitation energies using different probes is also evident in Sn-132, maybe in general for exotic unstable isotopes as it is for the stable isotopes.

6 Summary and Outlook

The nuclear structure is investigated for over a hundred years. The investigation revealed different phenomena in nuclei. One of those is the low-lying dipole excitation, which came into focus. The excitation is visible in stable and unstable nuclei throughout the whole nuclear chart. In stable nuclei a splitting of this excitation mode using isovector and isoscalar probes was observed. The question arises if the splitting is true also for exotic nuclei and whether it is a single-particle or collective excitation mode. For the purpose, to investigate the nuclear structure and answer the questions, facilities around the world can be used, for example RIBF at RIKEN, Japan, or the future Super-FRS at FAIR/GSI, Germany.

The mentioned questions were tackled by investigating several isotopes along the $Z = 50$ isotopic and the $n = 82$ isotonic chain. Within this thesis an experiment with the unstable isotopes Sn-128 and Sn-132 was performed and analyzed. Using in-beam γ-spectroscopy technique and α-particle as isoscalar probe the response of the isotopes was studied under zero degree. It was one of the first experiments to study exotic nuclei with an isoscalar probe, using a thick liquid-helium target. The experiment was performed at the RIBF utilizing BigRIPS and ZeroDegree Spectrometer for particle identification, and two γ-detector arrays, DALI2-crystals and LaBr:Ce-detectors from Hector.

An analysis of the data revealed two new transitions in Sn-132 and evidence for two possible new transitions in Sn-128. With the help of Geant4 simulations the transition energy and their cross sections were evaluated, see table 5.2 and 5.3. The excitation energy as a function of the asymmetry was shown in comparison with other isotopes and QRPA calculation. For the isotones the energy increases with increasing asymmetry for the isotones, while for the isotopes it decreases till Sn-128 and is increased again for Sn-132. The isoscalar excitation energy in Sn-132 is lower than in the isovector case. For both isotopes the possibility of a cascading high-lying state was investigated, but coincidences between two γ-rays were not observed. Another point is that the transitions obtained for Sn-128 are in agreement with zero, their significance is less than 5. In principle these two issues can be solved with more statistics, longer beam time. One possibility is to use the technique used in an EXL experiment [KSZ+16] and [ZAB+16]. For such purposes the NESR at FAIR [hes18a, hes18b] was planned. In a storage ring a jet-gas target can be implemented. The very thin target is compensated by recycling or reuse of the ions in the ring, increasing the luminosity per ion. Depending on the removal-reaction cross section and the lifetime of the isotope, the ions can be reused several thousand times luminosity. In addition, the jet-gas target offers the possibility to measure the scattered light particle, for example α-particles. In- and outgoing particles are identified with the same resolution.

The polarity of the new states are not known. The angular distribution of the scattering angle would help to determine the polarity. For such purposes vertex tracker could be used. This would also enable a more precise determination of the emitting angle θ of the γ-ray as the target in z-direction can be evaluated.
The aim was not only to investigate the isoscalar mode, but also to identify problems and challenges for future experiments. One of the problem was the huge particle background, which was taken care of by fitting experimental removal-reaction data, obtained in the same runs, to the spectra. Detectors with higher time resolution, such as the used LaBr-crystals would decrease this kind of background. A pulse-shape analysis like it is planned for CALorimeter for InFlight detection of γ-rays and high energy charged pArticles, called CALIFA [CGAPA+14], can help to distinguish particles and photons, thus suppressing background. Another option is to go to higher energies, which would reduce the amount of charge-states, solving the challenge of the charge-state losses and reducing at the same time the contamination of the charge states of the 3n-removal channel. As the branching ratio between particle and γ decay is unknown a measurement in complete kinematics, like for example is pursued by R^3B, could reveal strength in this region.
With the advances in detector and accelerator techniques it might be feasible soon to extend the study to even more exotic region of the nuclear charge. Then the question might be answered if the increase in isoscalar excitation energy of Sn-132 is an effect of the closed shell or not by investigating for example the isotopes Sn-134 and Cd-130, an isotone of Sn-132.

Appendices

A Beam profile

In this part of the appendix the beam profiles for the isotopes of interest, Sn-132 and Sn-128, are shown before the target at F8, followed by the extrapolated profiles at the target center. For the following parameters the plots are shown: *beta*, *x*, *y*, θ, and ϕ. θ and ϕ represent the angles in the *x*-*z*- and *y*-*z*-plane respectively. On the left hand-side the Sn-132 beam distribution is located, while on the right hand-side the Sn-128 is shown.

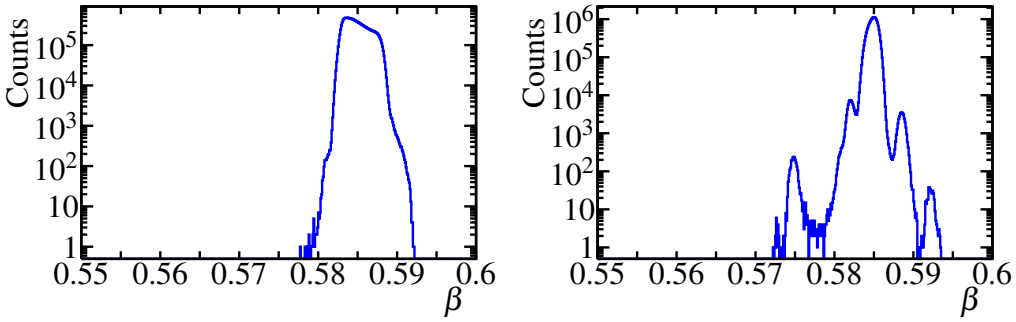

Figure A.1.: β-distribution of the selected ions at F8 beore the target. The left panel shows the distribution for Sn-132, while the right panel shows the same for Sn-128.

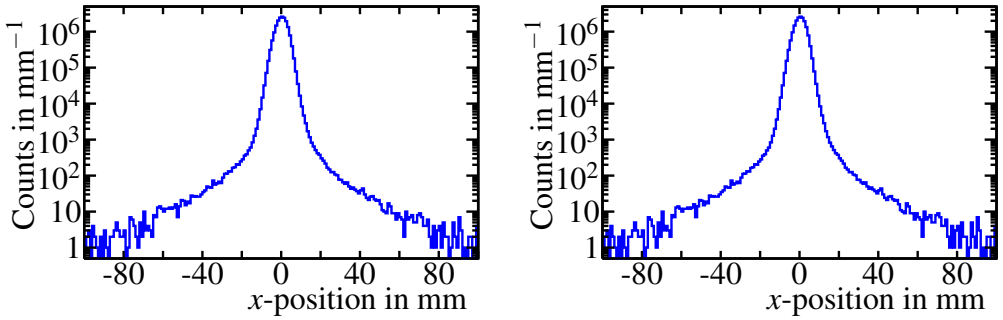

Figure A.2.: x-distribution of the selected ions at F8 beore the target. The left panel shows the distribution for Sn-132, while the right panel shows the same for Sn-128.

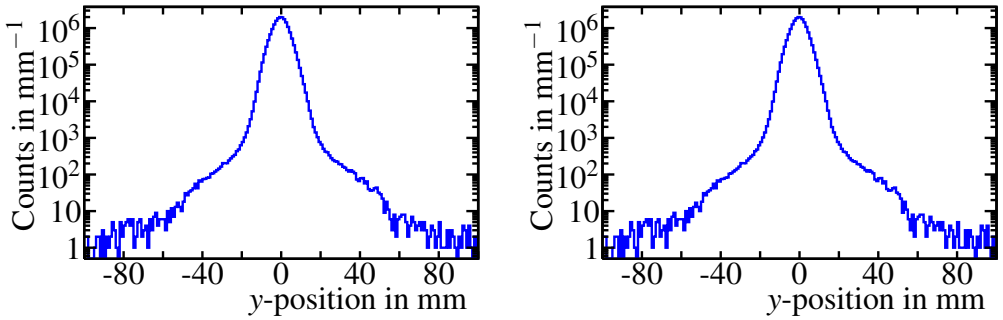

Figure A.3.: y-distribution of the selected ions at F8 beore the target. The left panel shows the distribution for Sn-132, while the right panel shows the same for Sn-128.

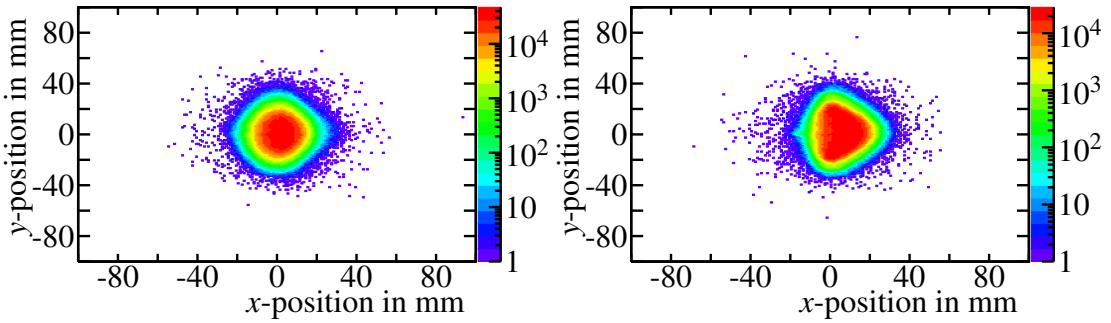

Figure A.4.: $x-y$-correlation of the selected ions at F8 beore the target. The left panel shows the distribution for Sn-132, while the right panel shows the same for Sn-128.

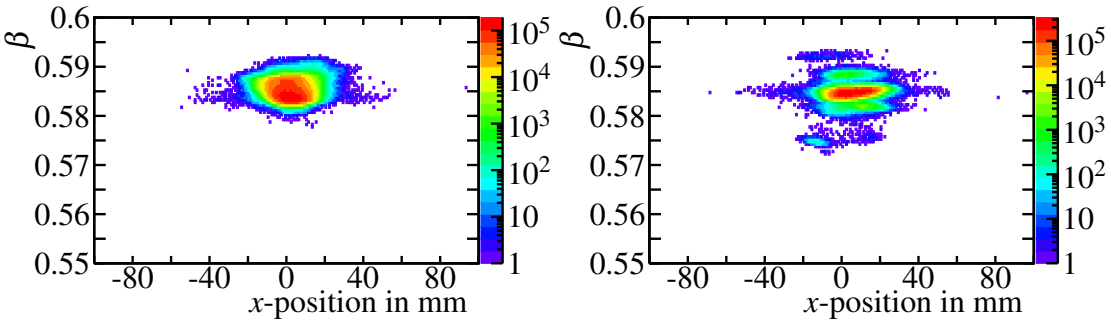

Figure A.5.: x-β-correlation of the selected ions at F8 beore the target. The left panel shows the distribution for Sn-132, while the right panel shows the same for Sn-128.

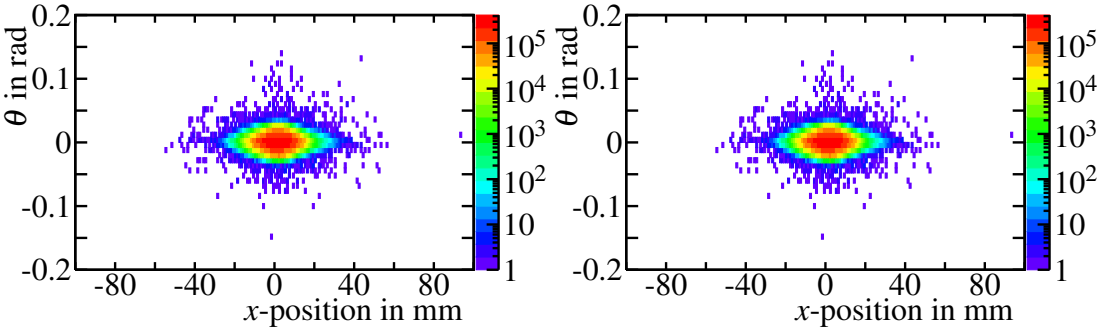

Figure A.6.: x-θ-correlation of the selected ions at F8 beore the target. The left panel shows the distribution for Sn-132, while the right panel shows the same for Sn-128.

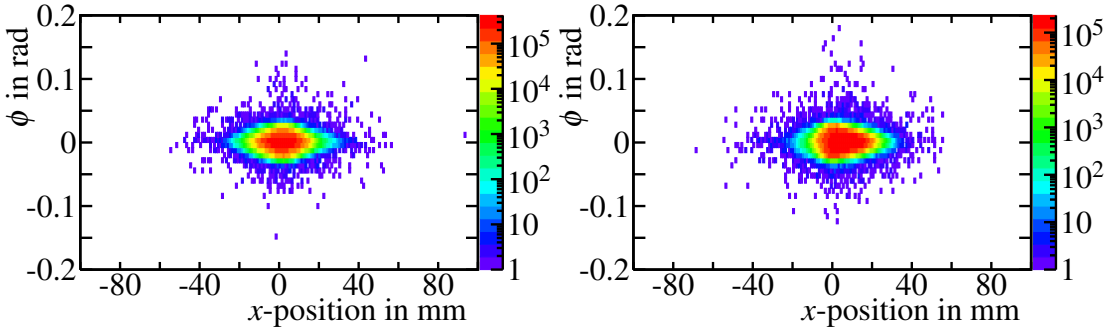

Figure A.7.: x-ϕ-correlation of the selected ions at F8 beore the target. The left panel shows the distribution for Sn-132, while the right panel shows the same for Sn-128.

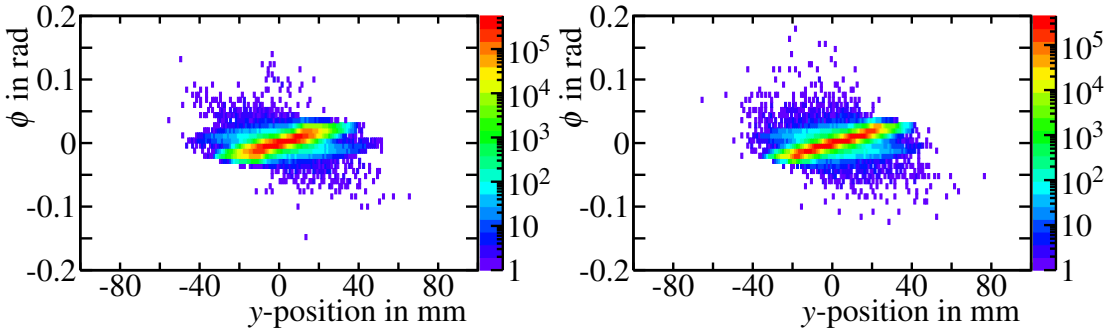

Figure A.8.: y-ϕ-correlation of the selected ions at F8. The left panel shows the distribution for Sn-132, while the right panel shows the same for Sn-128.

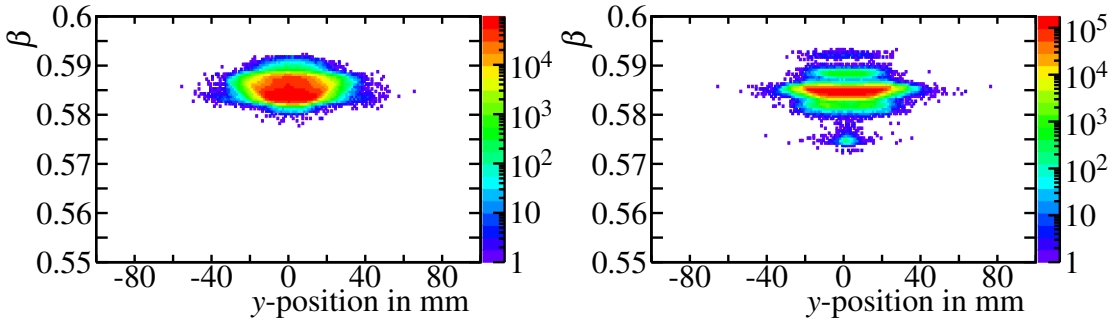

Figure A.9.: y-β-correlation of the selected ions at F8 beore the target. The left panel shows the distribution for Sn-132, while the right panel shows the same for Sn-128.

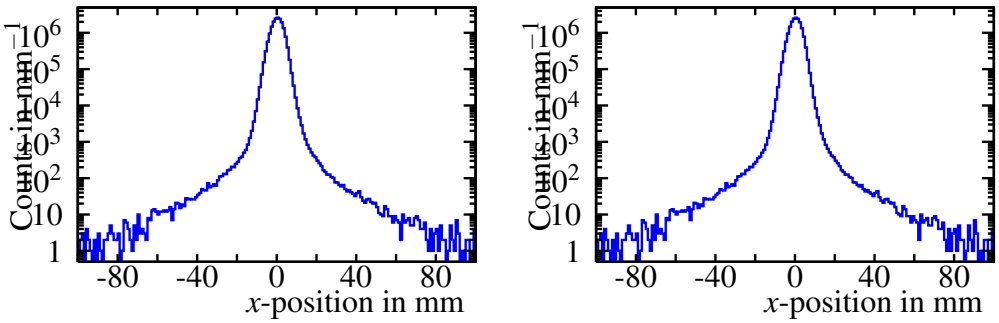

Figure A.10.: x-distribution of the selected ions at F7. The left panel shows the distribution for Sn-132, while the right panel shows the same for Sn-128.

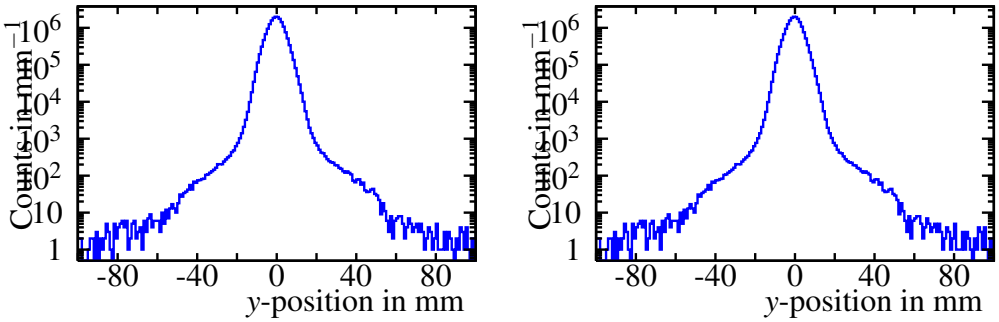

Figure A.11.: y-distribution of the selected ions at F7. The left panel shows the distribution for Sn-132, while the right panel shows the same for Sn-128.

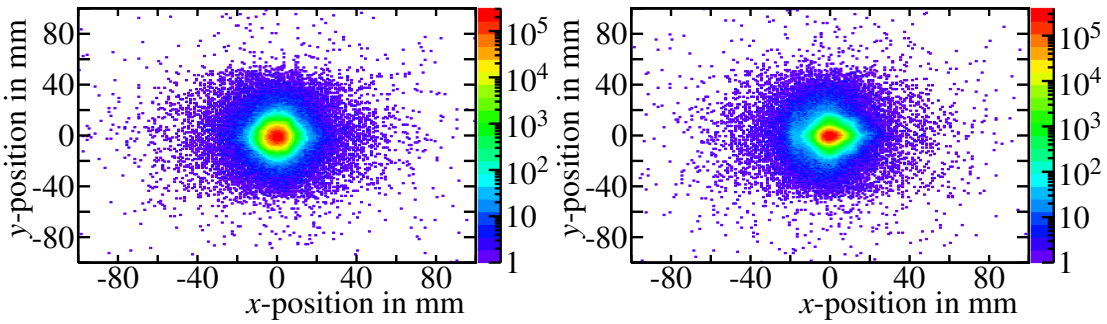

Figure A.12.: $x-y$-correlation of the selected ions at F7. The left panel shows the distribution for Sn-132, while the right panel shows the same for Sn-128.

B Fiber detector

B.1 Motivation

At the future FAIR-facility [faia], located in Darmstadt, Germany, the existing accelerator complex of GSI [GSIc] is being upgraded at the moment. The upgrade includes new experimental areas and setups. These upgrades enable the possibility to perform experiments at higher center-of-mass energies up to 1 A GeV and higher luminosity then before. Thus, more exotic nuclear regions can be explored to study nuclear structure and give important answers and insight for astrophysical questions, *e.g.*, neutron stars.
The R^3B collaboration, Reactions with Relativistic Radioactive Beams [r3b], is focused on the study of exotic nuclei through nuclear reactions. For this purpose, a large variety of detector systems is needed, as shown in figure B.1, to measure the complete kinematics of the reaction. The incoming and outgoing beam is tracked with position-sensitive detectors and fast plastic scintillators. For details of particle identification see section 3.1.2 and the references therein. For the tracking of the heavy fragments after the GLAD dipole magnet [faib], it is planned to use at least two fiber detectors to track the heavy ions. In combination with the Time-Of-Flight and a position measurement in front of the magnet, they open the possibility to determine the charge-to-mass ratio of the ions on an event-by-event basis. In addition, for high-rate experiments, fiber detectors are planned before and after the target, as the position-sensitive silicon detectors, used otherwise, cannot withstand a high rate of ions [Syn]. The requirements for the first fiber detector after the magnet are a high position resolution, radiation hardness, and high-rate capability. Prior to building such a detector, tests were performed, which is the content of this section. In the following, the design, building, and performed tests are described. In the last section, a summary of the challenges and possible solutions are discussed.

B.2 Design

The concept of a fiber detector is simple. The main idea is to place fibers straight, parallel, and without gaps next to each other. By identifying the fiber with a hit, the interaction position is defined. The resolution of such a detector in means of the standard deviation σ_x is proportional to the width w of the fiber and is the same as for a uniformly distributed variable

$$\sigma_x = \frac{w}{\sqrt{12}}. \tag{B.1}$$

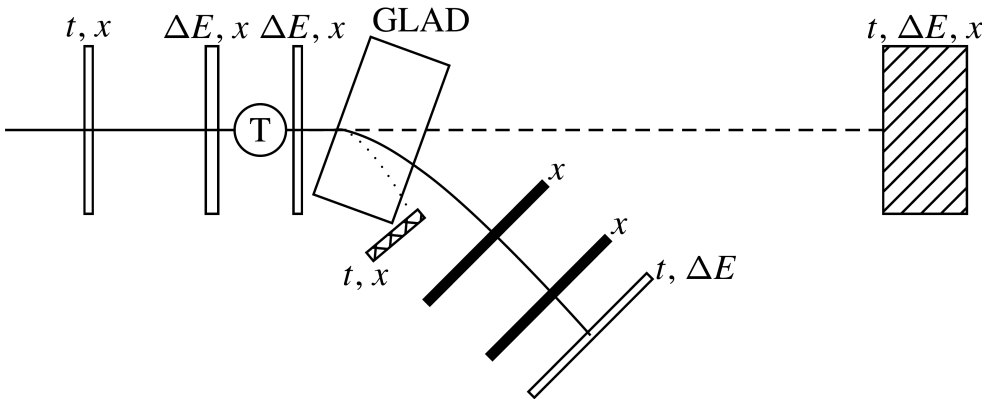

Figure B.1.: A schematic setup, which is planned to be used for the particle identification in an R^3B-experiment. The first detector is the start detector, measuring both time t and position x. Around the target are placed position-sensitive detectors, capable of determining the energy loss ΔE. The magnet GLAD deflects the outgoing particles. The neutrons (dashed line) go straight to NeuLAND [BAA+15], while the protons (dotted line) are bent the most. Fragments with higher AOQ, solid line, are bent and will travel through the heavy fragment detectors. The solid rectangles are fiber detectors. The quantities the detectors determine is indicated.

Table B.1.: Properties of the used round, single cladding fibers with a diameter $d = 0.2\,\text{mm}$ on an endless spool, values taken from [Kur16].

	core	cladding
refraction index n	1.59	1.49
density in $\frac{\text{g}}{\text{cm}^3}$	1.05	1.19
tolerance in $\frac{3\sigma}{\text{d}}$		< 2.5%
attenuation length in m		> 3
decay time in ns		2.3
emission peak in nm		428
min. bending radius in mm		≤50

The thinner the fiber the better the spacial resolution, which leads to a better resolution of the AOQ-value, hence a better particle identification. However, the energy deposition decreases, as the cross section of the fiber is quadratic or round, which is actually desired. But the decrease of deposited energy eventually reduces drastically the efficiency of the detector itself. Therefore a natural lower limit for the fiber thickness arises. On the other side, the spacial resolution should be higher or equal to the uncertainty due to angular broadening caused by the material of the detector. The amount of material inserted should be as little as possible, especially for the first detector. Any straggling increases the uncertainty of the measured angle. Another reason to minimize the material is the energy loss of the ions. The loss, resulting in an energy straggling, interferes with the velocity measurement. In addition, any introduced detector material in the beam line increases the nuclear-reaction probability of the beam with the detector. Therefore, a fiber thicknesses of 0.2 mm and 0.5 mm are chosen. For the second detector the resolution can be less, as the straggling does not disturb any further position measurements and the lesser resolution can be counteracted by a larger distance between the detectors.
The detector is going to cover the full acceptance of the magnet with a width of 400 mm and a height of 200 mm, resulting in 2000 fibers. This would lead to at least 2000 read-out channels per detector. In order to reduce the number of channels, the possibilities are a position-sensitive photodetector[1] or a bundling of fibers – the bundling as a solution is selected to maintain the high-rate capability. Each fiber is read out on both side. If a bundle of fibers is connected to one read-out on one side, all fibers of the bundle are distributed to different bundles on the other side. A combination of channel numbers has to be unique in order to identify the hit fiber by the pattern of fired photosensors, see figure B.2. The maximal achievable read-out channel reduction can be calculated according to

$$N_{\text{Channel}} = 2\sqrt{N_{\text{fiber}}}, \tag{B.2}$$

2025 fibers can be read out by 90 channels. As the detector is placed close to GLAD, the fringe field could disturb PMTs. To avoid this, the fibers are read out by SIlicon-PhotoMultipliers (SiPM). For a short description of SiPM and PMT see appendix C.1. Depending on the read-out system and where the electronics will be placed, cooling might be needed. The cooling system can then also be used to maintain a constant temperature of the photosensors, as their gain and noise level is sensitive to temperature changes.

[1] A continuous SiPM, which is read out on both side. The relation of the signal heights is connected to the position along the sensor. Multiple hits in one sensor destroy this correlation.

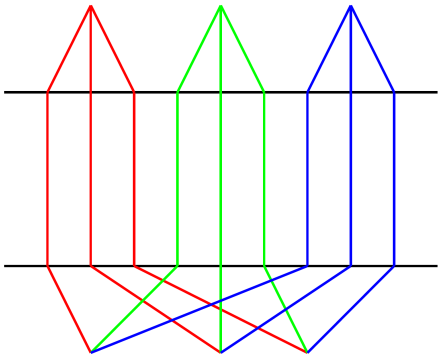

Figure B.2.: A schematic example of bundling fibers. Fibers starting at the same place at the top have the same color. The uniquely identification is obtained by combining the information of top and bottom channels.

B.3 Construction

The first two test detectors were built with square fibers. One of them was specifically built to test a bundling scheme and FEBEX read-out system, see appendix C.2.1 and for the used correlation-matrix, see appendix C.1. The fibers were glued on the frame. As the fibers are rather thin, the tension is not quite high, resulting in possible bending of the fiber in the active area. After construction the detector was controlled for twisting and gaps between the fibers, see figure B.3. The twisting is not visible, due to the small diameters of the fiber, but the gaps are visible and decrease the efficiency and increase the systematic error of the position reconstruction.
The second test detector was built to test Time-Over-Threshold (TOT) methods and the different performance of different SiPMs, namely from the companies Hamamatsu of type 12572-25p [Hama] and SensL of type MicroFC-30035-SMT [Sen][2]. For both SiPM types, eight square fibers were glued on a frame and read out on both sides. The signal is not amplified and processed by PADI-8 and a 10 ps VFTX, see appendix C.2.1. For the same beam time, a detector built with square fibers was made by hand with an active area of 6.4 x 6.4 mm^2 and single-fiber read-out, [Sch]. For the construction two slits were used to avoid twisting in the active area as the area is small gaps are not visible. This test-detector was using Hamamtsu SiPMs 3 x 3 mm^2 and the FEBEX read-out system.
For all systems, the fibers are glued into Aluminium masks, those masks are placed on top of the SiPMs. The fibers were not polished and cut with scissors. Optical grease was used for light coupling the photodetectors.
A further test detector currently under construction will use round double-layered fibers with an active area of 13 x 200 mm^2. It has two times 64 fibers, which will

[2] SiPMs of a third company FirstSensors [Fir] where tested beforehand. They were excluded as their dark count rate was much higher than for the other two

be bundled eightfold. For building the detector, Aluminium parts are mounted on a plastic ground plate, see figure B.4. The Aluminium parts include a frame on which the fibers are held using foam rubber. Several structures are used to prevent the fibers from crossing or overlapping. They have slits of 210 μm and for the second layer 400 μm, see figure C.4. The fibers of the first layer were placed and tightened. The frame with the rubber is used to hold them in place. A two-component epoxy adhesive [3] was used to glue the fibers together. Before the adhesive hardened the fibers of the second layer were stretched between the fibers of the first layer. The uncured adhesive immobilizes the fibers by capillary forces. This has the advantage that it was not necessary to stretch the fibers. Afterwards, the second layer was glued. The read-out system will be SensL SiPMs 1 x 1 mm^2 coupled to a PADI-TAMEX[4] unit. It is planned to polish the fibers, once they are glued to the masks. The round fibers have the advantage that the twisting is irrelevant for the acceptance, but the price is a double layer increasing the material and number of read-out channels. The double-layer structure increases the efficiency, as the cladding is a not sensitive area of the detector. Several[5] SiPMs are mounted on a board and supplied by positive voltage. In order to reduce crosstalk between the SiPMs, they are decoupled from each other and the power supply by a RC-circuit, see figure C.5. The signal will be sent without shaping to the PADI-ASIC.

B.4 Test

For the fiber detectors, different tests have been performed. In the laboratory the temperature dependence of the SiPMs have been investigated by J. Renner [Ren14]. It was observed that the noise decreases with decreasing temperature, but also does the efficiency of the sensor.
The light coupling and guiding was investigated by L. Schwalbach [Sch15]. The position dependence of the time and energy difference between both sides could be used to extract the position along the fiber, see section 3.2.3. It was found that the resolution of the detector system is not high enough to apply such methods.

As beam-time was available in October 2014 and June 2016 two in-beam tests have been performed. For the first test, the test detector was compared to the old fiber-detectors GFI (Großer FIber detector) using a Ca-40 beam. The bundling scheme is investigated, which followed the scheme in appendix C.1. Raw-spectra for the correlated energy-signal for two selected fibers are shown in the figure B.5. The energy-correlation for this detector is not straight forward and is, unfortunately, different for each pair of SiPMs. This can be explained by the different light coupling of each fiber

[3] important for the glue is that it does not dissolve the fiber and that the resulting film is very thin.
[4] TAMEX is a TDC
[5] *n* times 8, as the used PADI-chip has eight channels

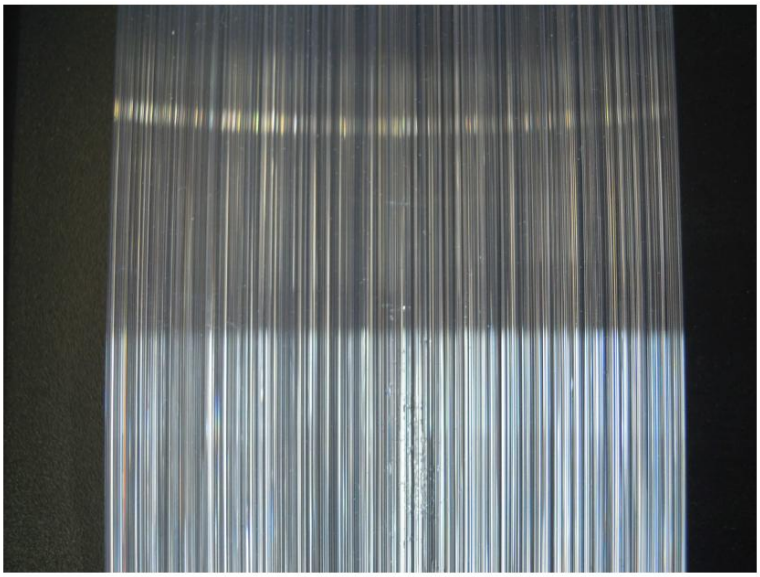

Figure B.3.: The first test detector, square fibers, with its Gaps between the fibers is visible. The possible twisting of the fibers is not visible, due to the small dimensions of the fiber. Picture was taken by J. Johansen [Joh].

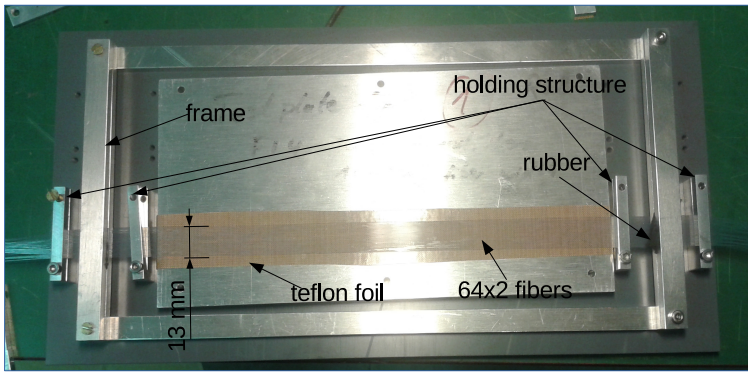

Figure B.4.: The test fiber-detector, for KVI, is under construction and will be used for the test beam-time in spring at KVI, Groningen. The detector has a double-layer structure, glued together.

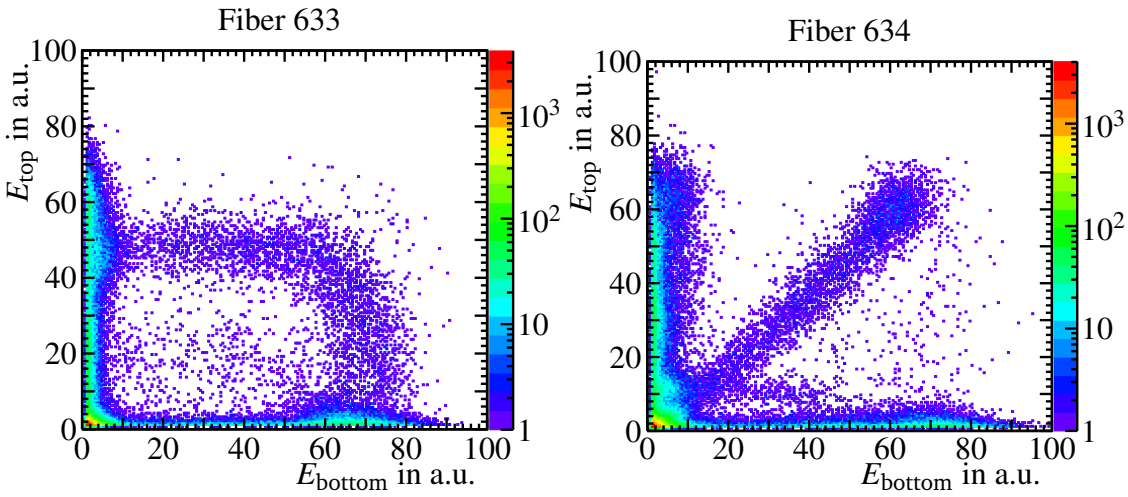

Figure B.5.: Using a bundling scheme two SiPMs are combined to reconstruct the hit fiber. In the right figure an energy correlation is visible, while for the other no clear correlation is visible.

to the sensors. The light coupling of the fibers was not enhanced with polishing, optical grease, or cement. The energy correlations show bands along one of the axes. This is related to the dark current of the SiPMs and hits in other fibers, resulting in a photon flux in one of the photsensors and, *e.g.*, dark current in the other sensor. This noise is drastically reduced in new SiPM model. The right panel of the figure shows the expected and measured energy correlation of the SiPMs of one fiber, while the left panel shown an unexpected correlation. The first correlation can be explained by assuming a production and trapping of n photons. As the distribution of the photons is isotropic, half of them travel to the top and half of them to the bottom SiPM. The other correlation perhaps occurs due to a scattering center introduced by damaging the fiber, for example a kink point. In this experiment, the position of the fibers were correlated to the other fiber detector. In the correlation plot, side peaks over the full range of the detector are visible, see figure B.6. They can be explained by wrongly identified fibers, as the distance matched exactly one channel distance. With the used bundling scheme, the peaks have a distance of 3.2 mm.

The second test detector was not bundled and were read out on both sides using time-over-threshold method. The time resolution with this method is better. As such, the time difference of correlated channels and energy correlation can be used. Both methods show a clear correlation for SiPMs, see figure B.7. In the energy spectra taken in a carbon run of 600 A MeV, the contribution of a single peak can be seen even in the high energy region. One pixel of the photosensors give about 5 ns, resulting in a detection of 15 to 20 photons on each side. The achieved time resolution between both ends of the fibers is 0.46 ns.

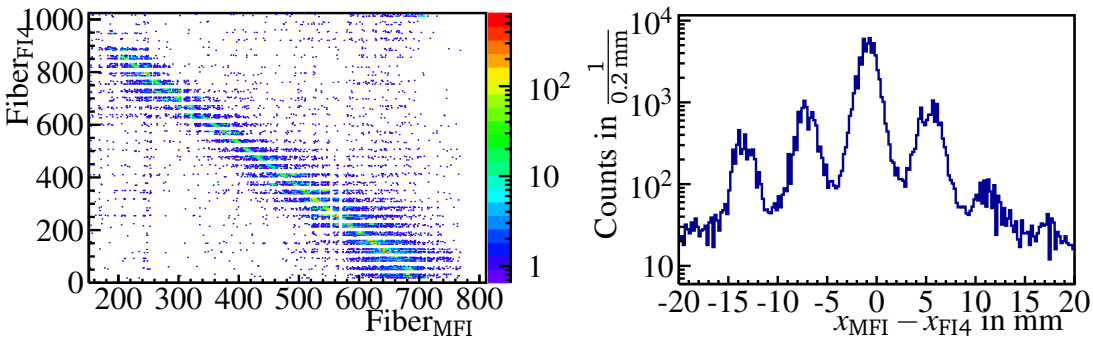

Figure B.6.: The correlation of the test detector with another fiber detector. Sidebands are visible throughout the active area. The stripes in between were skipped in the analysis.

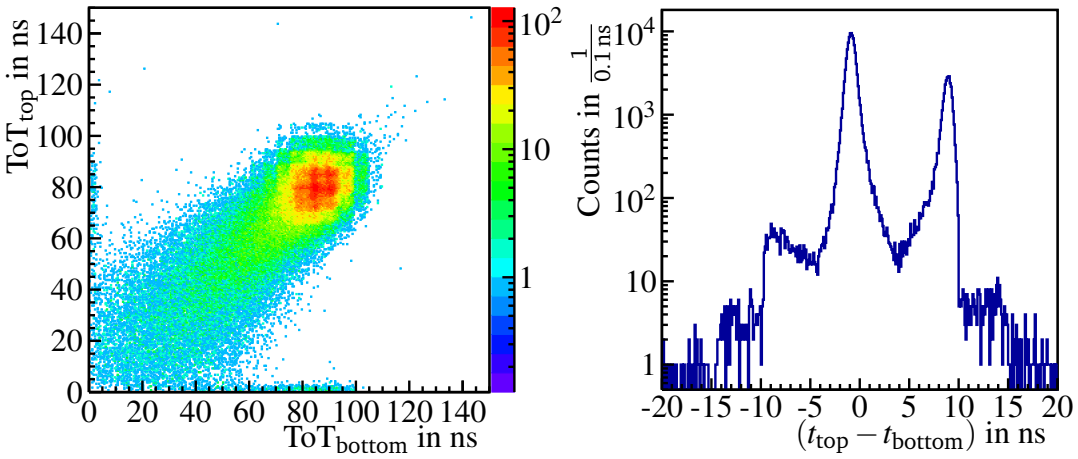

Figure B.7.: Using single fiber read out with a time-over-threshold the energy and time signals are correlated. The left figure shows the energy correlation for the SiPMs of one fiber, while the right figure shows the time difference of the two signals. In the energy spectra the number of detected photons can be estimated to be about 18 and a time resolution of 0.46 ns was achieved.

Based on the tests performed the laboratory, it was concluded to maintain for the SiPMs a stable temperature. As a cooling system might be needed for the electronics, the SiPMs can be included in the cooling system. But here caution is needed as the companies claim an efficiency and gain loss with decreasing temperature, which may result in an efficiency loss depending on the chosen energy and element. The position-measurement along the fiber is not possible due to the time and energy resolution. The best time resolution achieved was about 2 ns (FWHM) using an α-source corresponding to about 40 cm [Sch15].
For the in-beam runs the used FEBEX-system is not suited for the signal shape [Kur]. The FEBEX is designed for fast rising and slow decaying signals, but even with the used signal shaper, the signals are decaying to fast and the amplifier is a component which needs cooling. The TOT method gave a reasonable signal-to-noise discrimination using one of the two selection criteria at hand, the time difference and energy correlation of two SiPMs. For processing the signals a combination of PADI with a Clock-TDC was chosen. The TDC works with a 250 MHz clock providing a time resolution of 0.5 ns, which is almost the same resolution achieved with a 10 ps VFTX module.
The observed side peaks in the second beam test can be connected to the used matrix. Using another matrix and less fibers per bundle will reduce the side peaks distance or might even eliminate them. Due to the twisting and gap between the fibers, the scheme of gluing the fibers onto a thin foil can be pursued. Another solution to this problem are round fibers as described in section B.3. They can be built in a double-layer structure and glued together. However, the described building routine has problems, which have not been faced. Three obvious challenges are for a detector with a bigger width, more fibers next to each other. Namely, the tolerance of the fibers, the tightening of all fibers at the same time, and the second layer has a time limit if the capillary force will be used. The first challenge arises as the fiber thickness varies slightly as a function of length and has a tolerance of 2.5%. Selecting every second fiber trimmed of the spool to the second layer should solve the problem. If a winding machine is used, several spools could be used. The second challenge can be tackled with a winding machine or by not tightening the fibers, but instead putting them into a slit. The slit, with the size of the active area, has then to be removed before the glue is hardened and the second layer has to be placed within a time limit as long as the glue is still uncured. The time might be expanded by adding another thin adhesive film. A third option is to use round fibers with one layer and tilt the detector to the beam axis [Hei]. The disadvantage is the detector needs to be wider.
On one hand a two layer round fiber detector might introduce redundancy for heavy ions and increase the geometrical efficiency, on the other hand an increase of channel numbers by a factor of two and material budget by a factor of about 1.5, compared to

square fibers, is the price to pay. Note, that the material is not uniformly distributed over the area in the case of round fibers.

C Components of the Fiber Detector

The fiber used are from the company Kuraray [Kur16]. They were delivered on endless spools, in length of several kilometers. The fiber consists out of plastic. The fibers used here have a single cladding, accounting to 3% of the fiber diameter, to provide protection against damage. The scintillating light is produced in the core and isotropically emitted. The photons are trapped and guided via total reflection to the end of the fiber, where they are read out with photosensors. The critical angle ϕ, when total reflection starts, can be calculated using Snellius law,

$$n_1 \sin\alpha = n_2 \sin\beta \tag{C.1}$$

with the refraction indices of the medias $n_{1/2}$ and the angle α and β to the lot of the surface, see figure C.1. If $\sin\alpha$ is greater than $\frac{n_2}{n_1}$ total reflection occurs. The critical angle is then

$$\sin\phi = \frac{n_2}{n_1}. \tag{C.2}$$

Therefore the refraction index n_2 of the cladding is smaller than of the core n_1.

C.1 Photodetector

As photodetectors two options are available, the Photo Multiplier Tubes (PMT) and the SIlicon PhotoMultiplier (SiPM). Both photodetectors are briefly described in the following.

C.1.1 Photomultiplier Tube

The PMT basically consists of a photocathode, a focusing electrode, dynodes, and an anode, see figure C.2. The photons, stemming for example from a scintillator, hit the cathode, where they knock-out an electron via the photo-effect. The electron is accelerated towards the first dynode, passing the focusing electrode. If the electron hits the dynode secondary electrons are kicked out of the dynode, an avalanche is started. The original signal is multiplied by several dynodes afterwards towards the anode using a voltage difference of several 100 V up to 2 kV. This system provides a huge amplification up to 10^10, while maintaining a linear response to the original number of photoelectrons. The efficiency of the PMT is limited by the collection efficiency and the quantum efficiency of the photocathode. It varies with the selected cathode material and incident wavelength. Typical values for the efficiency are in the range of 20-30%. A concept for detectors with high granularity exists, the so called multi-anode PMT.

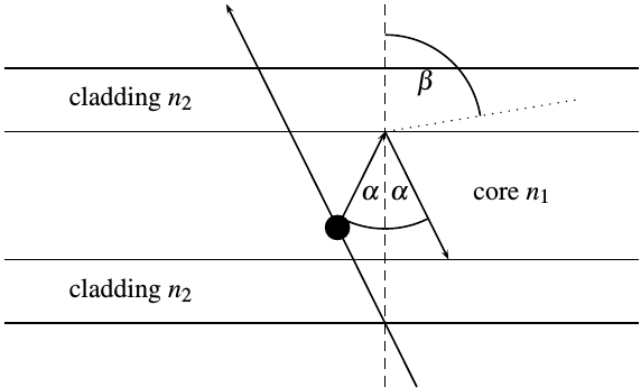

Figure C.1.: The layout of a fiber is shown here, together with the reconstruction of the total reflection. The incident ion deposits energy in the core at •. Light is produced and is reflected at the surface.

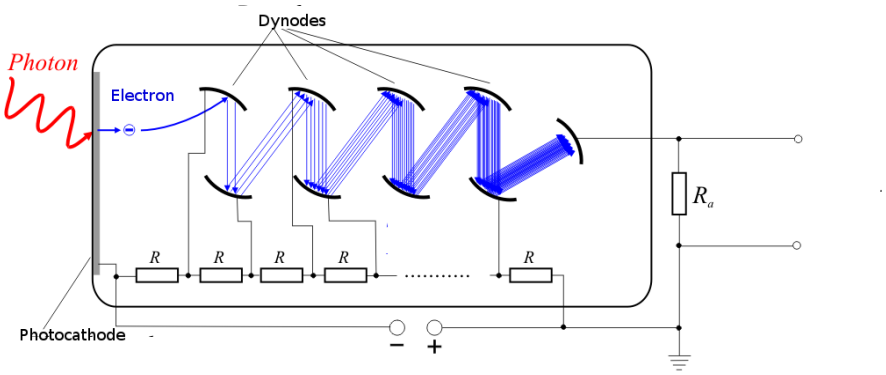

Figure C.2.: Schematic picture of a PMT with its anode, adapted from [PMT18].

C.1.2 Silicon Photomultiplier

The other system of photosensor is the SiPM, based on a semiconductor device. It consists of a p-n junction which is emptied of charge-carriers by aplying a voltage in reverse direction [Sen]. If a photon excites an electron in the junction from the valence band up to the conductor band, an electron-hole pair is created. The electron (hole) is accelerated towards the cathode (anode). If the applied voltage in the depletion region is high enough the charge-carrier will create other electron-hole pairs. The started cascade can break down the semiconductor, transforming it into a conductor. A macroscopic current is evident. This mode is called Geiger-Müller mode and is evident if the applied voltage is greater than the so called breakdown voltage V_{br}. The avalanche is stopped by resistors, as they limit the current, which lowers the voltage at the junction eventually below the breakdown voltage. One of those devices is called Avalanche Photo-Diodes (APD). If APDs are operated parallel a SiPM is at hand. APDs are placed parallel onto a substrate, which itself can be active detector volume. On top of the pixels resistors and electrical contacts are placed, reducing the active area of an APD, see figure C.3.
One APD detects only one photon at a time, but using many small APDs the signal is proportional to the number of incident photons. The number and size of the used APDs determine the linearity and fill factor[1] of the SiPM. They have advantages compared to PMTs: SiPMs can be produced very compact, are quite modular, insensitive to magnetic fields, and need lower voltages supply (about 30-60 V) than PMTs. Their quantum efficiency is around 20% to 50% for a wavelength of 450 nm, depending on the overvoltage, but the fill factor reduces the efficiency.
The disadvantages of the SiPMs are their noise sources, namely optical cross talk, afterpulses, and dark current. The optical cross talk occurs during an avalanche in high field regions in the junction. Accelerated charge carriers emit (long wavelength) photons, these photons can cause avalanches in other APDs. The afterpuls occurs if in an avalanche charge-carriers are trapped in the junction, due to impurities, and released after a time starting another avalanche. The dark current is the main source of noise generated by thermal electrons. It is a function of temperature, voltage, and active area.

C.2 Electronic

C.2.1 FEBEX

The FEBEX system [gsia] [Kur] is designed, developed, and built at GSI. It uses a trapezoidal filter, with two window length w_1 and w_2 with a gap g between them.

[1] relative active area of a SiPM. This factor is proportional to the efficiency.

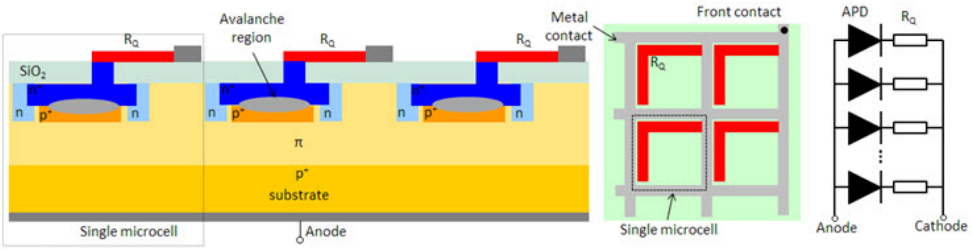

Figure C.3.: Schematic picture of a SiPM. Left is shown the cross section of the SiPM. On top are contacts and a resistor, the window, $Si0_2$, protects the active volume and enhances light coupling. Next is the APD with N^+-P^+ junction. The APD is connected through the substrate to a common anode. The middle figure shows the SiPM from the top, with red and gray the inactive surface and on the right side is the circuit diagram. Figure is taken from [SP17].

Those values can be set individually. The integrals of the windows are subtracted from each other and weighted by their width

$$f_n = \frac{1}{w_2} \sum_{w_1+n+g}^{w_2+w_1+n+g} - \frac{1}{w_1} \sum_{n}^{w_1+n} . \tag{C.3}$$

FEBEX searches for the highest filtered amplitude f_n. The system has a sample rate of 100 MHz. Due to the filter and the sampling rate, this system is not suited for fast and small signals. The signals of SiPMs have an amplitude of a few mV up to, if all pixel fire, 100-200 mV, depending on voltage and temperature. To counteract this, amplifier boards have been used. The amplifier boards were designed by Bonnes [Bon] and shape also the signal to maintain the tail for a longer time.

C.2.2 PADI and VFTX

C.2.3 PADI and VFTX

The PADI [CHH+13] and the VFTX [gsib, UKM+13] are both built and developed at GSI. The PADI chip has 8 channels and works with a comparator. The thresholds can be set for each channel individually for positive or negative signals. The module sends a Low Voltage Differential Signal (LVDS) at the moment the threshold is crossed. For leading and trailing signals two different channels are used. A TDC unit converts the signals. In the test-experiments so far a 10 ps VFTX TDC was used. The module works with a 200 MHz clock, called coarse time, which gives a time resolution of 5 ns. In order to improve the time resolution delay-lines within the chip of the VFTX are

inserted. After each delay-line a counter for the so called fine time, increases by one and the delay-line length is for each channel different and randomly distributed. In addition the delay depends on temperature, thus the VFTX has to be calibrated from time to time and for each experiment. This is done by the distribution of entries in each channel. The number of entries in each fine channel n_i is proportional to its width, therefore the additional time t_f is given by

$$t_f = 5\,\text{ns} \cdot \frac{\sum_{0}^{m-1} n_i}{N}. \tag{C.4}$$

5 ns stems from the clock cycle, m denotes to the channel number, and N to the number of total entries. The number of fine channel depends on the type of module, in this thesis the module works with channels and up to 8192 clock cycles before it is reseted again. Keeping the above in mind, the time-over-threshold is calculated by subtracting leading time and trailing time. This quantity is related to the energy deposition, as the decay time of the signal related to the amplitude and the energy deposition to the integral of the signal. If the shape of the signal is known, the amplitude, the integral, and the time-over-threshold describe the same quantity with different accuracy.

Table C.1.: The table shows the bundling matrix to reconstruct the fired fiber using the SiPMs on both side. On the next continues the table.

SiPM	1	2	3	4	5	6	7	8	9	10	11	12	13	14	15	16
1	64	96	128	160	192	224	256	288	320	352	384	416	448	480	512	544
2	95	127	159	191	223	255	287	319	351	383	415	447	479	511	543	575
3	126	158	190	222	254	286	318	350	382	414	446	478	510	542	574	606
4	157	189	221	253	285	317	349	381	413	445	477	509	541	573	605	637
5	188	220	252	284	316	348	380	412	444	476	508	540	572	604	636	668
6	219	251	283	315	347	379	411	443	475	507	539	571	603	635	667	699
7	250	282	314	346	378	410	442	474	506	538	570	602	634	666	698	730
8	281	313	345	377	409	441	473	505	537	569	601	633	665	697	729	761
9	312	344	376	408	440	472	504	536	568	600	632	664	696	728	760	792
10	343	375	407	439	471	503	535	567	599	631	663	695	727	759	791	823
11	374	406	438	470	502	534	566	598	630	662	694	726	758	790	822	854
12	405	437	469	501	533	565	597	629	661	693	725	757	789	821	853	885
13	436	468	500	532	564	596	628	660	692	724	756	788	820	852	884	916
14	467	499	531	563	595	627	659	691	723	755	787	819	851	883	915	947
15	498	530	562	594	626	658	690	722	754	786	818	850	882	914	946	978
16	529	561	593	625	657	689	721	753	785	817	849	881	913	945	977	1009
17	560	592	624	656	688	720	752	784	816	848	880	912	944	976	1008	16
18	591	623	655	687	719	751	783	815	847	879	911	943	975	1007	15	47
19	622	654	686	718	750	782	814	846	878	910	942	974	1006	14	46	78
20	653	685	717	749	781	813	845	877	909	941	973	1005	13	45	77	109
21	684	716	748	780	812	844	876	908	940	972	1004	12	44	76	108	140
22	715	747	779	811	843	875	907	939	971	1003	11	43	75	107	139	171
23	746	778	810	842	874	906	938	970	1002	10	42	74	106	138	170	202
24	777	809	841	873	905	937	969	1001	9	41	73	105	137	169	201	233
25	808	840	872	904	936	968	1000	8	40	72	104	136	168	200	232	264
26	839	871	903	935	967	999	7	39	71	103	135	167	199	231	263	295
27	870	902	934	966	998	6	38	70	102	134	166	198	230	262	294	326
28	901	933	965	997	5	37	69	101	133	165	197	229	261	293	325	357
29	932	964	996	4	36	68	100	132	164	196	228	260	292	324	356	388
30	963	995	3	35	67	99	131	163	195	227	259	291	323	355	387	419
31	994	2	34	66	98	130	162	194	226	258	290	322	354	386	418	450
32	1	33	65	97	129	161	193	225	257	289	321	353	385	417	449	481

Table C.2.: Secon part of the bundling matrix for the test detector

SiPM	17	18	19	20	21	22	23	24	25	26	27	28	29	30	31	32
1	576	608	640	672	704	736	768	800	832	864	896	928	960	992	1024	32
2	607	639	671	703	735	767	799	831	863	895	927	959	991	1023	31	63
3	638	670	702	734	766	798	830	862	894	926	958	990	1022	30	62	94
4	669	701	733	765	797	829	861	893	925	957	989	1021	29	61	93	125
5	700	732	764	796	828	860	892	924	956	988	1020	28	60	92	124	156
6	731	763	795	827	859	891	923	955	987	1019	27	59	91	123	155	187
7	762	794	826	858	890	922	954	986	1018	26	58	90	122	154	186	218
8	793	825	857	889	921	953	985	1017	25	57	89	121	153	185	217	249
9	824	856	888	920	952	984	1016	24	56	88	120	152	184	216	248	280
10	855	887	919	951	983	1015	23	55	87	119	151	183	215	247	279	311
11	886	918	950	982	1014	22	54	86	118	150	182	214	246	278	310	342
12	917	949	981	1013	21	53	85	117	149	181	213	245	277	309	341	373
13	948	980	1012	20	52	84	116	148	180	212	244	276	308	340	372	404
14	979	1011	19	51	83	115	147	179	211	243	275	307	339	371	403	435
15	1010	18	50	82	114	146	178	210	242	274	306	338	370	402	434	466
16	17	49	81	113	145	177	209	241	273	305	337	369	401	433	465	497
17	48	80	112	144	176	208	240	272	304	336	368	400	432	464	496	528
18	79	111	143	175	207	239	271	303	335	367	399	431	463	495	527	559
19	110	142	174	206	238	270	302	334	366	398	430	462	494	526	558	590
20	141	173	205	237	269	301	333	365	397	429	461	493	525	557	589	621
21	172	204	236	268	300	332	364	396	428	460	492	524	556	588	620	652
22	203	235	267	299	331	363	395	427	459	491	523	555	587	619	651	683
23	234	266	298	330	362	394	426	458	490	522	554	586	618	650	682	714
24	265	297	329	361	393	425	457	489	521	553	585	617	649	681	713	745
25	296	328	360	392	424	456	488	520	552	584	616	648	680	712	744	776
26	327	359	391	423	455	487	519	551	583	615	647	679	711	743	775	807
27	358	390	422	454	486	518	550	582	614	646	678	710	742	774	806	838
28	389	421	453	485	517	549	581	613	645	677	709	741	773	805	837	869
29	420	452	484	516	548	580	612	644	676	708	740	772	804	836	868	900
30	451	483	515	547	579	611	643	675	707	739	771	803	835	867	899	931
31	482	514	546	578	610	642	674	706	738	770	802	834	866	898	930	962
32	513	545	577	609	641	673	705	737	769	801	833	865	897	929	961	993

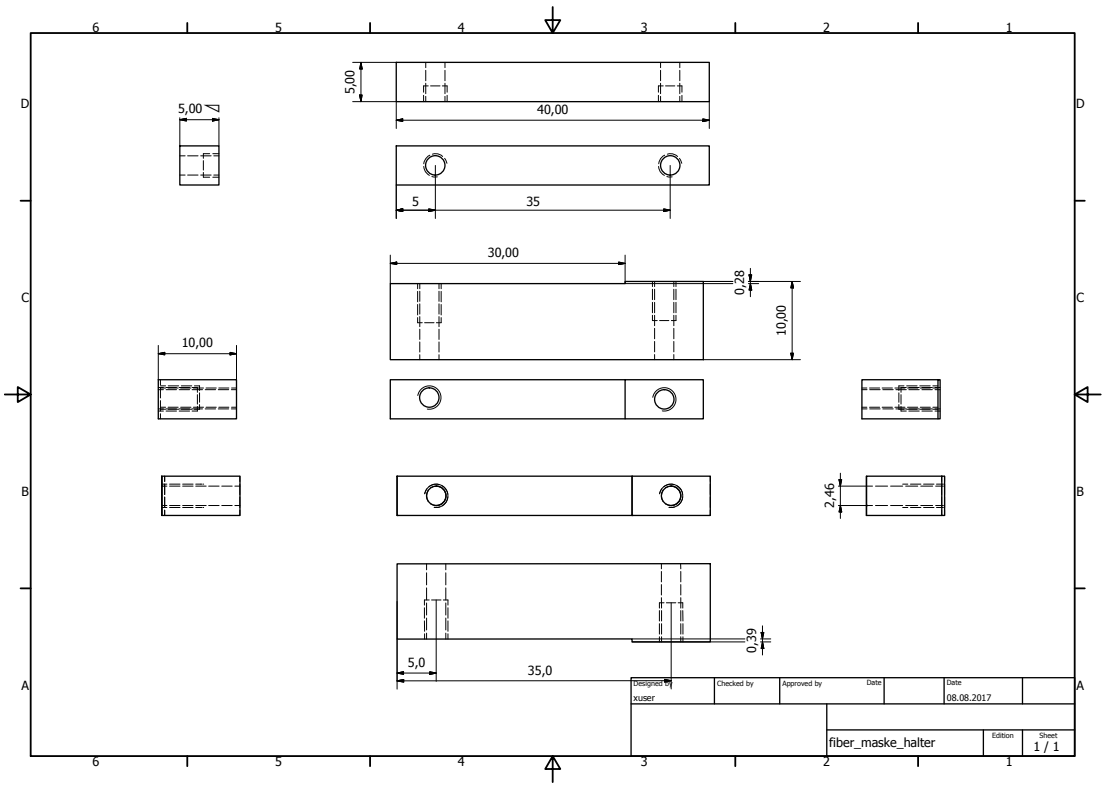

Figure C.4.: Shown here is the drawing for masks to sort the fibers. Those holding structure server the purpose to prevent the fibers from crossing each other and by pressing them together a close packaging.

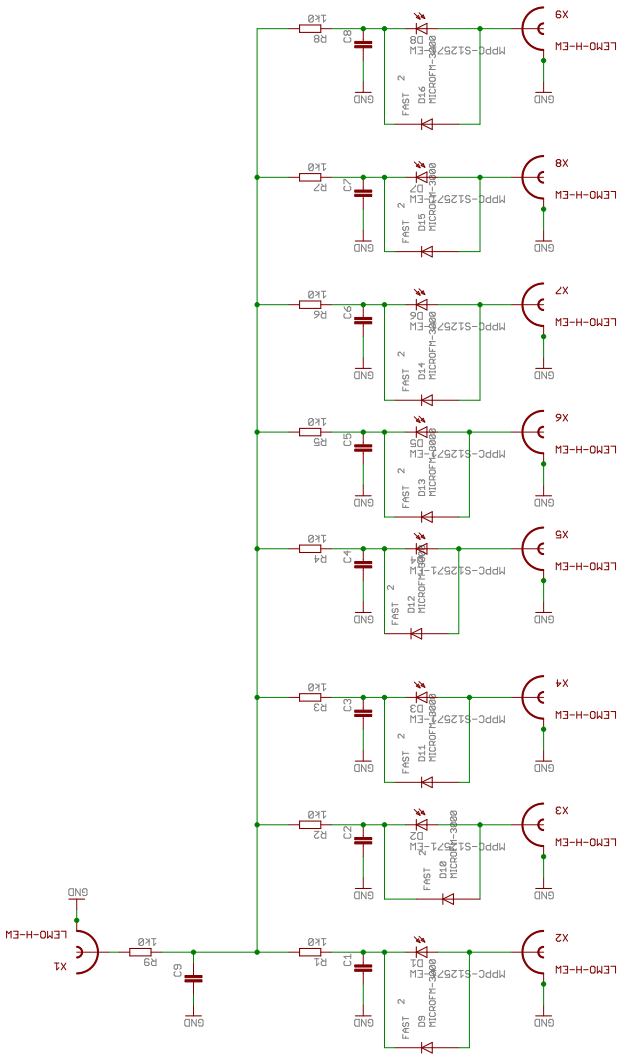

Figure C.5.: Shown here is the drawing for a test board with eight photosensors. The test board was designed for the three different types of SiPMs. They photosensors are decoupled by RC-circuits. With kind regards to Mr. Bonnes [Bon].

D Acronyms

abkg Atomic-BacKGround

AOQ mass-over-charge

APD Avalanche Photo-Diode

CFD Constant Fraction Discriminator

CNS Center of Nuclear Stud

DALI2 Detector Array for Low Intensity radiation 2

DS Down-Scale

ESWR Energy Weighted Sum Rule

fRC Fixed-frequency Ring Cyclotron

FWHM Full Width at Half Maximum

GDR Giant Dipole Resonance

HFB Hatree-Fock-Bogolyubov

IRC Intermediate-stage Ring Cyclotron

IS-ESWR Isoscalar Energy Weighted Sum Rule

ISOL Isotope Separation On-Line

1p1h 1-Particle-1-Hole

LaBr $LaBr_3$:Ce

LVDS Low Voltage Differential Signal

MUSIC MUltiple Sampling Ionization Chamber

PMT Photo Multiplier Tube

PPAC Parallel Plate Avalanche Counters

QDC charge-to-Digital Converter

QRPA Quasiparticle Random Phase Approximation

QTC charge-to-Time Converter

RIB Radioactive Ion Beams

RIBF Radioactive Isotope Beam Factory

RILAC2 RIKEN heavy Ion Linear Accelerator 2

RRC RIKEN Ring Cyclotron

SiPM SIlicon Photo Multiplier

SRC Superconducting Ring Cyclotron

SRG Similarity Correlation Operator

SC-ECR SuperConducting Electron Cyclotron Resonance

TDC Time-to-Digital Converter

TKE Total-Kinetic Energy

TOF Time-Of-Flight

ToT Time-over-Threshold

UCOM Unitary Correlation Operator Method

ZDS ZeroDegree Spectrometer

E Acknowledgement

Bibliography

[AAA+03] AGOSTINELLI, S. ; ALLISON, J. ; AMAKO, K. ; APOSTOLAKIS, J. ; ARAUJO, H. ; ARCE, P. ; ASAI, M. ; AXEN, D. ; BANERJEE, S. ; BARRAND, G. ; BEHNER, F. ; BELLAGAMBA, L. ; BOUDREAU, J. ; BROGLIA, L. ; BRUNENGO, A. ; BURKHARDT, H. ; CHAUVIE, S. ; CHUMA, J. ; CHYTRACEK, R. ; COOPERMAN, G. ; COSMO, G. ; DEGTYARENKO, P. ; DELL'ACQUA, A. ; DEPAOLA, G. ; DIETRICH, D. ; ENAMI, R. ; FELICIELLO, A. ; FERGUSON, C. ; FESEFELDT, H. ; FOLGER, G. ; FOPPIANO, F. ; FORTI, A. ; GARELLI, S. ; GIANI, S. ; GIANNITRAPANI, R. ; GIBIN, D. ; CADENAS, J.J. G. ; GONZÁLEZ, I. ; ABRIL, G. G. ; GREENIAUS, G. ; GREINER, W. ; GRICHINE, V. ; GROSSHEIM, A. ; GUATELLI, S. ; GUMPLINGER, P. ; HAMATSU, R. ; HASHIMOTO, K. ; HASUI, H. ; HEIKKINEN, A. ; HOWARD, A. ; IVANCHENKO, V. ; JOHNSON, A. ; JONES, F.W. ; KALLENBACH, J. ; KANAYA, N. ; KAWABATA, M. ; KAWABATA, Y. ; KAWAGUTI, M. ; KELNER, S. ; KENT, P. ; KIMURA, A. ; KODAMA, T. ; KOKOULIN, R. ; KOSSOV, M. ; KURASHIGE, H. ; LAMANNA, E. ; LAMPÉN, T. ; LARA, V. ; LEFEBURE, V. ; LEI, F. ; LIENDL, M. ; LOCKMAN, W. ; LONGO, F. ; MAGNI, S. ; MAIRE, M. ; MEDERNACH, E. ; MINAMIMOTO, K. ; FREITAS, P. M. ; MORITA, Y. ; MURAKAMI, K. ; NAGAMATU, M. ; NARTALLO, R. ; NIEMINEN, P. ; NISHIMURA, T. ; OHTSUBO, K. ; OKAMURA, M. ; O'NEALE, S. ; OOHATA, Y. ; PAECH, K. ; PERL, J. ; PFEIFFER, A. ; PIA, M.G. ; RANJARD, F. ; RYBIN, A. ; SADILOV, S. ; SALVO, E. D. ; SANTIN, G. ; SASAKI, T. ; SAVVAS, N. ; SAWADA, Y. ; SCHERER, S. ; SEI, S. ; SIROTENKO, V. ; SMITH, D. ; STARKOV, N. ; STOECKER, H. ; SULKIMO, J. ; TAKAHATA, M. ; TANAKA, S. ; TCHERNIAEV, E. ; TEHRANI, E. S. ; TROPEANO, M. ; TRUSCOTT, P. ; UNO, H. ; URBAN, L. ; URBAN, P. ; VERDERI, M. ; WALKDEN, A. ; WANDER, W. ; WEBER, H. ; WELLISCH, J.P. ; WENAUS, T. ; WILLIAMS, D.C. ; WRIGHT, D. ; YAMADA, T. ; YOSHIDA, H. ; ZSCHIESCHE, D.: Geant4a simulation toolkit. In: *Nuclear Instruments and Methods in Physics Research Section A: Accelerators, Spectrometers, Detectors and Associated Equipment* 506 (2003), Nr. 3, 250 - 303. http://dx.doi.org/10.1016/S0168-9002(03)01368-8. – DOI 10.1016/S0168–9002(03)01368–8. – ISSN 0168–9002

[acc] *Formation of an accelerator complex to generate RI beam.* http://www.nishina.riken.jp/facility/images/RIBFkousei_e.jpg

[AN13] AUMANN, T ; NAKAMURA, T: The electric dipole response of exotic nuclei. In: *Physica Scripta* 2013 (2013), Nr. T152, 014012. http://stacks.iop.org/1402-4896/2013/i=T152/a=014012

[BAA+15] In: BORETZKY, K. ; ALKAZOV, G. D. ; ATAR, L. ; AUMANN, T. ; BEINRUCKER, C. ; BEMMERER, D. ; BERTINI, D. ; BLANCO, A. ; CAESAR, C. ; COWAN, T. E. ; DENTINGER, G. ; ELEKES, Z. ; ENDRES, A. ; FONTE, P. ; GALAVIZ, D. ; GASPARIC, I. ; GOHL, S. ; GOLOVTSOV, V. L. ; HEFTRICH, T. ; HEIL, M. ; HEINE, M. ; HEINZ, A. ; HOLL, M. ; HORVAT, A. ; JOHANSSON, H. ; KAHLBOW, J. ; KELIC-HEIL, A. ; KISSEL, R. ; KÖRPER, D. ; KRESAN, D. ; KRIVSHICH, A. ; KUZNETSOV, V. ; LINDBERG, S. ; LOPES, L. A. ; MACHADO, J. ; MAYER, J. ; MIKI, K. ; NETTERDON, L. ; NILSSON, T. ; ORISCHIN, E. M. ; ICKSTONE, S. G. ; PLAG, R. ; POHL, M. ; REIFARTH, R. ; REINHARDT, T. P. ; REINICKE, S. ; RÖDER, M. ; ROSSI, D. ; SCHEIT, H. ; SCHINDLER, F. ; SIMON, H. ; SOBIELLA, M. ; SONNABEND, K. ; STACH, D. ; TEUBIG, P. ; THIES, R. ; TÖRNQVIST, H. ; UVAROV, L. N. ; VIKHROV, V. ; VOLKOV, S. S. ; WAGNER, A. ; ZHDANOV, A. A. ; ZILGES, A. ; ZUBER, K.: *GSI Report*. Bd. 2015-1: *NeuLAND - from double-planes to the demonstrator*. Darmstadt : GSI Helmholtzzentrum für Schwerionenforschung, 2015 ISSN 0171–4546, 200-202 p.. – BMBF (05P12RDFN8, 06FY71051, 06KY9136, 06DR134I, NupN, psp 1.2.5.1.2.5, GSI FRS R3B LAND

[BCE+07] BOUQUEREL, E. ; CATHERALL, R. ; ELLER, M. ; LETTRY, J. ; MARZARI, S. ; STORA, T. ; COLLABORATION, ISOLDE: Purification of a Zn radioactive ion beam by alkali suppression in a quartz line target prototype. In: *The European Physical Journal Special Topics* 150 (2007), Nov, Nr. 1, 277–280. http://dx.doi.org/10.1140/epjst/e2007-00323-4. – DOI 10.1140/epjst/e2007–00323–4. – ISSN 1951–6401

[BGG91] BERGER, J.F. ; GIROD, M. ; GOGNY, D.: Time-dependent quantum collective dynamics applied to nuclear fission. In: *Computer Physics Communications* 63 (1991), Nr. 1, 365 - 374. http://dx.doi.org/10.1016/0010-4655(91)90263-K. – DOI 10.1016/0010–4655(91)90263–K. – ISSN 0010–4655

[BHK16] BALL, G C. ; HACKMAN, G ; KRÜCKEN, R: The TRIUMF-ISAC facility: two decades of discovery with rare isotope beams. In: *Physica Scripta* 91 (2016), Nr. 9, 093002. http://stacks.iop.org/1402-4896/91/i=9/a=093002

[BLT+16] BORRI, M. ; LEMMON, R. ; THORNHILL, J. ; BATE, R. ; CHARTIER, M. ; CLAGUE, N. ; HERZBERG, R.-D. ; LABICHE, M. ; LINDSAY, S. ; NOLAN, P. ; PEARCE, F. ; POWELL, W. ; WELLS, D.: Detector production for the R3B Si-tracker. In: *Nuclear Instruments and Methods in Physics Research Section A: Accelerators, Spectrometers, Detectors and Associated Equipment* 836 (2016), Nr. Supplement C, 105 - 112. http://dx.doi.org/10.1016/j.nima.2016.08.050. – DOI 10.1016/j.nima.2016.08.050. – ISSN 0168–9002

[Bon] BONNES, U.: *private communication*

[Bor16] BORGE, M.J.G.: Highlights of the ISOLDE facility and the HIE-ISOLDE project. In: *Nuclear Instruments and Methods in Physics Research Section B: Beam Interactions with Materials and Atoms* 376 (2016), Nr. Supplement C, 408 - 412. http://dx.doi.org//10.1016/j.nimb.2015.12.048. – DOI /10.1016/j.nimb.2015.12.048. – ISSN 0168–583X. – Proceedings of the XVIIth International Conference on Electromagnetic Isotope Separators and Related Topics (EMIS2015), Grand Rapids, MI, U.S.A., 11-15 May 2015

[CGAPA+14] CORTINA-GIL, D. ; ALVAREZ-POL, H. ; AUMANN, T. ; AVDEICHIKOV, V. ; BENDEL, M. ; BENLLIURE, J. ; BERTINI, D. ; BEZBAKH, A. ; BLOCH, T. ; BÖHMER, M. ; BORGE, M.J.G. ; BRIZ, J.A. ; CABANELAS, P. ; CASAREJOS, E. ; GALLARDO, M. C. ; CEDERKÄLL, J. ; CHULKOV, L. ; DIERIGL, M. ; JULIO, D. D. ; DURÁN, I. ; FIORI, E. ; FOMICHEV, A. ; GALAVIZ, D. ; GASCÓN, M. ; GERNHÄUSER, R. ; GERL, J. ; GOLUBEV, P. ; GOLOVKOV, M. ; GONZÁLEZ, D. ; GORSHKOV, A. ; HEINZ, A. ; HEIL, M. ; HENNING, W. ; ICKERT, G. ; IGNATOV, A. ; JAKOBSSON, B. ; JOHANSSON, H.T. ; KRÖLL, Th. ; KRÜCKEN, R. ; KRUPKO, S. ; KURZ, N. ; BLEIS, T. L. ; LÖHER, B. ; NACHER, E. ; NILSSON, T. ; PARRILLA, C. ; PEREA, A. ; PIETRALLA, N. ; PIETRAS, B. ; REIFARTH, R. ; RIO, J. S. ; SAVRAN, D. ; SIDORCHUK, S. ; SIMON, H. ; SCHNORRENBERGER, L. ; TENGBLAD, O. ; TEUBIG, P. ; THIES, R. ; VILÁN, J.A. ; SCHMID, M. von ; WINKEL, M. ; WINKLER, S. ; WAMERS, F. ; YAÑEZ, P.: CALIFA, a Dedicated Calorimeter for the R3B/FAIR. In: *Nuclear Data Sheets* 120 (2014), 99 - 101. http://dx.doi.org/10.1016/j.nds.2014.07.017. – DOI 10.1016/j.nds.2014.07.017. – ISSN 0090–3752

[CHH+13] In: CIOBANU, M. ; HERRMANN, N. ; HILDENBRAND, K. D. ; KIS, M. ; SCHÜTTAUF, A. ; FLEMMING, H. ; DEPPE, H. ; FRÜHAUF, J. ; DEPPNER, I. ; TRÄGER, Michael ; LOIZEAU, P. A.: *GSI Report*. Bd. 2013-1: *PADI-6 and PADI-7, new ASIC prototypes for CBM ToF*.

Darmstadt : GSI Helmholtzzentrum für Schwerionenforschung, 2013 ISSN 0171–4546, 291 p.

[DM79] D.J. MORRISSEY, J.O. Rasmussen G.T. Seaborg Y. Yariv Z. F. L.F. Oliveira O. L.F. Oliveira: Microscopic and Macroscopic Model Calculations of Relativistic Heavy Ion Fragmentation Reactions. In: *Phys. Rev. Lett.* 43 (1979), S. 1139–1142

[Doo] DOORNEBAL, P.: *private communication*

[ELS+10] ENDRES, J. ; LITVINOVA, E. ; SAVRAN, D. ; BUTLER, P. A. ; HARAKEH, M. N. ; HARISSOPULOS, S. ; HERZBERG, R.-D. ; KRÜCKEN, R. ; LAGOYANNIS, A. ; PIETRALLA, N. ; PONOMAREV, V. Y. ; POPESCU, L. ; RING, P. ; SCHECK, M. ; SONNABEND, K. ; STOICA, V. I. ; WÖRTCHE, H. J. ; ZILGES, A.: Isospin Character of the Pygmy Dipole Resonance in ^{124}Sn. In: *Phys. Rev. Lett.* 105 (2010), Nov, 212503. http://dx.doi.org/10.1103/PhysRevLett.105.212503. – DOI 10.1103/PhysRevLett.105.212503

[ESB+09] ENDRES, J. ; SAVRAN, D. ; BERG, A. M. van d. ; DENDOOVEN, P. ; FRITZSCHE, M. ; HARAKEH, M. N. ; HASPER, J. ; WÖRTCHE, H. J. ; ZILGES, A.: Splitting of the pygmy dipole resonance in ^{138}Ba and ^{140}Ce observed in the $(\alpha, \alpha' \gamma)$ reaction. In: *Phys. Rev. C* 80 (2009), Sep, 034302. http://dx.doi.org/10.1103/PhysRevC.80.034302. – DOI 10.1103/PhysRevC.80.034302

[faia] http://www.fair-center.de/index.php?id=1&L=1

[faib] https://www.gsi.de/en/work/research/nustarenna/nustarenna_divisions/nuclear_reactions/activities/r3b_project_group/glad.htm

[Fir] https://www.first-sensor.com

[FKM12] FEDOSSEEV, V N. ; KUDRYAVTSEV, Yu ; MISHIN, V I.: Resonance laser ionization of atoms for nuclear physics. In: *Physica Scripta* 85 (2012), Nr. 5, 058104. http://stacks.iop.org/1402-4896/85/i=5/a=058104

[FKO+13] FUKUDA, N. ; KUBO, T. ; OHNISHI, T. ; INABE, N. ; TAKEDA, H. ; KAMEDA, D. ; SUZUKI, H.: Identification and separation of radioactive isotope beams by the BigRIPS separator at the RIKEN RI Beam Factory. In: *Nuclear Instruments and Methods in Physics Research Section B: Beam Interactions with Materials and Atoms* 317 (2013), Nr. Part B, 323 - 332. http://dx.doi.org/10.1016/j.nimb.2013.08.048.

– DOI 10.1016/j.nimb.2013.08.048. – ISSN 0168–583X. – XVIth International Conference on ElectroMagnetic Isotope Separators and Techniques Related to their Applications, December 27, 2012 at Matsue, Japan

[GAB+92] GEISSEL, H. ; ARMBRUSTER, P. ; BEHR, K.H. ; BRÜNLE, A. ; BURKARD, K. ; CHEN, M. ; FOLGER, H. ; FRANCZAK, B. ; KELLER, H. ; KLEPPER, O. ; LANGENBECK, B. ; NICKEL, F. ; PFENG, E. ; PFÜTZNER, M. ; ROECKL, E. ; RYKACZEWSKI, K. ; SCHALL, I. ; SCHARDT, D. ; SCHEIDENBERGER, C. ; SCHMIDT, K.-H. ; SCHRÖTER, A. ; SCHWAB, T. ; SÜMMERER, K. ; WEBER, M. ; MÜNZENBERG, G. ; BROHM, T. ; CLERC, H.-G. ; FAUERBACH, M. ; GAIMARD, J.-J. ; GREWE, A. ; HANELT, E. ; KNÖDLER, B. ; STEINER, M. ; VOSS, B. ; WECKENMANN, J. ; ZIEGLER, C. ; MAGEL, A. ; WOLLNIK, H. ; DUFOUR, J.P. ; FUJITA, Y. ; VIEIRA, D.J. ; SHERRILL, B.: The GSI projectile fragment separator (FRS): a versatile magnetic system for relativistic heavy ions. In: *Nuclear Instruments and Methods in Physics Research Section B: Beam Interactions with Materials and Atoms* 70 (1992), Nr. 1, 286 - 297. http://dx.doi.org/10.1016/0168-583X(92)95944-M. – DOI 10.1016/0168–583X(92)95944–M. – ISSN 0168–583X

[Got16] GOTTBERG, A.: Target materials for exotic ISOL beams. In: *Nuclear Instruments and Methods in Physics Research Section B: Beam Interactions with Materials and Atoms* 376 (2016), Nr. Supplement C, 8 - 15. http://dx.doi.org/10.1016/j.nimb.2016.01.020. – DOI 10.1016/j.nimb.2016.01.020. – ISSN 0168–583X. – Proceedings of the XVIIth International Conference on Electromagnetic Isotope Separators and Related Topics (EMIS2015), Grand Rapids, MI, U.S.A., 11-15 May 2015

[GPR+13] GIAZ, A. ; PELLEGRI, L. ; RIBOLDI, S. ; CAMERA, F. ; BLASI, N. ; BOIANO, C. ; BRACCO, A. ; BRAMBILLA, S. ; CERUTI, S. ; COELLI, S. ; CRESPI, F.C.L. ; CSATLÒS, M. ; FREGA, S. ; GULYÀS, J. ; KRASZNAHORKAY, A. ; LODETTI, S. ; MILLION, B. ; OWENS, A. ; QUARATI, F. ; STUHL, L. ; WIELAND, O.: Characterization of large volume 3.5"x8" LaBr3:Ce detectors. In: *Nuclear Instruments and Methods in Physics Research Section A: Accelerators, Spectrometers, Detectors and Associated Equipment* 729 (2013), Nr. Supplement C, 910 - 921. http://dx.doi.org/10.1016/j.nima.2013.07.084. – DOI 10.1016/j.nima.2013.07.084. – ISSN 0168–9002

[gsia] https://www.gsi.de/work/forschung/experimentelektronik/digitalelektronik/digitalelektronik/module/lwl/febex.htm

[gsib] https://www.gsi.de/work/forschung/experimentelektronik/digitalelektronik/digitalelektronik/module/vme/vftx.htm

[GSIc] GSI: *GSI*. https://www.gsi.de/start/aktuelles.htm

[Hama] http://www.hamamatsu.com/

[Hamb] HAMILTON: *HAVAR*. Data sheet,

[HD81] HARAKEH, M. N. ; DIEPERINK, A. E. L.: Isoscalar dipole resonance: Form factor and energy weighted sum rule. In: *Phys. Rev. C* 23 (1981), May, 2329–2334. http://dx.doi.org/10.1103/PhysRevC.23.2329. – DOI 10.1103/PhysRevC.23.2329

[Hei] HEIL, M.: *private communication*

[hes18a] https://www.gsi.de/work/forschung/appamml/atomphysik/ap_und_fair/sparc/anlagen/nesr.htm

[hes18b] https://www.rug.nl/kvi-cart/research/hnp/research/exl/

[hMNW99] HERRILL ; MORRISSEY, D.J. ; NOLEN, J.A. ; WINGER, J.A.: *projectile fragment separator*. http://dx.doi.org/10.1016/0168-583X(91)95108-P. Version: 199

[HOK+15] HASEBE, Hiroo ; OKUNO, Hiroki ; KUBOKI, Hironori ; IMAO, Hiroshi ; FUKUNISHI, Nobuhisa ; KASE, Masayuki ; KAMIGAITO, Osamu: Development of rotating beryllium disk stripper. In: *Journal of Radioanalytical and Nuclear Chemistry* 305 (2015), Sep, Nr. 3, 825–829. http://dx.doi.org/10.1007/s10967-015-4044-2. – DOI 10.1007/s10967–015–4044–2. – ISSN 1588–2780

[Hor] HORVAT, A.: *private communication*

[IOK+12] IMAO, Hiroshi ; OKUNO, Hiroki ; KUBOKI, Hironori ; YOKOUCHI, S ; FUKUNISHI, N ; KAMIGAITO, O ; HASEBE, Hiroo ; WATANABE, T ; WATANABE, Y ; KASE, M ; YANO, Yasushige: Charge stripping of 238U ion beam by helium gas stripper. 15 (2012), 12

[Joh] JOHANSEN, J.: *private communication*

[KIK+05] KIMURA, K. ; IZUMIKAWA, T. ; KOYAMA, R. ; OHNISHI, T. ; OHTSUBO, T. ; OZAWA, A. ; SHINOZAKI, W. ; SUZUKI, T. ; TAKAHASHI, M. ; TANIHATA, I. ; YAMAGUCHI, T. ; YAMAGUCHI, Y.: High-rate particle identification of high-energy heavy ions using a tilted electrode gas ionization chamber. In: *Nuclear Instruments and Methods in Physics Research Section A: Accelerators, Spectrometers, Detectors and Associated Equipment* 538 (2005), Nr. 1, 608 - 614. http://dx.doi.org/10.1016/j.nima.2004.08.100. – DOI 10.1016/j.nima.2004.08.100. – ISSN 0168–9002

[KKS+12] KUBO, Toshiyuki ; KAMEDA, Daisuke ; SUZUKI, Hiroshi ; FUKUDA, Naoki ; TAKEDA, Hiroyuki ; YANAGISAWA, Yoshiyuki ; OHTAKE, Masao ; KUSAKA, Kensuke ; YOSHIDA, Koichi ; INABE, Naohito ; OHNISHI, Tetsuya ; YOSHIDA, Atsushi ; TANAKA, Kanenobu ; MIZOI, Yutaka: BigRIPS separator and ZeroDegree spectrometer at RIKEN RI Beam Factory. In: *Progress of Theoretical and Experimental Physics* 2012 (2012), Nr. 1, 03C003. http://dx.doi.org/10.1093/ptep/pts064. – DOI 10.1093/ptep/pts064

[Kno00] KNOLL, G.F.: *Radiation Detection and Measurement*. 3rd. John Wiley Sons, 2000

[KOF+01] KUMAGAI, H. ; OZAWA, A. ; FUKUDA, N. ; SÜMMERER, K. ; TANIHATA, I.: Delay-line PPAC for high-energy light ions. In: *Nuclear Instruments and Methods in Physics Research Section A: Accelerators, Spectrometers, Detectors and Associated Equipment* 470 (2001), Nr. 3, 562 - 570. http://dx.doi.org/10.1016/S0168-9002(01)00804-X. – DOI 10.1016/S0168–9002(01)00804–X. – ISSN 0168–9002

[KOF+13] KUMAGAI, H. ; OHNISHI, T. ; FUKUDA, N. ; TAKEDA, H. ; KAMEDA, D. ; INABE, N. ; YOSHIDA, K. ; KUBO, T.: Development of Parallel Plate Avalanche Counter (PPAC) for BigRIPS fragment separator. In: *Nuclear Instruments and Methods in Physics Research Section B: Beam Interactions with Materials and Atoms* 317 (2013), 717 - 727. http://dx.doi.org/10.1016/j.nimb.2013.08.050. – DOI 10.1016/j.nimb.2013.08.050. – ISSN 0168–583X. – XVIth International Conference on ElectroMagnetic Isotope Separators and Techniques Related to their Applications, December 2-7, 2012 at Matsue, Japan

[KOT+09] KUBO, Toshiyuki ; OHNISHI, Tetsuya ; TAKEDA, Hiroyuki ; FUKUDA, Naoki ; KAMEDA, Daisuke ; KUSAKA, Kensuke ; YOSHIDA, Atsumasa

; YOSHIDA, Koichi ; OHTAKE, Masao ; INABE, Naohito ; YANAGISAWA, Yoshiyuki ; TANAKA, Kanenobu: ZeroDegree spectrometer at RIKEN RI Beam Factory. (2009), 10

[KPA+07] KLIMKIEWICZ, A. ; PAAR, N. ; ADRICH, P. ; FALLOT, M. ; BORETZKY, K. ; AUMANN, T. ; CORTINA-GIL, D. ; PRAMANIK, U. D. ; ELZE, Th. W. ; EMLING, H. ; GEISSEL, H. ; HELLSTRÖM, M. ; JONES, K. L. ; KRATZ, J. V. ; KULESSA, R. ; NOCIFORO, C. ; PALIT, R. ; SIMON, H. ; SURÓWKA, G. ; SÜMMERER, K. ; VRETENAR, D. ; WALUŚ, W.: Nuclear symmetry energy and neutron skins derived from pygmy dipole resonances. In: *Phys. Rev. C* 76 (2007), Nov, 051603. http://dx.doi.org/10.1103/PhysRevC.76.051603. – DOI 10.1103/PhysRevC.76.051603

[KSZ+16] KRÖLL, Thorsten ; SCHMID, Mirko von ; ZAMORA, J ; BAGCHI, Soumya ; BÖNIG, Sabine ; CSATLOS, Margit ; DILLMANN, Iris ; DIMOPOULOU, C ; EGELHOF, Peter ; EREMIN, V ; FURUNO, T ; GEISSEL, H ; GERNHÄUSER, Roman ; N HARAKEH, M ; HARTIG, A.-L ; ILIEVA, Stoyanka ; KALANTAR-NAYESTANAKI, N ; KISELEV, O ; KOLLMUS, H ; ZENIHIRO, J: Nuclear reactions in the storage ring ESR with EXL. 724 (2016), 06, S. 012026

[Kub03] KUBO, Toshiyuki: In-flight RI beam separator BigRIPS at RIKEN and elsewhere in Japan. In: *Nuclear Instruments and Methods in Physics Research Section B: Beam Interactions with Materials and Atoms* 204 (2003), Nr. Supplement C, 97 - 113. http://dx.doi.org/10.1016/S0168-583X(02)01896-7. – DOI 10.1016/S0168–583X(02)01896–7. – ISSN 0168–583X. – 14th International Conference on Electromagnetic Isotope Separators and Techniques Related to their Applications

[Kuh25] KUHN, W.: Über die Gesamtstärke der von einem Zustande ausgehenden Absorptionslinien. In: *Zeitschrift für Physik* 33 (1925), Dec, Nr. 1, 408–412. http://dx.doi.org/10.1007/BF01328322. – DOI 10.1007/BF01328322. – ISSN 0044–3328

[Kur] KURZ, N.: *private communication*

[Kur16] KURARAY: *scintillation materials*. Data sheet. http://www.kuraray.co.jp/en/index.html. Version: February 2016

[Leo87] LEO, W. R.: *Techniques for Nuclear and Particle Physics Experiments*. 3rd. Springer Verlag, 1987

[NHB17] NAKATSUKA, N. ; H. BABA, et a.: Observation of isoscalar and isovector dipole excitations in neutron-rich 20O. In: *Physics Letters B* 768 (2017), 387 - 392. http://dx.doi.org/10.1016/j.physletb.2017.03.017. – DOI 10.1016/j.physletb.2017.03.017. – ISSN 0370–2693

[NKH+08] NAKAGAWA, T. ; KIDERA, M. ; HIGURASHI, Y. ; OHONISHI, J. ; GOTO, A. ; YANO, Y.: New superconducting electron cyclotron resonance ion source for RIKEN RI beam factory project. In: *Review of Scientific Instruments* 79 (2008), Nr. 2, 02A327. http://dx.doi.org/10.1063/1.2801683. – DOI 10.1063/1.2801683

[nnd] *nndc nuclear chart*. http://www.nndc.bnl.gov/chart

[NSA14] N. S AKAMOTO, N. F UKUNISHI ET A. M. F UJIMAKI U. M. F UJIMAKI: Performance of new injector RILAC2 for RIKEN RI-Beam Factory. (2014). http://accelconf.web.cern.ch/AccelConf/LINAC2014/papers/thpp116.pdf

[ODA+14] OBERTELLI, A. ; DELBART, A. ; ANVAR, S. ; AUDIRAC, L. ; AUTHELET, G. ; BABA, H. ; BRUYNEEL, B. ; CALVET, D. ; CHÂTEAU, F. ; CORSI, A. ; DOORNENBAL, P. ; GHELLER, J. M. ; GIGANON, A. ; LAHONDE-HAMDOUN, C. ; LEBOEUF, D. ; LOISEAU, D. ; MOHAMED, A. ; MOLS, J. P. ; OTSU, H. ; PÉRON, C. ; PEYAUD, A. ; POLLACCO, E. C. ; PRONO, G. ; ROUSSE, J. Y. ; SANTAMARIA, C. ; UESAKA, T.: MINOS: A vertex tracker coupled to a thick liquid-hydrogen target for in-beam spectroscopy of exotic nuclei. In: *The European Physical Journal A* 50 (2014), Jan, Nr. 1, 8. http://dx.doi.org/10.1140/epja/i2014-14008-y. – DOI 10.1140/epja/i2014–14008–y. – ISSN 1434–601X

[OFH+14] OKUNO, Hiroki ; FUKUNISHI, N ; HASEBE, Hiroo ; IMAO, Hiroshi ; KAMIGAITO, O ; KASE, M ; KUBOKI, Hironori: Charge strippers for Radioisotope Beam Factory at RIKEN. 299 (2014), 02

[PD] P. DOORNEBAAL, et a.: *shogun-sim*. http://ribf.riken.jp/~pieter/shogun/

[PHPR14] PAPAKONSTANTINOU, P. ; HERGERT, H. ; PONOMAREV, V. Y. ; ROTH, R.: Low-energy electric dipole response of Sn isotopes. In: *Phys. Rev. C* 89 (2014), Mar, 034306. http://dx.doi.org/10.1103/PhysRevC.89.034306. – DOI 10.1103/PhysRevC.89.034306

[PMT18] *Photomultiplier schema*. https://de.wikipedia.org/wiki/Photomultiplier#/media/File:Photomultiplier_schema_de.png. Version: january 2018

[Pre16] PRETE, G.: The SPES project at the INFN-Laboratori Nazionali di Legnaro. In: *Nuovo Cimento C Geophysics Space Physics C* 38 (2016), November, S. 181. http://dx.doi.org/10.1393/ncc/i2015-15181-3. – DOI 10.1393/ncc/i2015–15181–3

[PVKC07a] PAAR, Nils ; VRETENAR, Dario ; KHAN, Elias ; COLÒ, Gianluca: Exotic modes of excitation in atomic nuclei far from stability. In: *Reports on Progress in Physics* 70 (2007), Nr. 5, 691. http://stacks.iop.org/0034-4885/70/i=5/a=R02

[PVKC07b] PAAR, Nils ; VRETENAR, Dario ; KHAN, Elias ; COLÒ, Gianluca: Exotic modes of excitation in atomic nuclei far from stability. In: *Reports on Progress in Physics* 70 (2007), Nr. 5, 691. http://stacks.iop.org/0034-4885/70/i=5/a=R02

[r3b] https://www.gsi.de/work/forschung/nustarenna/nustarenna_divisions/kernreaktionen/activities/r3b.htm

[Ren14] RENNER, J.: *Untersuchung der Untergrundzählrate an einem Silizium Photonen Zähler*. 2014

[Ric96] RICHTER, A.: Operational experience at the S-DALINAC, 1996

[RKM+05] RYUTO, H. ; KUNIBU, M. ; MINEMURA, T. ; MOTOBAYASHI, T. ; SAGARA, K. ; SHIMOURA, S. ; TAMAKI, M. ; YANAGISAWA, Y. ; YANO, Y.: Liquid hydrogen and helium targets for radioisotope beams at RIKEN. In: *Nuclear Instruments and Methods in Physics Research Section A: Accelerators, Spectrometers, Detectors and Associated Equipment* 555 (2005), Nr. 1, 1 - 5. http://dx.doi.org/10.1016/j.nima.2005.08.102. – DOI 10.1016/j.nima.2005.08.102. – ISSN 0168–9002

[Ros] ROSSI, D.: *private communication*

[Rot] ROTH, R.: *private communication*

[RS80] RING, Peter ; SCHUCK, P: *The Nuclear Many-Body Problems*. Bd. 103. 1980

[RT25] REICHE, F. ; THOMAS, W.: Über die Zahl der Dispersionselektronen, die einem stationären Zustand zugeordnet sind. In: *Zeitschrift für*

Physik 34 (1925), Dec, Nr. 1, 510–525. http://dx.doi.org/10.1007/BF01328494. – DOI 10.1007/BF01328494. – ISSN 0044–3328

[SAZ13] SAVRAN, D. ; AUMANN, T. ; ZILGES, A.: Experimental studies of the Pygmy Dipole Resonance. In: *Progress in Particle and Nuclear Physics* 70 (2013), Nr. Supplement C, 210 - 245. http://dx.doi.org/10.1016/j.ppnp.2013.02.003. – DOI 10.1016/j.ppnp.2013.02.003. – ISSN 0146–6410

[Sch] SCHOLL, S.: *private communication*

[Sch15] SCHWALBACH, L.: *Light transmission in scintillating plastic fibres*. 2015

[Sen] http://sensl.com/

[SH00] SAVAGE, Martin ; HOLSTEIN, B: Effective Field Theory in Nuclear Physics. (2000), 12. https://arxiv.org/pdf/nucl-th/0012060.pdf

[SMNW91] SHERRILL, B.M. ; MORRISSEY, D.J. ; NOLEN, J.A. ; WINGER, J.A.: The A1200 projectile fragment separator. In: *Nuclear Instruments and Methods in Physics Research Section B: Beam Interactions with Materials and Atoms* 56-57 (1991), Nr. Part 2, 1106 - 1110. http://dx.doi.org/10.1016/0168-583X(91)95108-P. – DOI 10.1016/0168–583X(91)95108–P. – ISSN 0168–583X

[SP17] https://www.hamamatsu.com/us/en/community/optical_sensors/articles/technical_guide_to_silicon_photomultipliers_sipm/index.html#

[Syn] SYNDIKUS, I.: *private communication*

[TB08] TARASOV, O.B. ; BAZIN, D.: LISE++: Radioactive beam production with in-flight separators. In: *Nuclear Instruments and Methods in Physics Research Section B: Beam Interactions with Materials and Atoms* 266 (2008), Nr. 19, 4657 - 4664. http://dx.doi.org/10.1016/j.nimb.2008.05.110. – DOI 10.1016/j.nimb.2008.05.110. – ISSN 0168–583X. – Proceedings of the XVth International Conference on Electromagnetic Isotope Separators and Techniques Related to their Applications

[Tho25] THOMAS, W.: Über die Zahl der Dispersionselektronen, die einem stationären Zustande zugeordnet sind. (Vorläufige Mitteilung). In: *Naturwissenschaften* 13 (1925), Juli, S. 627–627. http://dx.doi.org/10.1007/BF01558908. – DOI 10.1007/BF01558908

[TMT+14] TAKEUCHI, S. ; MOTOBAYASHI, T. ; TOGANO, Y. ; MATSUSHITA, M. ; AOI, N. ; DEMICHI, K. ; HASEGAWA, H. ; MURAKAMI, H.: DALI2: A NaI(Tl) detector array for measurements of γ rays from fast nuclei. In: *Nuclear Instruments and Methods in Physics Research Section A: Accelerators, Spectrometers, Detectors and Associated Equipment* 763 (2014), Nr. Supplement C, 596 - 603. http://dx.doi.org/10.1016/j.nima.2014.06.087. – DOI 10.1016/j.nima.2014.06.087. – ISSN 0168–9002

[UKM+13] UUR, C. ; KORCYL, G. ; MICHEL, J. ; PENSCHUK, M. ; TRAXLER, M.: 264 Channel TDC Platform applying 65 channel high precision (7.2 psRMS) FPGA based TDCs. In: *2013 IEEE Nordic-Mediterranean Workshop on Time-to-Digital Converters (NoMe TDC)*, 2013, S. 1–5

[VTB+06] VOLZ, S. ; TSONEVA, N. ; BABILON, M. ; ELVERS, M. ; HASPER, J. ; HERZBERG, R.-D. ; LENSKE, H. ; LINDENBERG, K. ; SAVRAN, D. ; ZILGES, A.: The photoresponse of stable N=82 nuclei below 10 MeV. In: *Nuclear Physics A* 779 (2006), Nr. Supplement C, 1 - 20. http://dx.doi.org/10.1016/j.nuclphysa.2006.08.012. – DOI 10.1016/j.nuclphysa.2006.08.012. – ISSN 0375–9474

[Wei35] WEIZSÄCKER, C. F. v.: Zur Theorie der Kernmassen. In: *Zeitschrift für Physik* 96 (1935), Jul, Nr. 7, 431–458. http://dx.doi.org/10.1007/BF01337700. – DOI 10.1007/BF01337700. – ISSN 0044–3328

[Wie] WIELAND, O.: *private communication*

[WSS95] WIRINGA, R. B. ; STOKS, V. G. J. ; SCHIAVILLA, R.: Accurate nucleon-nucleon potential with charge-independence breaking. In: *Phys. Rev. C* 51 (1995), Jan, 38–51. http://dx.doi.org/10.1103/PhysRevC.51.38. – DOI 10.1103/PhysRevC.51.38

[ZAB+16] ZAMORA, J ; AUMANN, T ; BAGCHI, Soumya ; BÖNIG, Sabine ; CSATLOS, Margit ; DILLMANN, Iris ; DIMOPOULOU, C ; EGELHOF, Peter ; EREMIN, V ; FURUNO, T ; GEISSEL, H ; GERNHÄUSER, Roman ; HARAKEH, M.N. ; HARTIG, A.-L ; ILIEVA, Stoyanka ; KALANTAR-NAYESTANAKI, N ; KISELEV, O ; KOLLMUS, H ; KOZHUHAROV, Christophor ; ZENIHIRO, J: First measurement of isoscalar giant resonances in a stored-beam experiment. 763 (2016), 10. http://dx.doi.org/10.1016/j.physletb.2016.10.015. – DOI 10.1016/j.physletb.2016.10.015

[ZDS+15] ZILGES, A ; DERYA, V ; SAVRAN, D ; HENNIG, A ; PICKSTONE, S G. ; SPIEKER, M: The Pygmy Dipole Resonance status and new

developments. In: *Journal of Physics: Conference Series* 580 (2015), Nr. 1, 012052. http://stacks.iop.org/1742-6596/580/i=1/a=012052

[ZPM+17] ZENG, Zhi ; PAN, Xingyu ; MA, Hao ; HE, Jianhua ; CANG, Jirong ; ZENG, Ming ; MI, Yuhao ; CHENG, Jianping: Optimization of an underwater in-situ LaBr3:Ce spectrometer with energy self-calibration and efficiency calibration. In: *Applied Radiation and Isotopes* 121 (2017), 101 - 108. http://dx.doi.org/10.1016/j.apradiso.2016.12.016. – DOI 10.1016/j.apradiso.2016.12.016. – ISSN 0969–8043

List of Figures

2.1. γ-transitions in Sn-124 using different probes 5
2.2. Systematics of the isovector B(E1) value 6
2.4. Transition density 11

3.1. Primary beam accelerator complex 16
3.2. Schematics of BigRIPS 17
3.3. ZeroDegree Spectrometer 19
3.4. Schematic picture of PPAC 20
3.5. Schematics of MUSIC 21
3.6. Resolution caused by Doppler broadening 25
3.7. γ-detector setup 26
3.8. Intrinsic radiation of LaBr detectors 28
3.9. Target chamber 30
3.10. Trigger chart 32

4.1. PPAC consistency check 37
4.2. PPAC efficiency 37
4.3. Plastic consistency check 38
4.4. Determining the time offset 39
4.5. Calibration of the MUSIC 40
4.6. Corrections applied to the MUSIC 41
4.7. TKE vs β 42
4.8. Different methods to determine AOQ 44
4.9. Correction of the AOQ dependency 44
4.10. Particle identification with the ZDS. 45
4.11. Charge-changing identification. 45
4.12. Acceptance of the ZDS. 46
4.13. Beam profile with bulge-function. 47
4.14. Energy calibration of DALI2 crystals. 49
4.15. DALI2 resolution and energy calibration 50
4.16. Gain drift of DALI2 crystals. 50
4.17. LaBr calibration 52
4.18. Calibration of the Mid- and Lowgain branch of LaBr 52
4.19. LaBr parameter change 53
4.20. Time calibration of DALI2 53
4.21. Time calibration of LaBr 54
4.22. Experimental distance of DALI2 single-hits. 55

4.23. Reconstruction of the emitting angle. 57
4.24. Offset estimation of the target position. 58
4.25. Efficiency evaluation using Y-88 59
4.26. Beam profile 60
4.27. Comparison between simulation and measurement using Y-88 61
4.28. Influence of the atomic background 61
4.29. Experimental offbeam and empty-target background response of LaBr-crystals with Sn-132. 63
4.30. Experimental background-response of LaBr-crystals. 64

5.1. Background subtraction for Sn-132 69
5.2. Level scheme of Sn-132 70
5.3. Fit of the simulation to the Sn-132 spectra 71
5.4. γ-γ-matrix for Sn-132 72
5.5. Fit of the simuated response to the sum spectra 72
5.6. Sn-128 background subtraction 74
5.7. Level scheme of Sn-128 75
5.8. Sn-128 LaBr background subtracted spectra 76
5.9. Sn-128 coincidence matrix 76
5.10. Systematic error estimation for the cross section 78
5.11. Systematic evolution of excitation energy 79

A.1. β-distribution at F8 85
A.2. Beam proilfe at F8 in x-direction 85
A.3. Beam proilfe at F8 in y-direction 85
A.4. Beam proilfe at F8 in x-y-correlation 86
A.5. Beam proilfe in at F8 in x-β-correlation 86
A.6. Beam proilfe in at F8 in x-θ-correlation 86
A.7. Beam proilfe in at F8 in x-ϕ-correlation 87
A.8. Beam proilfe in at F8 in y-ϕ-correlation 87
A.9. Beam proilfe in at F8 in y-β-correlation 87
A.10. Beam proilfe in at F7 in x-direction 88
A.11. Beam proilfe in at F7 in x-direction 88
A.12. Beam proilfe in at F7 in $x-y$-correlation 88

B.1. Schematics of tracking detector setup 90
B.2. Bundling scheme for fiber detectors 92
B.3. Gap between the fibers 94
B.4. Round fiber detector 94
B.5. Energy correlation of the FEBEX test detector 95
B.6. Correlation of the test detector to MFI 96
B.7. Energy correlation of the TOT test detector 96

C.1. Fiber layout 100
C.2. Schematics of a PMT 100
C.3. Schematics of a SiPM 102
C.4. Drawing for the sorting masks of the fibers 106
C.5. Drawing for a SiPM board 107

List of Tables

3.1. Location of the in-beam detectors 17
3.2. BigRIPS parameters 17
3.3. ZDS parameter 18
3.4. DALI2 crystals 26
3.5. θ distribution of the γ-detectors. 27
3.6. Alloy-foil composition 30
3.7. DS-factor 31
3.8. Beam time 33

4.1. Number of events 43
4.2. particle identification resolution. 46
4.3. particle selection criteria. 46
4.4. Used γ-calibration sources 48
4.5. Parameters for LaBr time 55
4.6. In beam detector offset 57

5.1. Global parameters to estimate the cross section 66
5.2. Cross section of the transitions in Sn-132 68
5.3. Cross section of the transitions in Sn-128 73

B.1. Properties of the used fibers 90

C.1. Bundling matrix used for the first test detector. 104